HIGH PRECISION

INSTRUMENTATION AND CONTROL

YANG RUI

HIGH PRECISION

INSTRUMENTATION AND CONTROL

YANG RUI

(B.Eng., NATIONAL UNIVERSITY OF SINGAPORE)

Acknowledgments

I would like to express my most sincere appreciation to all who had helped me during my PhD candidature at the National University of Singapore (NUS). First of all, I would like to thank my supervisors Professor Tan Kok Kiong and Prof Arthur Tay for their helpful discussions, support and encouragement. Their wisdom, vision, devotion and gentleness brighten my research paths. Without their guidance and support, I would not have accomplished this thesis.

I would also like to express my gratitude to all my friends who helped me during my PhD candidature. Special thanks must be made to Dr Huang Sunan and Dr Sun Jie for their real-time discussions and warmhearted help. Great thanks to Mr Kong Yong Ming and Dr Teo Chek Sing for their help in providing experimental equipments and guidance in setting up platforms. Great thanks to Mr Tan Chee Siong, the lab officer in Mechatronics and Automation (M&A) Lab, for providing high-class laboratory environment for my research. Many thanks to Dr Chen Silu for working together to win the third prize in the first Agilent VEE Challenge. Thanks to all my colleagues working and used to work in M&A Lab for their friendship and help. Special thanks also to Akribis Systems and SIMTech for providing the experiment setups for testing

and verification.

Finally, I would like to thank my family for their endless love and support. Specially, I would like to express my deepest gratitude to my wife, Mengjie, for her love, understanding, support and inspiration. This thesis is dedicated to my family for their infinite stability margin.

Contents

Summary

High precision machines are widely used in industries like semiconductor, medical and automobile. With rapid development in the technologies of high precision machining and the ever increasing demand for high accuracy in the automation industry, addressing accuracy problems due to geometric, thermal and sensing errors are becoming more critical in recent years. Retrofitting the mechanical design, maintaining the operational temperature or upgrading sensors may not be feasible and can significantly increase cost. The accuracy of the position measurement in the face of such issues is fundamental and critically important to achieve high precision control performance. There is a requirement for an effective balance among measurement issues like conflicting interests in cost versus performance and different performance measures arising in the same application. Thus, this thesis focuses on the soft enhancement of high precision system using approaches including selective data fusion of multiple sensors and error compensation techniques using geometric error, thermal error and end-effector output errors.

First, a proposed method for the position control of an XYZ table using geometric error modeling and compensation is discussed. Geometric error compensation is required in order to maintain and control high precision machines. The geometric model is

formulated mathematically based on laser interferometer calibration with displacement measurements only. Only four and fifteen displacement measurements are needed to identify the error components for the XY and XYZ table respectively. These individual error components are modeled using radial basis functions (RBFs) and used by the controller for error compensation.

Secondly, a displacement and thermal error compensation approach is proposed and developed based on RBFs. Raw position and temperature signals are measured using the laser interferometer and a thermistor respectively. The overall errors are related to both movement positions and the machine operating temperatures, so a 2D-RBF network is designed and trained to model and estimate the errors for compensation.

Thirdly, an approach towards precision motion control with a selective fusion of multiple signal candidates is furnished. A specific application of a linear motor using a magnetic encoder and a soft position sensor in conjunction with an analog velocity sensor is demonstrated. The weightages of the sensors are approximated using RBFs based on measurement calibration results. The data fusion of the multiple sensors is used in the controller to improve the system performance.

Lastly, an industrial application: a multi-valve micro-dispensing drop-on-demand (DOD) system, is investigated and error compensation on both stage and the end-effector output (the droplets from the printheads) are proposed and applied. A trajectory model is proposed to study the characteristics of the printed droplets and image analysis techniques are applied to identify the trajectory parameters for the compensation.

In order to show the background and motivation of the research clearly, related literature reviews on geometric error compensation, thermal error compensation, selective data fusion and micro dispensing system are given in the corresponding chapters. In addition, extensive experimental results are presented to illustrate the effectiveness of the proposed approaches throughout the thesis.

List of Tables

List of Figures

List of Abbreviations

(x_c, y_c) Center coordinate of droplet circle

α Temperature coefficient at known temperature T_B

α_{uv} Squareness error between axis u and axis v

$\alpha_{uv}(T)$ Squareness error between axis u and axis v at temperature T

β Linear expansion coefficient

ΔL Change in length of the solid

ΔT Change in temperature

$\delta_u(u)$ Linear error along u axis with motion in u direction

$\delta_u(u, T)$ Linear error along u axis with motion in u direction at temperature T

$\delta_u(v)$ Straightness error along u axis with motion in v direction

$\delta_u(v, T)$ Straightness error along u axis with motion in v direction at temperature T

η Percentage of droplet size located within a specific range

η_μ Learning rate of RBF basis center μ

η_w Learning rate of RBF weight w

μ_i RBF basis center

$\overline{x}_{m\_d}$ Measured average droplet diameter

σ_i Standard deviation

σ_{m_d} Standard deviation of the measured average droplet diameter

$\varepsilon_u(v)$ Angular error along u axis with motion in v direction

$\varepsilon_u(v, T)$ Angular error along u axis with motion in v direction at temperature T

φ Gaussian function

$^O\vec{AB}$ Translation vector AB with reference to the coordinate frame O

$^A_B R$ Rotation matrix R from coordinate frame A to coordinate frame B

E Back propagated error

E_{ms} Mean square of errors

h Distance from the end position of the dispensing head to the substrate

K Temperature constant: 273.15

k_i Sensor weightage

n_{noise} Noise level

R_B Known thermistor resistance at known temperature T_B

R_T Thermistor resistance at temperature T

R_{meas} Measured radius of droplet circle

R_{real} Known radius of droplet circle

s_i Measurements from sensor

T_B Known temperature in thermistor calibration table

$v_{vsensor}$ Velocity signal measured by velocity sensor

w_i RBF weights

x_e Initial placement errors of dispensing head on X axis

x_p Measured distances between the target position and droplet position on X axis

x_{enc} Position signal measured by encoder

x_{laser} Position signal measured by laser interferometer

x_{meas} Real/measured movement position

x_{pos} Position signal from sensor fusion output

x_{sensor_i} Measurements from sensor

$x_{vsensor}$ Position signal measured by velocity sensor

y_e Initial placement errors of dispensing head on Y axis

y_p Measured distances between the target position and droplet position on Y axis

2D   2-Dimensional

3D   3-Dimensional

BIPM   International Bureau of Weights and Measures

CMM   Coordinated Measuring Machine

DAQ   Data Acquisition

DC   Direct Current

DOD   Drop-On-Demand

DOF   Degree-Of-Freedom

etc   et cetera

ICSI   Intracytoplasmic Sperm Injection

LabVIEW   Laboratory Virtual Instrument Engineering Workbench

Matlab   Matrix Laboratory

MEMS   Micro-Electro-Mechanical Systems

NEMS   Nano-Electro-Mechanical Systems

OOT   Operational On Time

PES   Position Error Signal

PID   Proportional-Integral-Derivative

RBF   Radial Basis Function

RI   Riemann Integral

TPS   Thermal Position Sensor

TTL   Transistor-Transistor Logic

Chapter 1

Introduction

1.1 Background and Motivation

1.1.1 Industrial applications of precision systems

Today, high precision machines like multi-axis milling machine, coordinated measuring machine (CMM) are widely used in but not exclusive to various industries such as precision engineering, micro-fabrication, nano-fabrication, semiconductor manufacturing, bio-tech product manufacturing and metrology.

Precision engineering is a set of systematized knowledge and principles for realizing high-precision machinery [4], and concerns the creation of high-precision machine tools involving their design, fabrication and measurement. There are many types of high precision machines used in precision engineering industry, ranging from conventional types like bridge type CMMs as shown in Fig. 1.1a, milling machines and drilling machines, to non-contact machines leveraging on magnetic and air-bearing as shown in Fig. 1.1b. The precision of these machines can vary from 100 micrometer in normal machining to 0.1 micrometer in optic manufacturing industry [5].

Micro-fabrication is the process involving design and fabrication of miniature struc-
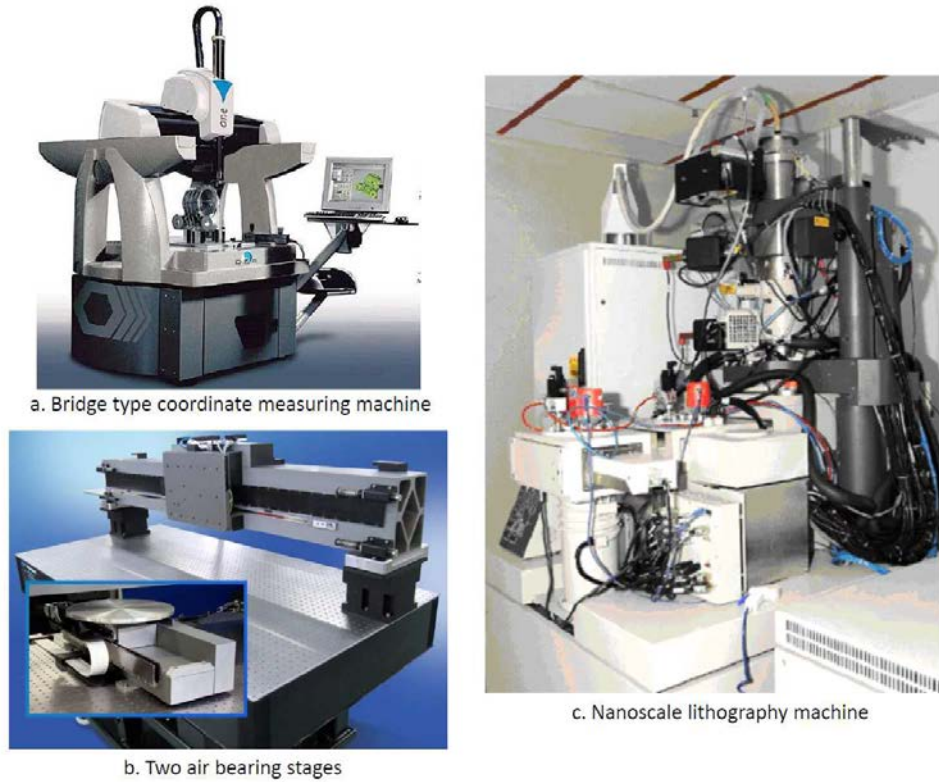
Figure 1.1: Examples of precision machines in industry

tures of micrometre scales and smaller, and it can be extended to nanometer scales which is called as nano-fabrication. Semiconductor manufacturing is also an important part of micro/nano-fabrication industry. A nanoscale lithography machine is shown in Fig. 1.1c. The devices fabricated in micro/nano-fabrication include but not limited to integrated circuits, microelectromechanical systems (MEMS), nanoelectromechanical systems (NEMS), microfluidic devices and solar cells. In micro/nano-fabrication industry, the precision requirement varies from micrometer level to nanometer level [6].

Biotechnology is an industry making use of living systems and organisms to develop useful products. In United Nations Convention on Biological Diversity, it is defined as "any technological application that uses biological systems, living organisms or deriva-

2

tives thereof, to make or modify products or processes for specific use" [8]. The term

"biotechnology" is believed to have been firstly used in 1919 by Hungarian engineer Karl

Ereky [9]. Since late 20th century, the modern biotechnology has expanded to include

new and diverse sciences such as genomics, recombinant gene technologies, applied im-

munology, which requires high precision machines during manufacturing high precision

devices for minimally invasive surgery, surgical implant placement and intracytoplasmic

sperm injection (ICSI) [10], with the precision requirement varying from millimeter level

to nanometer level.

Defined by the International Bureau of Weights and Measures (BIPM), metrology is a

"science of measurement, embracing both experimental and theoretical determinations

at any level of uncertainty in any field of science and technology" [14]. To measure

products with sufficient accuracy and test parts against the design intent, precision

measuring machine such as CMM with accuracy from submicron to nanometer has

been developed and becomes a very important device in manufacturing and assembly

process [15] [16].

With the ever increasing demand for higher precision applications, the requirements

of higher precision and accuracy in these machines are becoming more important. The

precision machining accuracy can be classified into three categories: normal machining,

precision machining and ultraprecision machining [7]. Fig. 1.2 shows the development

of achievable machining accuracy with the data from prediction by Taniguchi [7] in 1983

and the current development [5]. In Fig. 1.2, the ultra-precision machining accuracy is
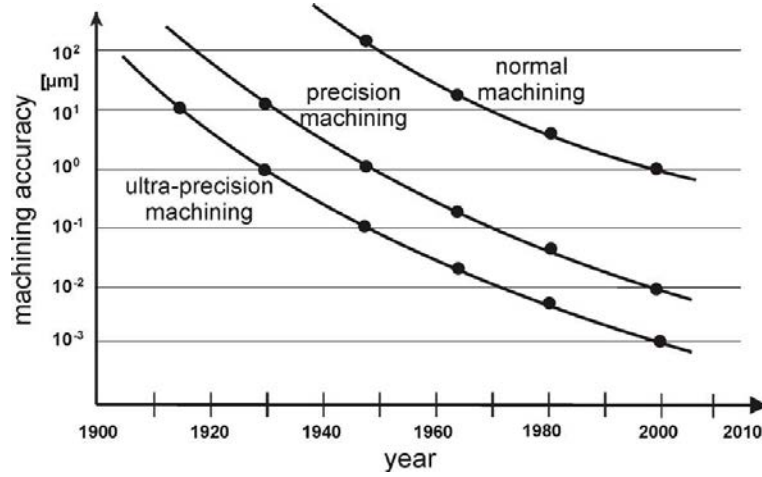
Figure 1.2: Trend in machining accuracy

the highest possible dimensional accuracy has been achieved, and the machining accuracy increases at a rate of one order every twenty years.

Many factors can affect the accuracy of the precision machine. The relative position errors between the end-effector of the precision machine and the workpiece will directly affect the machine accuracy and the quality during production. Sensors such as encoders and tachometers are typically installed on the precision machine to yield the necessary measurements. The performance and accuracy of these sensors will also affect the final performance of the machine. In this thesis, the techniques improving precision are developed for precision machine using error compensation and sensor selective control approaches. The ensuing subsections will elaborate these developments.

1.1.2 Error compensation technique in precision systems

A major problem in the precision machine is that no matter how well a machine may be designed, there is always an accuracy limit. The positional inaccuracies or errors between the end-effector and the workpiece may arise from various sources, like mechan-

ical imperfection, misalignment, environmental temperature change etc. Those errors can be roughly classified into two categories: systematic errors which are repeatable and random errors which vary all the time. For random errors, it is very difficult to completely eliminate them; while for repeatable errors which are mainly originated from geometric errors of the precision machine, improving the mechanical design may be a solution. But such an endeavor cannot solve errors caused by thermal deformation etc, and the introduced manufacturing cost will be considerably large. So nowadays, error compensation techniques which can effectively improve the accuracy of the precision machines have been considered as a good approach to solve this problem [23]- [25], due to its cost-effectiveness and ease of implementation.

There are mainly two types of error compensation techniques [2]: 1) Pre-calibrated error compensation: the same error measured before or after the machine operation is used to calibrate the machine for subsequent operations; 2) Active error compensation: the error is monitored online during the machining operation and is used to calibrate the same operation. The pre-calibrated error compensation method is suitable for repeatable machining process and error measurement, and the active error compensation method is more suitable for high accuracy achievement with low cost tools as live compensation can provide more flexibilities in the compensation during manufacturing process.

In order to apply error compensation, the error components should be measured first using corresponding instruments. Depending on the characteristics and similarities, the error components in the precision machine can be classified into different groups of error

components such as: linear error, angular error, straightness error, squareness error, parallelism error, thermal error, force induced error, spindle error etc. The measurement methods and procedures are different from each other. Usually instruments such as laser interferometers, precision straight edges, electronic levels, capacitance gauges and ball bar [27]- [29] [32]- [34] can be used to measure and identify those error components based on various factors like motion position, environment temperatures etc.

In this thesis, the laser interferometer is used to collect the positional inaccuracies and calibrate the precision machine. The laser interferometer is an instrument which measures displacements with very high accuracy and precision, and are widely used in high resolution real-time position control systems and characterization and calibration of high resolution motions. The working principle of a laser interferometer is based on the basic Michelson interferometer as shown in Fig. 1.3. The monochromatic light is split into two beams at 90 degrees by the beam splitter: one is transmitted to a movable mirror and another is transmitted to a fixed mirror. The reflections from both mirrors are recombined at the beam splitter after reflection. When the movable mirror moves in a direction parallel to the incident beam, interference exists in the recombined beam and one interference cycle represents a half wavelength displacement of the movable mirror. If the wavelength of the light is known, the displacement of the movable mirror can be accurately determined. So the laser interferometer measures the relative displacement and the accuracy can reach 1 nm [3].

But in order to measure all the error components directly using conventional laser

6
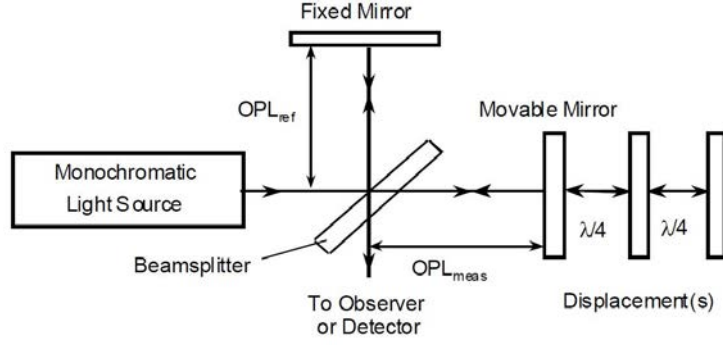
Figure 1.3: Working principle of Michelson interferometer

interferometer method, full sets of optics are necessary thus the overall cost can be increased significantly. As different error components measurements require different setups, the total calibration time of one precision machine can take several days [11]. As the accuracy of laser interferometer degrades under atmospheric conditions and can be affected by environment factors like temperature, humidity and pressure [12], it is very difficult to maintain the operational environment unchanged for several days and the calibration results can be different from day to day. Another shortcoming of the conventional laser interferometer method is that the roll errors can not be measured directly [13]. Thus from this perspective, a complete, time efficient and cost effective error compensation method using laser interferometer is desirable in precision machine calibration.

1.1.3   Sensor fusion technique in precision systems

Sensing and instrumentation are fundamental enabling technologies in precision system. To achieve high precision control, sensors are necessary to measure the related signals to very fine resolution and repeatability. Accurate and reliable data collection is the basis

which can lead to better design and performance by allowing more effective control in the system. The acquired data of the precision machine strongly relies on the accuracy, stability and repeatability of the sensors used.

Sensors have different specifications such as volume/size, signal type, speed, resolution, bandwidth, accuracy, coupling type and sensitivity [18], and the costs are different based on different specifications. Many advanced technologies can be applied to sensing industry like micro/nano-electronic technologies like MEMS and NEMS, the size of sensors has been reduced significantly to micrometer and even nanometer level [19], with a faster response speed and sensitivity compared with macroscopic scale sensors.

Besides the specifications, the performances of sensors are also affected by various error sources such as hysteresis, bias, noise, nonlinearity and degradation. Digitalization error exists in digital sensor as its output is an approximation of measured property, although it can be directly used to communicate with processor and controller. Thus analog sensor is generally more accurate and expensive due to the freedom to allow further interpolation.

Due to the different specifications and performances of the sensors and the different requirements of the precision machine, there is inevitably a limit to the overall performance achievable with a single sensor. For example, the optical encoder has a higher resolution than magnetic encoder, but it is less robust in harsh environment than magnetic encoder. For some sensors with excellent performance and accuracy, they may only work well in a certain limited frequency range [95] [96]. Thus, the fusion of signals from

multiple sensors can be a possible approach to solve above mentioned problems.

The applications of sensor data fusion technique can include an appropriate synergy of sensors to achieve dynamic balance in different combinations of the specification like speed and resolution, bandwidth and accuracy, cost and performance etc. The data fusion approach has been used in certain domains, like location tracking systems [80], reverse engineering in coordinate measuring machines [84]- [87] and robotics control [82] [83] etc. But in precision system and control, such applications are relatively scarce, like [95] [96] to solve the problem of different working frequencies of the sensors. The concept of using multiple sensors or signals is more commonly used as selective control in the process control industry, as the measurement reliability can be improved from several sensors and is more suitable in hostile environments like high temperature, dirty or vibrating surroundings [17].

In current sensor fusion technique, central limit theorem or Kalman filter is adopted with weightages based on the quality of the measurements [81], which requires complicated mathematics and extensive computation. In order to expand the sensor fusion technique to precision system applications, a more general framework of sensor fusion should be proposed from the measurements of different sensors on the precision machine, with varying selector attribute of each sensor based on sensor performance. The operational speed of the precision machine should be considered during the computation of the weightage of each sensor in the proposed framework, as it can affect the performance of the sensor and the machine. For example, an analog speed measuring sensor such as

tachometer can perform well in position control of the precision machine at relative low operational speed range with proper digital integration, but due to delay and response times in the control loop [22] and sensitivity of the sensor, the accuracy of the digital integrated signal degrades at high operational speed. Noise variances can also significantly affect the sensor performances [81] [94] and thus it should also be considered in the frame work. A general framework of sensor fusion in precision machine with operational speed and noise variances as the selector attributes will be proposed and verified via experiments in this thesis.

1.2   Objectives and Challenges

The main objective of this thesis is to enhance the accuracy and precision of the high precision machines with the proposed error estimation models of the machine errors and sensors selective control approach with compensation in the feedback control. The corresponding challenges in the modeling and compensation process during the experiments are:

Lack of simple and efficient error estimation model   There is a total of 21 geometric errors in 3D precision machine, and each of them is independent with the others. Measuring each error component requires unique set of measurement sensors like optics, thus increases the calibration time and cost. Such a complete calibration may not be necessary for a given performance specification. It would be more cost effective and time efficient if each error component can be computed using one certain measurement

10

method only. One existing method uses 22 displacement measurements to estimate the 21 errors which introduces one redundancy in the system [39]- [41]. Another existing method assumes angular errors and straightness errors are dependent, and the computation of high order polynomials increases the system complexity [42]. The existing models are either overly done given the specifications, not rigorously verified, or inefficient. Thus, a simple and efficient estimation model for all error components based on one certain measurement method only is a useful incremented result to the field which constitute an objective of the work here.

Difficulty in modeling curvilinearity   Curvilinearity exists in all the relevant quantities in this thesis. The geometric and thermal errors are position and temperature dependent in a complicated and non-predictable fashion typically a curvilinear relationship, and the noise also introduces a strong random effect in the sensors' measurement results. Thus, the raw data must be collected considering all the relevant factors and efficient models should be carefully adopted and adjusted to estimate and compensate the curvilinearity in those data.

Extensive computational and storage requirement   For error compensation method, the look-up table based on the calibration data is the usually adopted method, and linear interpolation is used between the data collection intervals. But for compensation with multiple parameters, the look-up table method requires significant increase in the table size thus requires tremendous memory usage. The memory usage is even higher

if higher resolution is required. For a huge table, the tedious search and interpolation computation is necessary at every sampling interval. Thus, a parametric approximation model which can solve above problems should be adopted.

Performance limitation of sensors under different requirements In many precision machines, a single sensor is used to measure the property of interest for precision control. But due to the limitation in specification and performance of a single sensor, using single sensor only may not be enough in situations such as high reliability requirement and better precision under various operational environments. Using multiple sensors in the precision machine can be considered as an option to deal with those situations, but the data from multiple sensors have to be appropriately fused with respect to the operating conditions. Thus, a general framework for data fusion of multiple sensors is necessary to solve this problem. These multiple sensors should offer different characteristics and performances to work with the situations of different operational parameters, thus a proper selection of suitable sensors in the experiments is also very important and worthwhile for careful consideration.

1.3 Contributions

This thesis aims to propose efficient error compensation techniques at both the stage and the end-effector and selective sensor fusion techniques to achieve precision improvement in high precision system. The following contributions have been made in this thesis.

Geometric Error Identification & Compensation Using Displacement Measurement Only   A new geometric error identification and compensation model is proposed in this thesis, with displacement measurement only using laser interferometer. As only displacement optics are involved compared with conventional method which requires full sets of optics, the proposed method is cost-effective and also saves setup and calibration time. The model of the error components is estimated using trained RBF network, thus the method can be easily implemented in digital precision machines. Different data collection intervals can be selected according to precision requirement, which is very useful for machines requiring relatively lower level of accuracy but fast calibration, like acceptance testing and periodic checking. Real-time experiments on two XY tables illustrate the effectiveness of the proposed method.

2D RBF-based Displacement & Thermal Error Model Identification and Compensation   A 2D RBF-based identification and compensation model on both displacement error and thermal error is proposed. Both measured position and temperature signals are used as the inputs to train the 2D RBF networks for error estimation, instead of the conventional method based on single input only [71]- [73]. Real time experiments are conducted to validate the effectiveness of the proposed approach, with both fixed and varying temperature cases.

Selective Control Scheme in Multiple-sensor based Data Fusion Model   A new general selective control frame work on the multiple-sensor based data fusion model

is proposed. The objective is to achieve a higher quality and accuracy in precision machine measurement, not from individual sensor but an appropriate fusion of the multiple sensors to yield a more optimal fit to the true values in a dynamic manner. With the proposed frame work, the selector attributes of each sensor can be determined, base on which the 2D RBF network can be trained. The systematic procedures to obtain all the parameters of the frame work is furnished, and the trained RBF network is used to estimate the selector attributes in the system control. The practical appeal of proposed new method is verified by a real-time case study on the control of a DC linear motor using a digital magnetic encoder and a soft position sensor in conjunction with an analog velocity sensor.

Micro-Dispensing DOD System Development A multi-valve micro-dispensing DOD system is developed and the relevant factors related to system accuracy is discussed. To accurately control the performance of the dispensing system, a parametric model on the printed droplets with its identification and compensation method are proposed. A camera vision system is setup and image processing techniques are applied to identify the parameters of the proposed model online. A systematic set of procedures to obtain all the parameters of the model is furnished. Real time experiments are conducted on both geometric error compensation on the stage and error compensation on printed droplets to illustrate the effectiveness of the proposed method.

All the approaches proposed in this thesis can be implemented in real time applications. The proposed method on geometric error compensation with displacement measurement

only is most suitable for precision systems which require fast calibration process such as periodic inspection and system diagnostic. The proposed thermal error compensation method is most suitable for precision systems which are significantly affected by thermal effects but where the control of temperature is not feasible, such as in milling machines. The proposed data fusion model for multiple-sensor is most suitable for systems with signals of interests but a single sensor cannot satisfy all the requirements, or the same type of signals must be measured of different locations (e.g.: the vibration signal). The compensation methods used in the development of the micro-dispensing DOD system is generally suitable for all types of DOD machines on which a top view camera vision system can be installed.

1.4   Thesis Organization

The thesis is organized as follows: First, in Chapter 2, following the review of existing geometric error compensation schemes, a new method on geometric error compensation using displacement measurement only is proposed with the usage of laser interferometer. The detailed modeling of each individual geometric error based on linear errors only is explained and developed. The error components are estimated using trained RBF networks. The effectiveness of the proposal is exhibited via experiments on two precision machines. Secondly, in Chapter 3, the relevant literature on the effects of machine operating temperature over the machine precision is reviewed first, and a fast yet efficient error compensation approach based on both thermal and displacement errors using 2D

RBF network is proposed. Thirdly, Chapter 4 describes a selective control approach with data fusion of multiple signal candidates towards precision motion control. A review on previous related works using data fusion in engineering and precision control has been made. The emphasis is placed on the selection weightage computation on each sensor. A specific application towards precision motion control of a linear motor using a magnetic encoder and a soft position sensor in conjunction with an analog velocity sensor is demonstrated. Then, Chapter 5 describes the setup and precision control of a multi-valve micro-dispensing drop-on-demand system in industrial applications. Both geometric error compensation on the stage and error compensation on printed droplets using image processing techniques are proposed and applied. The key parts of the image processing include object detection, circle fitting and parameter identification. Real experiments on the DOD system have been conducted and the verification of the accuracy and the efficiency of the proposed method is demonstrated using the corresponding results. Finally, conclusions and suggestions for future works are documented in Chapter 6.

Chapter 2

Geometric Error Identification & Compensation Using Displacement Measurements Only

2.1 Introduction

The technique of geometric error compensation in precision machines has been widely applied to improve the accuracy of precision machines. In order to implement geometric error compensation, it is necessary to measure these errors first. There are mainly three types of methods to measure the geometric errors: direct method, artifacts method, and displacement method. In the direct method, each error component is measured with conventional equipment such as laser interferometers, precision straight edges, electronic levels and capacitance gauges [27]- [29]. The laser interferometer system is the most widely used instrument because it can measure linear displacement with an accuracy of 1 nm and angular displacement with an accuracy of 0.002 *arcsec* [30] [31]. But there are some shortcomings, like for different types of errors such as linear, straightness and angular errors, different optics are required and each requires setting and calibration

time. Because many equipments are involved, the direct method is quite time-consuming and not cost efficient. In the artifacts method, the ball bar is used as the artifact standard to collect the motion errors, and the error traces are used to identify the error components, like double ball bar method by Kakino et al. [32], laser ball bar method by Srinivasa et al. [33] and 2D ball plate method by Caskey et al. [34]. But if there are more significant errors in the motion, extracting the error components becomes quite difficult. Thus, the artifacts method is only suitable for a few dominant errors in short range calibration.

In the displacement method, only linear errors are measured using the laser interferometer system. As the measured displacement results are influenced by other geometric errors as well, all the remaining error components can be derived from displacement measurements at different positions [35]. With only linear optics involved, the displacement method is relatively simpler than the previous two methods. Therefore, the displacement method is more suitable and popular in practical applications due to time and cost efficiency [36]- [42]. But the calculation process in the displacement method is quite sensitive to the noise level and repeatability of the machine, thus averaging techniques are required to improve the accuracy [38]. Zhang et al. are the first to develop a straightforward measurement method to assess the 21 geometric errors using linear displacement measurements only [39]- [41]. In Zhang's method, there are 22 lines required to be measured, and techniques like least square fitting and iterative computation with a series of intermediate equations are used to identify all the 21 errors. Zhang's method

can significantly improve the accuracy of the machine. However, this method also has shortcomings. Using 22 lines to calibrate 21 errors apparently brings in redundancy issue as there is an excess line, which implies that this method can be further improved with fewer lines to reduce machine calibration time.

Chen et al. improved Zhang's approach by measuring the displacement errors with only 15 lines in the machine operational span [42]. Chen's method is relatively simpler and faster, but there are shortcomings in his approach. Firstly, the straightness errors are assumed to be related to integration of angular errors and obtained via off-line calculations instead of online ones, which thus save displacement lines measurement. The validity of the assumption is quite debatable as the geometric errors may be independent. Secondly, high order polynomials are assumed for pitch, yaw, roll and squareness errors and least square algorithms are used to fit these polynomials from the measured displacement results. Similarly, Umetsu et al. also use matrix and polynomials method to estimate the errors [43]. But the problem in determining a suitable polynomial order for all the errors involved requires time and this increases the complexity as well.

In this chapter, motivated by above mentioned problems, a new method for geometric compensation with displacement measurements only is proposed. The method requires fewer lines to be measured, with only 15 lines for an XYZ table, thus reducing the complexity and calibration time. It also provides for flexibilities as some of the lines can be arbitrarily chosen. Compared with previous methods, new approaches are used to estimate the straightness and squareness errors. The RBF is used in this method

to approximate the errors measured for online compensation, so no order estimation or look up table is needed. This proposed method is more suitable for machines requiring a relative low level of accuracy but fast calibration, like those used for acceptance testing and periodic quality checking.

2.2 Geometric Error Modeling Using Displacement Measurement Only

2.2.1 Mathematical modeling of geometric errors

For positioning machines, geometric errors may exist thus reducing the machine accuracy. Then error compensation model is necessary if high precision movement needs to be satisfied. To build the error compensation model, the machine should be calibrated and errors should be measured at selected points within the operation span of the machine. For an XYZ table, the geometric errors may be decomposed into 21 underlying components, which are 3 linear errors, 3 squareness errors, 6 straightness errors and 9 angular errors [44]. The overall position is accumulated by these errors, and a mathematical error model is provided and analyzed below.

Assume the tool on the XYZ table moves a nominal distance in y direction first, then in x direction, and lastly in z direction, as shown in Fig. 2.1. After each movement, the original coordinate may not be valid any more due to rotational and positional errors, and a new coordinate system with the same origin should be established. Also assume axis y is properly aligned compared to axis x, and axis x is properly aligned compared to axis z. So the squareness of the system, α_{xy}, α_{yz} and α_{xz} are defined as shown in Fig.
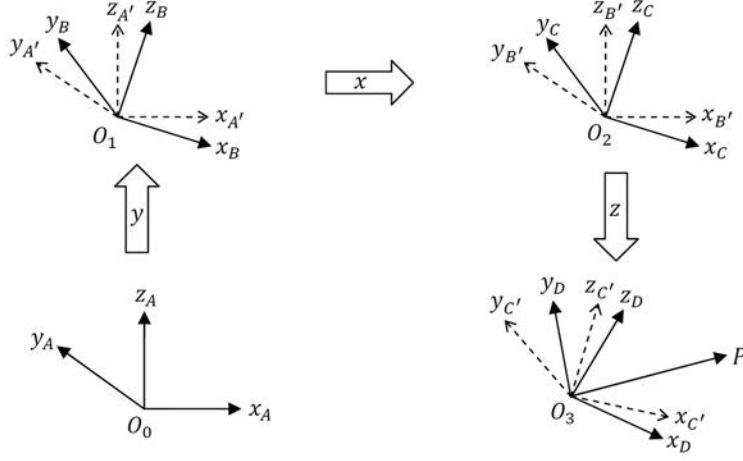
Figure 2.1: XYZ motion analysis
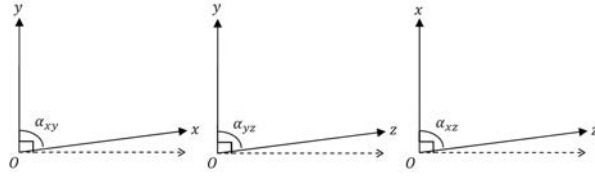
Figure 2.2: Squareness errors

2.2.

The translation movements can be calculated as shown in Eq. 2.1-2.4, where P is position of the tool on the XYZ table, $\delta_u(v)$ is the straightness error along u axis under v direction motion, and $\delta_u(u)$ is the linear error along u axis with motion in the u direction [45]- [48].

$$^A\vec{O_0O_1} = \begin{pmatrix} \delta_x(y) \\ y + \delta_y(y) \\ \delta_z(y) \end{pmatrix} \tag{2.1}$$

$$^B\vec{O_1O_2} = \begin{pmatrix} x + \delta_x(x) \\ \delta_y(x) + cos\alpha_{xy} \cdot x \\ \delta_z(x) \end{pmatrix} \tag{2.2}$$

21

$$^C\vec{O_2O_3} = \begin{pmatrix} \delta_x(z) + cos\alpha_{xz} \cdot z \\ \delta_y(z) + cos\alpha_{yz} \cdot z \\ z + \delta_z(z) \end{pmatrix} \tag{2.3}$$

$$^D\vec{O_3P} = \begin{pmatrix} x_p \\ y_p \\ z_p \end{pmatrix} \tag{2.4}$$

The rotational movements can be calculated as shown in Eq. 2.5-2.7, where $\varepsilon_u(v)$ is the angular error along u axis in the v direction.

$$^{A'}_{B}R(y) = \begin{pmatrix} 1 & -\varepsilon_z(y) & \varepsilon_y(y) \\ \varepsilon_z(y) & 1 & -\varepsilon_x(y) \\ -\varepsilon_y(y) & \varepsilon_x(y) & 1 \end{pmatrix} \tag{2.5}$$

$$^{B'}_{C}R(x) = \begin{pmatrix} 1 & -\varepsilon_z(x) & \varepsilon_y(x) \\ \varepsilon_z(x) & 1 & -\varepsilon_x(x) \\ -\varepsilon_y(x) & \varepsilon_x(x) & 1 \end{pmatrix} \tag{2.6}$$

$$^{C'}_{D}R(z) = \begin{pmatrix} 1 & -\varepsilon_z(z) & \varepsilon_y(z) \\ \varepsilon_z(z) & 1 & -\varepsilon_x(z) \\ -\varepsilon_y(z) & \varepsilon_x(z) & 1 \end{pmatrix} \tag{2.7}$$

So, based on the coordinate transformation theory of rigid body, the total movement is:

$$^A\vec{O_0P} = {}^A\vec{O_0O_1} + {}^{A'}_{B}R(y)^B\vec{O_1O_2} + {}^{A'}_{B}R(y)^{B'}_{C}R(x)^C\vec{O_2O_3}$$

$$+ {}^{A'}_{B}R(y)^{B'}_{C}R(x)^{C'}_{D}R(z)^D\vec{O_3P} \tag{2.8}$$

Substitute Eq. 2.5-2.7 into Eq. 2.8 and note that $\varepsilon_u(v)\delta_u(v) = 0$, $\varepsilon_u(u)\varepsilon_u(v) = 0$, $\varepsilon_u(u)cos\alpha_{uv} = 0$ as $\varepsilon_u(v)$, $\delta_u(v)$, $cos\alpha_{uv}$ are very small, the overall position error model

of the table can be obtained as:

$$^{A}\vec{O_0P} = \begin{pmatrix} \vec{O_0P_x} \\ \vec{O_0P_y} \\ \vec{O_0P_z} \end{pmatrix} \tag{2.9}$$

where

$$\vec{O_0P_x} = x + \delta_x(x) + \delta_x(y) + \delta_x(z) + cos\alpha_{xz} \cdot z + \varepsilon_y(x) \cdot z + \varepsilon_y(y) \cdot z$$

$$+ x_p - y_p \cdot [\varepsilon_z(x) + \varepsilon_z(y) + \varepsilon_z(z)] + z_p \cdot [\varepsilon_y(x) + \varepsilon_y(y) + \varepsilon_y(z)] \tag{2.10a}$$

$$\vec{O_0P_y} = y + \delta_y(y) + \delta_y(x) + \delta_y(z) + cos\alpha_{xy} \cdot x + cos\alpha_{yz} \cdot z + \varepsilon_z(y) \cdot x - \varepsilon_x(x) \cdot z$$

$$- \varepsilon_x(y) \cdot z + x_p \cdot [\varepsilon_z(x) + \varepsilon_z(y) + \varepsilon_z(z)] + y_p - z_p \cdot [\varepsilon_x(x) + \varepsilon_x(y) + \varepsilon_x(z)] \tag{2.10b}$$

$$\vec{O_0P_z} = z + \delta_z(z) + \delta_z(y) + \delta_z(x) - \varepsilon_y(y) \cdot x - x_p \cdot [\varepsilon_y(x) + \varepsilon_y(y) + \varepsilon_y(z)]$$

$$+ y_p \cdot [\varepsilon_x(x) + \varepsilon_x(y) + \varepsilon_x(z)] + z_p \tag{2.10c}$$

2.2.2 RBF approximation

Usually the look-up table method is used to approximate the nonlinear profile of these errors, based on points collected and calibrated for the machine [28] [52] [53]. Literally Edward Troughton was the first to use a look-up table to compensate the displacement errors in the position of the slideway of a linear dividing engine based on previously measured data [52]. In 1970s, R. Hocken was the first one using it in a practical implementation on a CMM system [53].

But there are several significant disadvantages with the look-up table method [48]. Firstly, look-up table requires extensive memory. If data collection of each axis increased by a factor of N for 3D machine, the number of table entries will increase by the order of N^3. This is more significant for high precision machine as a huge amount of calibration

data is necessary. Secondly, linear interpolation is used for the error compensation with intermediate points of the recorded data. Linear estimation may suffice if the calibration is done at very fine intervals, but tremendous memory will be required which may beyond the capacity of a typical look-up table. Thirdly, there is no amenable structure in look-up table for additional conditions like environment and thermal affects. Additional tables are required when those factors are being considered when for a more precise compensation. Finally, tedious search is necessary at every sampling interval for continuous online error compensation, when the table is large in size, especially when the calibration is not done at regular intervals.

Due to the shortcomings of the look-up table method, the coefficient table method is then proposed and used by researchers [42] [43] [54]. In this method, the error functions are in analytical form such as polynomial or Taylor series, and the coefficients of the polynomial are stored in the table in the computer memory [28]. This method can relatively reduce the amount of data stored in the computer memory, but it has a heavier calculation process than the look-up table method. If the error has a strong nonlinearity, very higher order polynomial function is necessary thus it also introduces the inaccuracy risk in selecting the order of each polynomial.

To overcome the above mentioned problems, neural networks such as RBF can be used [49] [50] to estimate those error components. RBF method is a versatile and practical nonlinear function approximator and has several advantages. Firstly, RBF uses parametric model resulting a more manageable manner instead of multitude of

data. Secondly, RBF adopts nonlinear interpolation for compensation of intermediate points resulting smoother error modeling. Thirdly, RBF can be recursively refined based on additional conditions and factors resulting better expansion ability. Fourthly, in RBF the output is computed directly based on input thus no search procedure is required. Finally, compared with many other neural-networks techniques, the training of RBF is more rapid [58]. In the derived error model above, each error component varies with displacement in a nonlinear manner. So in order to estimate those error components, RBF is used for error estimation in this chapter since it can approximate any nonlinear function to any desired level of accuracy.

Derived from function approximation theory, the RBF network is a kind of feed-forward network. They form mappings from an input vector to an output vector. Let $y(x)$ be a smooth function from R to R. Then, given a compact $S \in R$ and a positive number w_M, there exists an RBF network such that with $||w_0|| < w_M$ for all $x \in S$, as shown in Eq. 2.11. Typically Gaussian function is used as the property of universal approximation by linear superposition of Gaussian basis functions has been proved [59].

$$y(x) = \sum_{i=1}^{M} w_i \varphi_i(||x - \mu_i||) + w_0 \tag{2.11}$$

where M is the size of the input vector, w_i is the representative value vector, φ_i is the Gaussian function which $\varphi_i(||x - \mu_i||) = exp(-\frac{||x-\mu_i||^2}{2\sigma_i^2})$, μ_i is the basis center of RBF, and σ_i is the standard deviation.

There are three layers in the RBF networks: an input layer, a hidden layer with RBF activation function and a linear summation output layer, as shown in Fig. 2.3. In
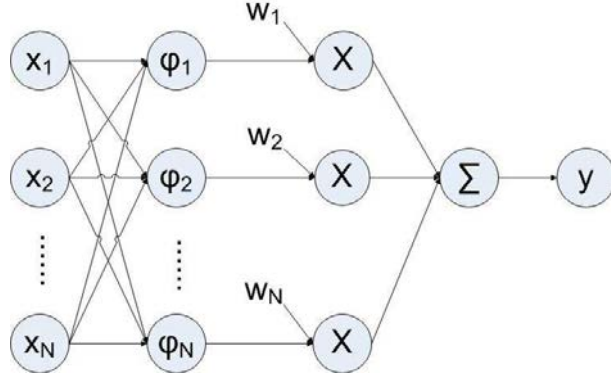
Figure 2.3: Architecture of RBF network

order to calculate the nonlinear functions associated with the various error components, the RBF should be trained using input and output data sets to obtain the function parameters: w and μ so that the set of inputs can produce the desired set of output. Thus, RBF training algorithms are required. There are mainly two methods used in the RBF network training: supervised training with gradient descent and unsupervised training with two-stage procedure. The gradient descent method determines all the parameters at the same time simultaneously via iteratively update process and the two-stage method decouples the training process into two parts by determining the centers and weights separately. The main difference of the two methods is: in the first method both inputs and desired outputs are needed in the training process, and in the second method no desired output is required. Thus the first method may lead to optimal choice of the parameters and the results from the second method may become unpredictable. So in this chapter, the gradient descent method based on error back propagation is adopted for parameter adaptation. Back propagation is a systematic method to train RBF, and has expanded the range of problems where the neural networks can be applied [55]- [57].

In the RBF network shown in Fig. 2.3, and assuming a network with differentiable RBF activation functions, then the necessary condition to achieve a minimal error is the derivatives of back propagated error $E = y_{Ti} - y_i$ vanish with respect to the weights w and basis center μ. An iterative procedure to find a solution is the gradient descent method. Define the parameter set $W = (w_i, \mu_i)$, and η as the learning rate. Before starting the training process, the weights w are initialized to small value. Then the parameter set W should move by a small distance defined by η in the direction in which the back propagated error E decreases most rapidly. The update of the parameters can be obtained in Eq. 2.12, and the discrete time versions of this algorithm are given in Eq. 2.13 and Eq. 2.14 [51]. A termination condition in the form of mean square of error E_{ms} is adopted here to end the iterative adaption process. When the E_{ms} between the actual outputs and the desired outputs reaches the termination condition, the network is said to be trained and the optimum RBF parameters can be obtained. Then the weights w will not be changed and the trained RBF can be used to estimate the required error components based on the inputs. The following algorithm is used in Matlab to train the weights w and centers μ according to the gradient descent back-propagation method:

Algorithm 1 Gradient Descent Back Propagation Method

---

    while $E_{ms} >$ threshold value **do**

        Caculate RBF test output RBF_test with current weights w and basis center μ

        Compute error E between RBF_test and RBF training set RBF_train

        Adjust weights w and basis center μ to minimize E

        Compute and return updated E_{ms}

    end while

$$W(t+1) = W(t) - \eta \nabla E(W(t)) \tag{2.12}$$

$$w_i(t+1) = w_i(t) - \eta_w E \varphi_i(||x - \mu_i||^2) \tag{2.13}$$

$$\mu_i(t+1) = \mu_i(t) - \eta_\mu E w_i \varphi_i(||x - \mu_i||^2)(x_T - \mu_i)/\sigma_i^2 \tag{2.14}$$

where E is the back propagated error $y_{Ti} - y_i$, y_T is the target RBF output, x_T is the ideal RBF input that yields the desired RBF output, η_w and η_μ are the learning rate of w and μ, and σ_i is chosen as a constant.

2.2.3 Geometric error estimation using displacement measurement

Linear error

Linear errors may arise from various sources, like the deficiencies along the guideway or measurement errors. The linear errors can be obtained directly by displacement measurement along each axis. The measured sets of data can be used to train the RBF approximation. With the corresponding function weights, the linear errors of x and y axis can be modeled as:

$$\delta_x(x) = f_{lin,x}(x) \tag{2.15}$$

$$\delta_y(y) = f_{lin,y}(y) \tag{2.16}$$

$$\delta_z(z) = f_{lin,z}(z) \tag{2.17}$$

Squareness error

Squareness error characterizes how far the two axis form a 90 degree orientation. One of the squareness errors α_{xy} can be illustrated in Fig. 2.4. Assume y axis is properly aligned, and the linear movement errors are repeatable. In order to calculate this
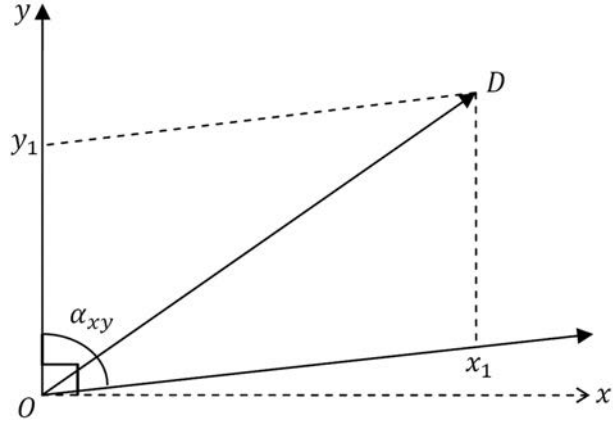
Figure 2.4: Squareness error illustration

squareness error α_{xy}, the face diagonal line OD on xy plane (where $OD_x = x_1, OD_y = y_1$ and plus the linear errors in both axis from the previous models) should be measured using displacement measurement. Here the values of x_1 and y_1 are not necessary equally chosen.

According to the law of cosine:

$$cos(\pi - \alpha_{xy}) = \frac{x_1^2 + y_1^2 - OD^2}{2x_1y_1} \tag{2.18}$$

Then, the squareness error can be obtained:

$$\alpha_{xy} = \pi - arccos(\frac{x_1^2 + y_1^2 - OD^2}{2x_1y_1}) \tag{2.19}$$

Using a similar method, the other two squareness errors α_{yz} and α_{xz} can be obtained by measuring the face diagonal lines on yz plane and xz plane correspondingly. As each squareness error only yields a single constant, no RBF approximation is needed for the squareness error estimation.

Pitch and yaw error
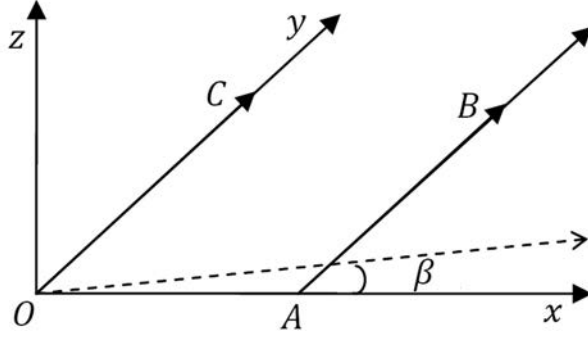
Figure 2.5: Yaw error illustration

Pitch and yaw error is mainly caused by non-uniformity and distortion of the guideway. There are totally six pitch and yaw errors, and one of these errors $\varepsilon_z(y)$ can be referred as the angle β in Fig. 2.5. Usually the value of β is very small, so it is reasonable to assume that:

$$\beta = \sin\beta = \tan\beta = \varepsilon_z(y) \tag{2.20}$$

The movement $AB = l(x_1, y_1, 0)$ along y axis, starting from point $A = (x_1, 0, 0)$, can be measured using displacement measurement and expressed as:

$$l(x_1, y_1, 0) = y_1 + \delta_y(y_1) + \varepsilon_z(y_1) \cdot [x_1 + \delta_x(x_1)] + y_p$$
$$+ x_p \cdot \varepsilon_z(y_1) - z_p \cdot \varepsilon_z(y_1) + \cos\alpha_{xy} \cdot [x_1 + \delta_x(x_1)] \tag{2.21}$$

The movement $OC = l(0, y_1, 0)$ along y axis, starting from origin $O = (0, 0, 0)$ has already been obtained from the linear error measurement:

$$l(0, y_1, 0) = y_1 + \delta_y(y_1) + y_p + x_p \cdot \varepsilon_z(y_1) - z_p \cdot \varepsilon_z(y_1) \tag{2.22}$$

As the value of $\cos\alpha_{xy}$ has been obtained previously, the error $\varepsilon_z(y)$ can be calculated as:

$$\varepsilon_z(y_1) = \frac{l(x_1, y_1, 0) - l(0, y_1, 0)}{x_1 + \delta_x(x_1)} - \cos\alpha_{xy} \tag{2.23}$$

30

Using the RBF approximation, the yaw error of y axis can be modeled as:

$$\varepsilon_z(y) = f_{yaw,y}(y) \tag{2.24}$$

The remaining 5 pitch and yaw errors can also be obtained using the same method by measuring five displacement lines on plane xy, yz and xz correspondingly.

Straightness error

Straightness errors mainly arise from the guideway distortion. As each straightness error only involves two dimensions, the third axis can be isolated when deriving the straightness error. For example, for xy plane movement only and for tables with zero tool offsets, the following equation can be derived from Eq. 2.9:

$$\begin{pmatrix} x \\ y \end{pmatrix} = \begin{pmatrix} x_a + \delta_x(x) + \delta_x(y) \\ y_a + \delta_y(y) + \delta_y(x) + \varepsilon_z(y) \cdot x + cos\alpha_{xy} \cdot x \end{pmatrix} \tag{2.25}$$

The calculation process for straightness error in Eq. 2.25 can be shown in Fig. 2.6. The diagonal xy movement OD, with $OD_x = x_a$ and $OD_y = y_a$, has been measured using displacement measurement in previous section. Then it is apparent that:

$$tan\theta = \frac{y_a}{x_a}, x = cos\theta \cdot OD, y = sin\theta \cdot OD \tag{2.26}$$

From previous discussions on error determinations, the other four errors $\delta_x(x_a)$, $\delta_y(y_a)$, $\varepsilon_z(y_a)$ and $cos\alpha_{xy}$ in Eq. 2.25 have been obtained already, then the two straightness errors can be calculated as:

$$\delta_x(y) = cos\theta \cdot OD - x_a - \delta_x(x) \tag{2.27}$$

$$\delta_y(x) = sin\theta \cdot OD - y_a - \delta_y(y) - \varepsilon_z(y) \cdot x - cos\alpha_{xy} \cdot x \tag{2.28}$$

31
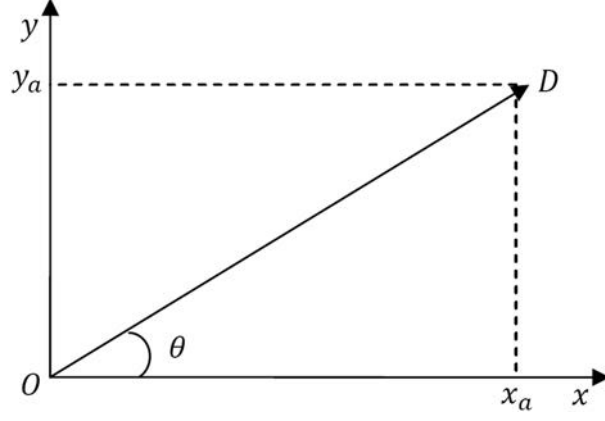
Figure 2.6: Straightness error illustration

The RBF approximation functions of above two straightness errors can be obtained

as:

$$\delta_x(y) = f_{str,x}(y) \tag{2.29}$$

$$\delta_y(x) = f_{str,y}(x) \tag{2.30}$$

The remaining four straightness errors can be obtained by isolating x axis or y axis

correspondingly and measuring two arbitrary planar lines.

Roll error

Similar to pitch and yaw errors, roll errors are also mainly caused by non-uniformity

and distortion of the guideway. There are totally three roll errors: $\varepsilon_x(x), \varepsilon_y(y)$ and $\varepsilon_z(z)$,

and the measurement process is shown in Fig. 2.7, where the z_1E_1 and z_2E_2 are diagonal

lines on xy plane with $z = z_1$ and $z = z_2$ respectively. For tables with zero tool offsets,
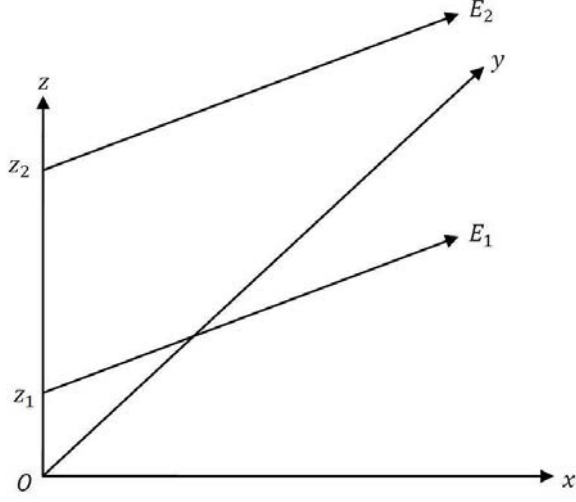
Figure 2.7: Roll error illustration

the following equations can be derived from Eq. 2.9:

$$z_1 E_1(x) = x + \delta_x(x) + \delta_x(y) + \delta_x(z_1) + cos\alpha_{xz} \cdot z_1 + \varepsilon_y(x) \cdot z_1 + \varepsilon_y(y) \cdot z_1 \quad (2.31a)$$

$$z_1 E_1(y) = y + \delta_y(y) + \delta_y(x) + \delta_y(z_1) + cos\alpha_{xy} \cdot x + cos\alpha_{yz} \cdot z_1$$

$$+ \varepsilon_z(y) \cdot x - \varepsilon_x(y) \cdot z_1 - \varepsilon_x(x) \cdot z_1 \quad (2.31b)$$

and

$$z_2 E_2(x) = x + \delta_x(x) + \delta_x(y) + \delta_x(z_2) + cos\alpha_{xz} \cdot z_2 + \varepsilon_y(x) \cdot z_2 + \varepsilon_y(y) \cdot z_2 \quad (2.32a)$$

$$z_2 E_2(y) = y + \delta_y(y) + \delta_y(x) + \delta_y(z_2) + cos\alpha_{xy} \cdot x + cos\alpha_{yz} \cdot z_2$$

$$+ \varepsilon_z(y) \cdot x - \varepsilon_x(y) \cdot z_2 - \varepsilon_x(x) \cdot z_2 \quad (2.32b)$$

By checking Eq. 2.31 and Eq. 2.32, the only unknown variables are $\varepsilon_y(y)$ and $\varepsilon_x(x)$, as the rest error components are already determined previously. So with two equations describing by comparing $z_1 E_1$ and $z_2 E_2$, the roll error of x and y axes $\varepsilon_x(x)$ and $\varepsilon_y(y)$

33

Figure 2.8: Aerotech XY table

can be determined accordingly. The roll error of z axis can also be calculated with a diagonal measurement along xz or yz plane, as the roll errors of x and y axes are known already. Then the RBF function for $\varepsilon_u(u)$ of u axis can be obtained as:

$$\varepsilon_u(u) = f_{poll,u}(u) \tag{2.33}$$

2.3 Experiment on XY Tables

2.3.1 Error identification and compensation on Aerotech XY table

To validate the proposed model of geometrical errors compensation, an XY table made by Aerotech with linear servo motors is used as the experimental platform, as shown in Fig. 2.8. The tool attached to the table can be moved in either X or Y direction, and span a 200 mm × 200 mm 2-D space. Digital driver and encoders are used in both axes with 1μm resolution.

Since there is no probe used in this experiment, the tool offset of this XY table is

34

Table 2.1: Geometric Errors for XY Table

Error Symbol	Error Type
$\delta_x(x)$	Linear error of x axis
$\delta_y(y)$	Linear error of y axis
$\delta_y(x)$	Straightness error of x axis
$\delta_x(y)$	Straightness error of y axis
$cos\alpha_{xy}$	Squareness error of xy axis
$\varepsilon_z(y)$	Yaw error

zero, i.e. $x_p = y_p = z_p = 0$, from Eq. 2.9, the total error model will be:

$$^A\vec{O_0}P = {}^A\vec{O_0O_1} + {}^{A'}_B R(y) \cdot {}^B\vec{O_1O_2} \tag{2.34}$$

where

$$^A\vec{O_0}P(x) = x + \delta_x(x) + \delta_x(y) \tag{2.35a}$$

$$^A\vec{O_0}P(y) = y + \delta_y(y) + \delta_y(x) + \varepsilon_z(y) \cdot x + cos\alpha_{xy} \cdot x \tag{2.35b}$$

$$^A\vec{O_0}P(z) = \delta_z(y) + \delta_z(x) - \varepsilon_y(y) \cdot x \tag{2.35c}$$

For XY plane motion, the movement of z axis can be assumed to be zero, so the final error model can be mathematically described as:

$$^A\vec{O_0}P = \begin{pmatrix} x + \delta_x(x) + \delta_x(y) \\ y + \delta_y(y) + \delta_y(x) + \varepsilon_z(y) \cdot x + cos\alpha_{xy} \cdot x \end{pmatrix} \tag{2.36}$$

For a 2-D machine like this XY table, the total geometric errors reduced to six components: two linear errors, two straightness errors, one angular error (yaw error) and one squareness error, as shown in Table 2.1. The overall position error is accumulated by these errors, and a mathematical error model is provided below.

The error data sets to be used for RBF training are collected using laser interferometer and displacement measurement optics only, and the experiment setup is shown in Fig.

2.9. Only displacement optics are used in raw data measurement for the error modeling using RBF estimation, and full optics are used to measure all the geometric errors as references. The comparison between the RBF estimation of raw data and reference data can be used to validate the proposed method.

Based on the proposed method, four displacement lines are to be measured, as shown in Fig. 2.10, where line ① is along X direction with $y = 0$, line ② is along Y direction with $x = 0$, line ③ is an arbitrary chosen diagonal line of XY table, and line ④ is along Y direction with an arbitrary offset $x = x_1$. The raw data collection is done at 5 mm intervals along the 200 mm travel range including origin for both X and Y axis. Hence a total of 41 data points are collected for each displacement line to be measured. To minimize the effects of random influence, three cycles of data are collected for each line in both forward and backward directions. The average value of those raw data is used and RBF approximation is applied to each displacement separately to compute the geometric error. Fig. 2.11 shows the linear error measurements along the X axis, and the differences between the raw errors in each measurement cycle are all less than 1 μm, which is the resolution of the XY table. This shows that the geometric errors in the XY table with linear motors are not path related.

For the modeling of the error components, a total of five RBF are required to be trained separately. Here each RBF network is trained using 41 samples of data which are averaged values from three cycles of bidirectional operations. Thus $M = 41$ and $\sigma = 0.05$ are selected for the RBF training. As the parameter adaptation process is done

offline with pre-acquired data, a longer training time with a relative small value of the mean square error can be used to get better fitting results. Thus $E_{ms} < 0.001$ is selected as the terminating condition for parameter adaption, and the learning rate η_w and η_μ are chosen at 0.01. The training time for each RBF network with 41 samples of data takes a few seconds only with small variations due to the convergence time, with the weights w and basis center μ updating according to the Eq. 2.13 and Eq. 2.14. As discussed in Section 2.2.2, the parameter adaptation process will converge according to gradient descent back-propagation method. When each RBF training process converges to the terminating condition, the trained weights w and centers μ are available to commission the RBF estimation of error components.

The results of the RBF approximation are shown in Fig. 2.12 to Fig. 2.16, where the circles represent the measured raw data, the solid lines represent the corresponding RBF approximation and the asterisk-lines represent reference data. The raw data are the estimated error components using the proposed method based on measurement using displacement optic only, the RBF approximations are the estimated continuous error components using RBF based on the raw data, and the reference data are the directly measured error components using full optic sets. Thus the reference data can be treated as a reference to validate the proposed error estimation method.

In Fig. 2.14, 2.15 and 2.16, there are local differences between reference data and the RBF approximation. The reason is because the reference data and RBF approximation are obtained using different methods at different cost: reference data is obtained directly

Table 2.2: Estimated Errors for XY Table

Error components	Value
Linear error of x $\delta_x(x)$	N.A.
Linear error of y $\delta_y(y)$	N.A.
Yaw error $\varepsilon_z(y)$	0-4 $arcsec$
Straightness error of x $\delta_y(x)$	0-4.5 μm
Straightness error of y $\delta_x(y)$	0-2 μm
Squareness error $cos\alpha_{xy}$	40 $arcsec$

using full optical sets (e.g. angular optics are needed to measure angular errors, square optics are needed to measure square errors), while RBF approximation is computed from displacement data obtained from linear optics only. The accuracy of the encoder of the system is 1 μm only, and the difference of encoder measured data and laser optics measured data can reach up to 6 μm along the X axis and 4 μm along the Y axis from Fig. 2.12 and Fig. 2.13. During the computation of RBF approximation, multiple displacement data are involved. Although repeatable errors may cancel during the computation, but such cancellations cannot be achieved for non-repeatable errors. So it is reasonable to have some micrometers difference from the reference data which are measured directly from corresponding optics. From Fig. 2.14 to Fig. 2.16, the RBF approximation is able to track the shape of the reference data, with maximum differences of 2-4 μm, which means a good range of errors can be compensated with this approach.

Besides those plots, the estimated squareness error of XY is 899.9660 $arcsec$, while the measured data is 859.96 $arcsec$. A summary of the error components based on the RBF estimation and reference results can be obtained as shown in Table 2.2. It can be observed that the outputs of RBF estimation can follow the reference errors closely.

38
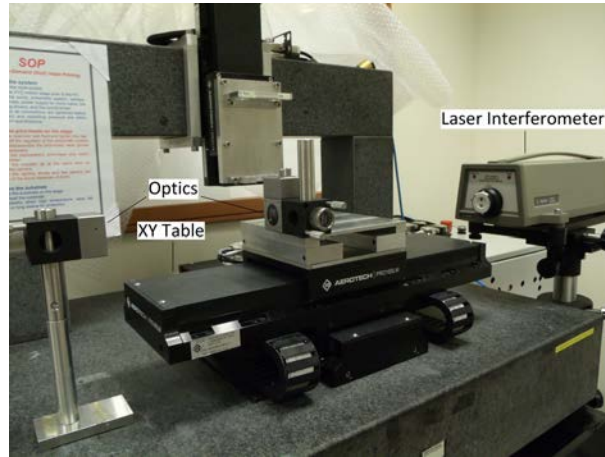
Figure 2.9: Experimental setup
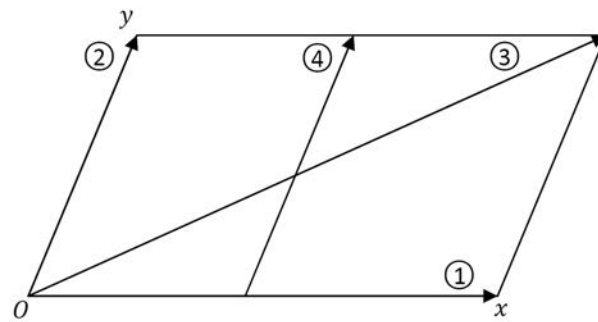
Figure 2.10: Displacement measurements
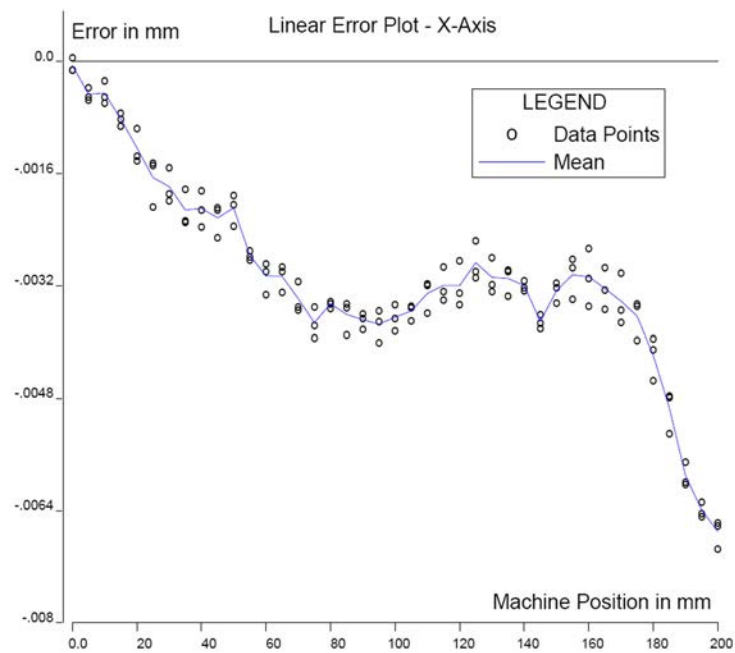
Figure 2.11: Raw data of X axis linear error

39
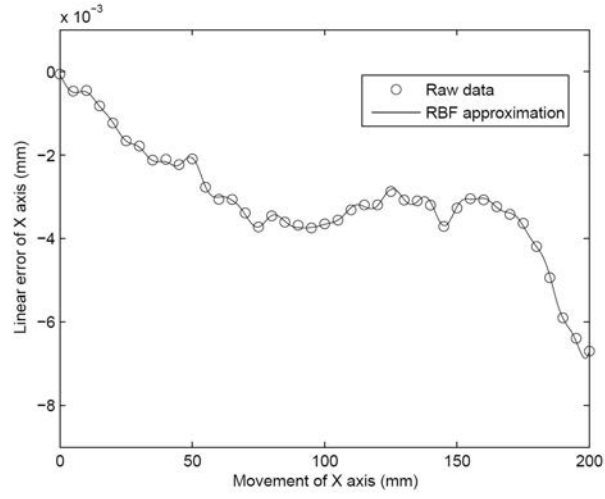
Figure 2.12: RBF approximation of X axis linear error $\delta_x(x)$
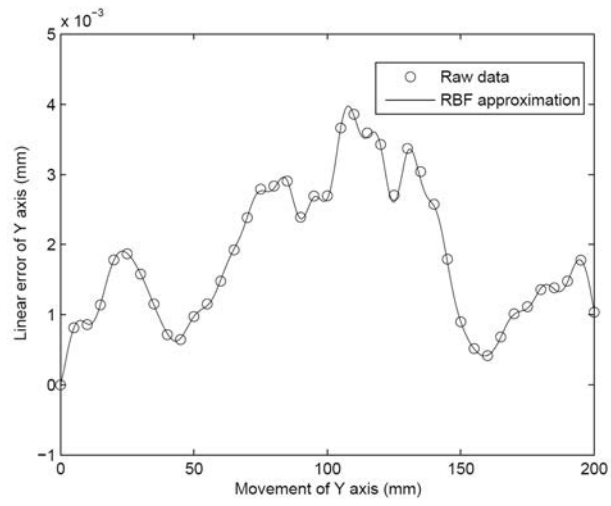
Figure 2.13: RBF approximation of Y axis linear error $\delta_y(y)$
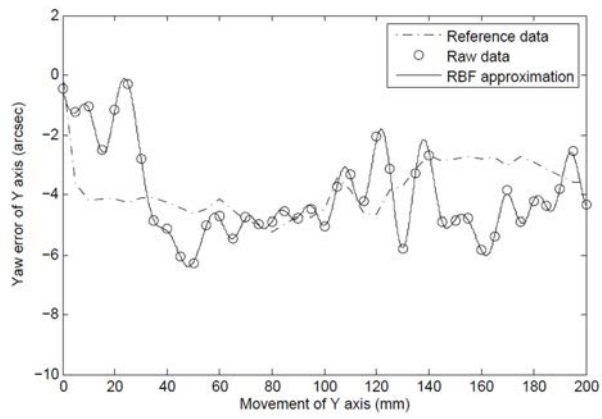
Figure 2.14: RBF approximation of yaw error $\varepsilon_z(y)$
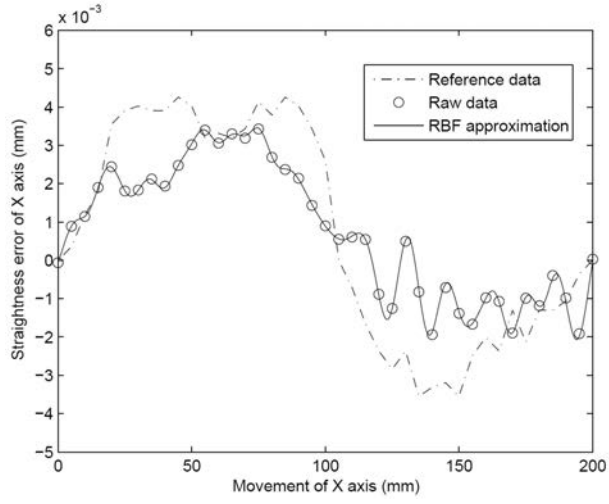
Figure 2.15: RBF approximation of straightness error of X axis $\delta_y(x)$
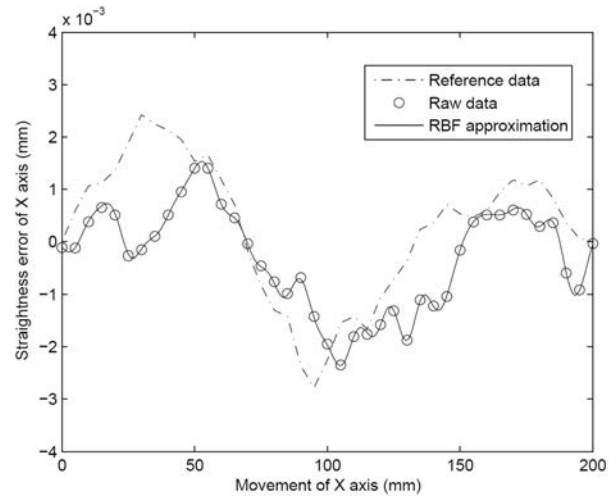
Figure 2.16: RBF approximation of straightness error of Y axis $\delta_x(y)$
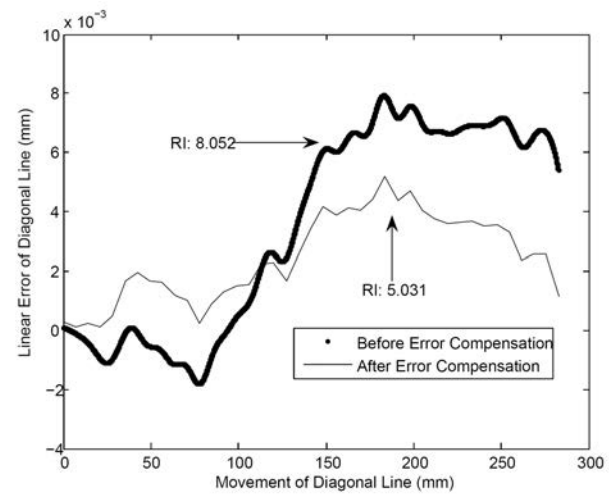
Figure 2.17: Error compensation result for Aerotech XY table

Table 2.3: Results of Different Data Intervals

Data Interval(mm)	Error RI($10^{-7}m^2$)
5	5.031
10	5.730
20	5.843
25	5.920
40	5.969
50	6.124

With those estimated error components, the system performance after error compensation can be obtained by measuring the diagonal line as shown in Fig. 2.17, where RI abbreviates 'Riemann Integral'. It can be observed that the maximum error is 4μm, instead of 8μm before error compensation. In order to observe the effect of the amount of raw data collected on the estimated results, different data collection intervals along the axis have been selected and the corresponding compensation outcomes have been shown in Table 2.3 as well, where Riemann integral of the error after compensation is used for comparison. With data collection at lower density, the calibration time can be significantly reduced, and it can observed that the accuracy can be still controlled within a certain level. This is very useful for machines requiring relatively lower level of accuracy but fast calibration, like acceptance testing and periodic checking.

2.3.2 Error compensation on WinnerMotor XY table

Another XY table with 200mm$\times$200mm 2-D work spacemade by WinnerMotor as shown in Fig. 2.18 is investigated in this section. In this machine, digital driver and encoder is used in X axis, while analog driver and encoder is used in Y axis. This machine is a good investigation platform using the proposed error compensation method for fast

Figure 2.18: WinnerMotor XY table

calibration and compensation.

In order to access the performance of the error compensation, both axes are controlled to move the carriage along the diagonal line of the working area, with the ratio of the positions of y and x set as $y = kx$. The linear errors are measured along the movement path of the carriage using laser interferometer system and a total of 41 points along the maximum working range of the machine are measured with and without error compensation. The results when $k = 1$ and $k = 0.5$ are shown in Fig. 2.19 to Fig. 2.22, and it can be seen that the errors can be as high as 0.4mm at the end of the test range and 140μm for short range of 70mm. After compensation, the error can be controlled within the range of 0.1mm for the full test range and 10μm for short range of 70mm. The detailed analysis for error compensation outcome of this machine is shown in Table 2.4.
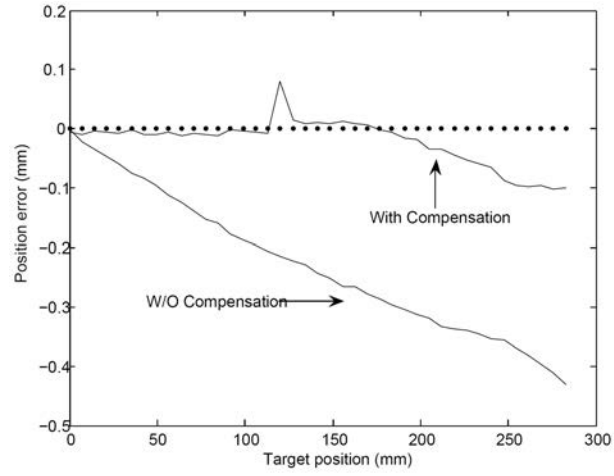
Figure 2.19: Position errors for $y = x$ measurement
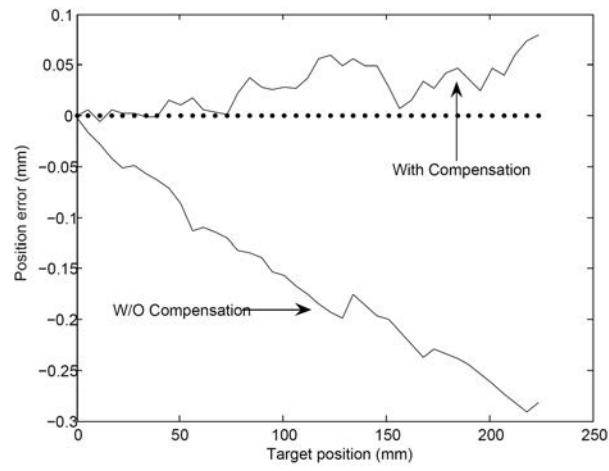
Figure 2.20: Position errors for $y = 0.5x$ measurement
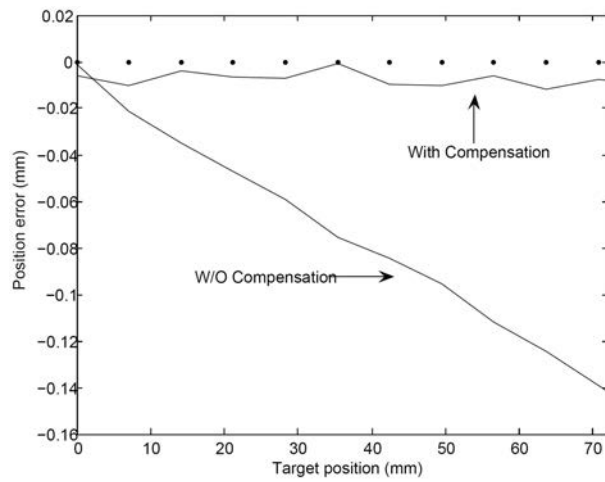
Figure 2.21: Position errors for $y = x$ measurement within 70mm

44
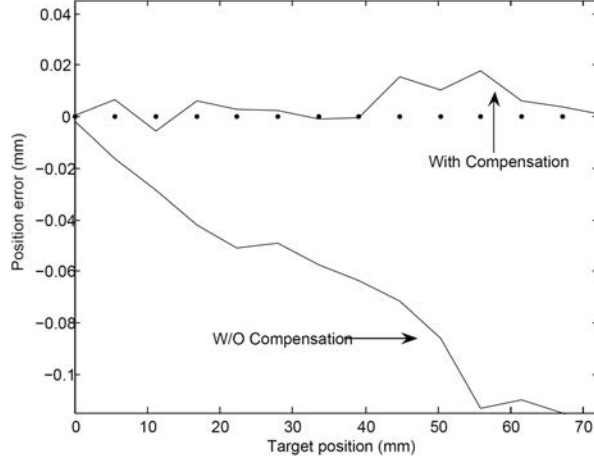
Figure 2.22: Position errors for $y = 0.5x$ measurement within 70mm

Table 2.4: System Geometric Error Analysis

Measurement	Bef.Comp.	Aft.Comp.	Improvement
Y=X, 200mm	Max 0.43mm	Max 0.1mm	76.74%
Y=X, 70mm	Max 0.15mm	Max 0.01mm	93.33%
Y=0.5X, 200mm	Max 0.29mm	Max 0.07mm	75.86%
Y=0.5X, 70mm	Max 0.12mm	Max 0.02mm	83.33%

2.4 Conclusion

In this chapter, a new method for error compensation using only displacement measurement has been proposed for geometric error compensation of precision motion systems. The geometric model is formulated based on individual error components, and these error components are estimated based on the raw data obtained with displacement measurements only using laser interferometer. Compared with previous methods, different measurement methods for straightness and square errors are adopted in this approach. The measured raw data are modeled using RBF instead of the traditional look-up table for error compensation in the controller. In this approach, four and fifteen displacement lines are required to identify the six and twenty-first geometric errors for XY and XYZ

table. The proposed method can significantly increase the system accuracy and decrease the calibration and measurement time. It is also possible to use different intervals of calibration points to reduce the calibration time and maintain a high level of accuracy according to different user requirements.

Chapter 3

Displacement and Thermal Error Identification and Compensation

3.1 Introduction

The relative position errors between the end-effector of the machine and the workpiece in precision machine can be classified into two categories: random errors which are very difficult to be completely eliminated and systematic errors which are repeatable. Among the repeatable errors, thermal errors represent one of the largest contributors, as up to 75% of the overall geometrical errors of machined workpieces can be induced by thermal effects [61]. Generally, the thermal errors of machine tool can be divided into two categories: position-independent and position-dependent errors [62]. The first category is only correlative with temperature but not related to axis coordinate or command position, and the corresponding thermal deformation may cause offset in machine's origin position and tilt in the spindle. The second category is related to both temperature and coordinate positions, and the corresponding thermal deformation may cause errors along the movement path.

There are generally three methods which can be used to reduce thermal errors [62]: 1) Thermal error control: by maintaining the operational temperature using a cooling system; 2) Thermal error avoidance: by re-designing the system like using thermally insensitive materials; 3) Thermal error compensation: by compensating geometric errors introduced by thermal deformation. The first two methods can reduce the thermal errors effectively. But it is very difficult to precisely predict the machine behaviors at the design stage due to reasons such as the thermal expansion coefficients differing with materials; it is also not possible to maintain environment temperature in open space. The first two methods may also significantly increase the cost. Thus, thermal error compensation is more easily facilitated and cost efficient, as the algorithm can be easily implemented and executed in the machine controller and no further modification of the machine is needed.

Research has been conducted on the compensation of thermal errors, both in the position-independent and the position-dependent categories [63]- [73]. Among them, mathematical expressions were used to model the thermal errors, like statistical regression [67] and polynomial fit method [68] [69]. But to find suitable polynomial orders for all the errors involved requires time and this also increases the design complexity. As a result, some researchers used artificial neural networks to predict thermal errors from discrete temperature measurements and compensate the thermal deformation [71]- [73]. Neural networks can be used as an ideal tool for non-linear modeling like geometric errors [25]. As the thermal error of machine tools is generally a function of tempera-

ture [27], Chen [71] and Yang [72] used time-based temperature measurements to train the neural networks and predict the trend of the thermal errors for the compensation, but no position information was used to train the neural networks. Mou [73] also used time-based temperature measurements to train the neural networks, and kinetic modeling was used to predict the thermal errors based on neural network outputs and position measurements. From observations during the experiments, thermal errors are related to both temperature and position information. So in this chapter, both measured temperature and position data are used as inputs to train 2D RBF networks.

As the heat generated during cutting or milling operation is one of the major heating factors affecting the final accuracy of the system, the target of this chapter is to develop an effective and simple real time system to compensate both displacement errors and thermal errors in a milling machine. As both displacement errors and thermal errors are dynamic errors with non-linear characteristics, the RBF which can approximate any nonlinear function to any desired level of accuracy, is used to approximate the errors for online compensation. No order estimation of polynomial or kinetic modeling is required. Since the heat generated during milling operation is mainly from the end-effector which is usually on the slide, a heat sensor attached to the slide and a heating pad is used to simulate the thermal effects of milling operations. The rest of the chapter is organized as follows: Section 3.2 describes the error modeling for 3D machine, including the selection and training of the RBF and the measurement and estimation of the errors for 3D machine, Section 3.3 describes the system setup in both temperature control subsystem

and position control subsystem, Section 3.4 discusses and analyzes the experiment results and Section 3.5 concludes this chapter.

3.2 System Error Modeling

For 3D positioning machines, there are totally 21 geometric error components: 3 displacement errors, 3 squareness errors, 6 straightness errors and 9 angular errors [44]. The overall positional inaccuracies is accumulated by those error components. All of those error components are temperature dependent due to the thermal distortions and expansions in the machine [63]- [73]. So an error compensation model is necessary if high precision movement needs to be satisfied.

Fig. 2.1 shows the movement trace of the tool on a 3D machine. Define $\delta_u(v, T)$ as the straightness error along u axis along the v direction motion at an operating temperature of T, $\delta_u(u, T)$ as the displacement error along u axis with motion along the u direction at an operating temperature of T, $\varepsilon_u(v, T)$ as the angular error along u axis along the v direction at an operating temperature of temperature T, and $\alpha_{uv}(T)$ as the squareness error between u and v axes at an operating temperature of temperature T. With the rotational and positional errors, the overall position error model of the machine without tool offset is shown in Eq. 3.1, similar to Eq. 2.8. In order to build the error compensation model and calibrate the machine, all of the 21 errors should be measured within the operation span of the machine under different machine temperatures [62] [40].

$$^A\vec{O_0P} = \begin{pmatrix} \vec{O_0P_x} \\ \vec{O_0P_y} \\ \vec{O_0P_z} \end{pmatrix} \tag{3.1}$$

50
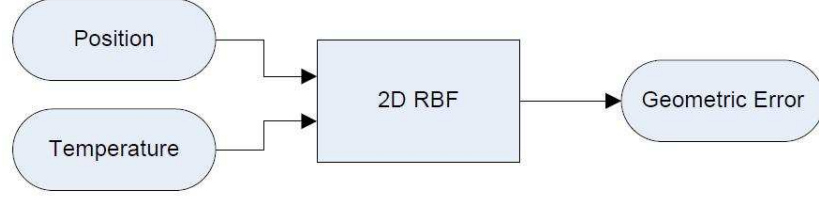
Figure 3.1: Flowchart of 2D RBF network

where

$$\vec{O_0 P_x} = x + \delta_x(x, T) + \delta_x(y, T) + \delta_x(z, T) + cos\alpha_{xz}(T) \cdot z$$

$$+ \varepsilon_y(x, T) \cdot z + \varepsilon_y(y, T) \cdot z \tag{3.2a}$$

$$\vec{O_0 P_y} = y + \delta_y(y, T) + \delta_y(x, T) + \delta_y(z, T) + cos\alpha_{xy}(T) \cdot x$$

$$+ cos\alpha_{yz}(T) \cdot z + \varepsilon_z(y, T) \cdot x - \varepsilon_x(x, T) \cdot z - \varepsilon_x(y, T) \cdot z \tag{3.2b}$$

$$\vec{O_0 P_z} = z + \delta_z(z, T) + \delta_z(y, T) + \delta_z(x, T) - \varepsilon_y(y, T) \cdot x \tag{3.2c}$$

3.2.1 RBF approximation

In the derived error model above, each error component varies with both displacement and temperature in a nonlinear manner. To estimate those error components, neural networks like RBF can be used [49] [50]. In this chapter, RBF networks are required to be trained to obtain the relationship between the geometric error and the motor temperatures and the displacement positions. The RBF networks have a 2-DOF (degree-of-freedom) because the error characteristics depend on both motor temperatures and the displacement positions, as shown in Fig. 3.1.

51

3.2.2 Error measurement and estimation

Linear error

The 2-DOF RBF model of the displacement errors can be trained based on the measurement results by displacement measurements along each axis using linear optics, under different temperatures.

Squareness error

The squareness errors can be obtained by measurements on each plane using optical square and straightness optics, under different temperatures. 1-DOF RBF approximation for each squareness error is adequate as it can be assumed to be position independent.

Straightness error

The straightness errors can be obtained by measuring on each plane using straightness optics, under different temperatures. The measured sets of data can be used to train the 2-DOF RBF networks.

Angular error

There are three types of angular errors: roll, pitch and yaw errors. For pitch and yaw errors, the measurements can be done using angular optics along the corresponding axis under different temperatures. For roll errors, as it is not possible to make direct measurement using laser interferometer and optics, a possible measurement process is shown in Fig. 2.7. Then the 2-DOF RBF networks can be trained based on the measured sets of data.

3.3 System Setup

The main objectives of system setup are to monitor the operational temperature of the system in real time, and to measure the motor positions and errors accurately. The equipments used in the experiment are: $24V$ heating pad, thermistor ($1K\Omega$ at 25°C), temperature controller and NI DAQ for the temperature control part; an Akribis DC linear motor, dSpace control card and the Agilent laser interferometer for the motion control part.

3.3.1 Temperature monitoring and control

A single axis DC motor stage is used in this experiment. In order to simulate the situation when the motor is heated during operations, a heating pad is attached on the slide directly, as shown in Fig. 3.2. This heating pad is controlled by a temperature controller and can reach maximum 70°C when continuously heated.

A thermistor is attached to the slide to measure the real time temperature of the slide, and its resistance-temperature characteristic is calibrated to follow the following equation:

$$R_T = R_B * exp(\frac{\alpha}{100} * (T_B + K)^2 * (\frac{1}{T + K} - \frac{1}{T_B + K}))$$ (3.3)

where K is the temperature constant which equals to 273.15, R_T is the thermistor resistance at temperature T, R_B is the known thermistor resistance at known temperature T_B, and α is the temperature coefficient at temperature T_B.

Based on the previous equation, the temperature of the slide can be calculated when

the thermistor resistance is measured. Thus, a simple sensor circuit is built and NI DAQ is used to read in the resistance of the thermistor and calculate the temperature, as shown in Fig. 3.2. The output of the DAQ is used to control the heating pad controller. A PID closed loop control is written in LabVIEW to control the temperature of the slide to reach the required temperature during experiments. The control structure of the temperature measurement system is shown in Fig. 3.3.

The thermistor sensor is attached to the slide which is the most sensitive temperature spot in this experiment, as the location of the heating pad is on the slide too. The measured thermal errors are also very sensitive to the temperature measured at this location, which would be shown in Section 3.3.3. Thus, one thermistor sensor which is fixed on the slide (without touching the heating pad) is enough to monitor the temperature. If it can be confirmed that there are other heating sources which may cause expansion or distortion at different locations of the machines, more thermistor sensors can be mounted near those locations to monitor the real time temperatures. If in real applications where it may not be viable to attach contact type thermal sensor directly to those locations like the machine spindle, non-contact thermal camera method [74] can be used to monitor the real time temperatures. The machine can be divided into different zones according to the dependency of the thermal errors on the readings of each temperature sensor, then compensation can be applied for each zone separately.
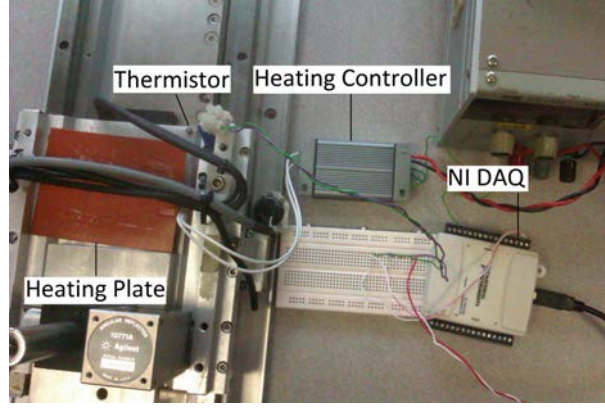
Figure 3.2: Temperature control system setup
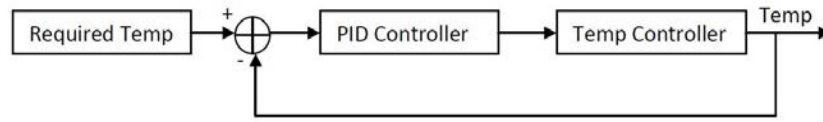
Figure 3.3: Temperature control structure

3.3.2 System position measurement

A single axis DC linear servo motor stage manufactured by Akribis is used as the experimental platform. The slide attached on the stage can move bi-directionally along the X axis, with a working range of 200 mm. Digital driver and encoders are used in this axis with a 1.25μm resolution. According to Eq. 3.1, only X axis displacement error exists in the measurement of 1-dimensional motor stage and the measurement results can be interpreted as Eq. 3.4:

$$x_{meas} = x + \delta_x(x, T) \tag{3.4}$$

where x_{meas} is real movement position, x is the required movement position and $\delta_x(x, T)$ is the displacement error in x axis related to both position x and temperature T. This displacement error during the motor movement can be collected using laser interferometer and linear measurement optics, and the corresponding setup is shown in Fig.

55
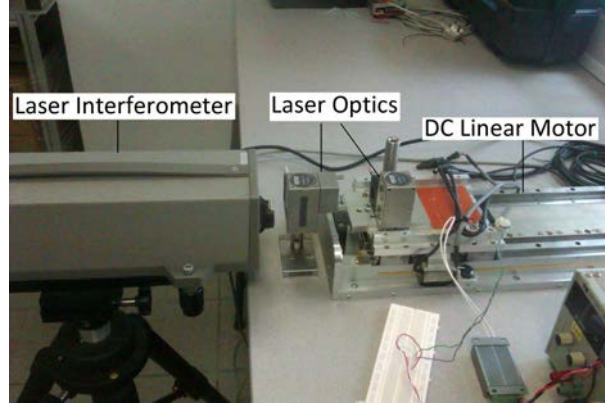
Figure 3.4: Motor position measurement setup

3.4.

3.3.3 System tests

Tests are conducted to observe the characteristics of the thermal errors based on the measured slide temperature and slide positions. The thermal errors are measured using laser interferometer at several slide positions with a fixed power of the heating pad. The slide is heated from room temperature (around 26.8°C) to 30°C. The thermal errors at different positions are shown in Fig. 3.5. It can be observed that at the same slide position, the thermal errors increases (in negative Y direction) when the slide temperature increases; and at a nearer slide position, the thermal errors are smaller. So the thermal errors of this machine depend on both slide temperature and slide position.

The tests results can be explained physically. Generally, for a small change in temperature, the change in the linear dimension of solid can be estimated as:

$$\Delta L = \beta L \Delta T \tag{3.5}$$

where β is the linear expansion coefficient, L is the length of the solid and ΔT is the

56
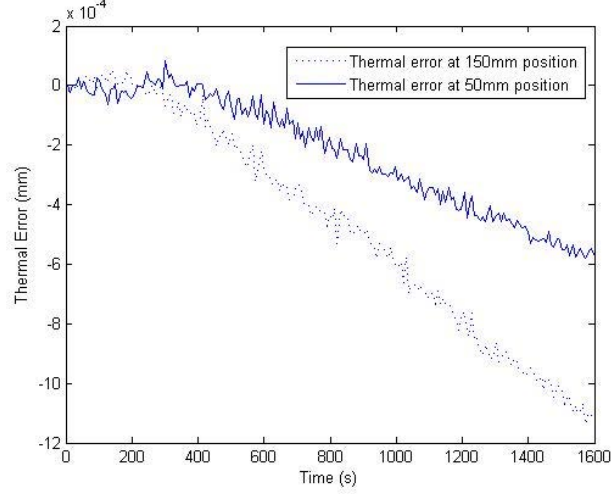
Figure 3.5: Thermal error at different slide position

change in temperature. As the temperature of the slide increases due to the heating

process, the slide expands. Thus, the reflector optic fixed on the slide moves nearer to

the interferometer optic and the distance measured by laser interferometer is shorter.

3.4   Experimental Results and Analysis

To illustrate the effectiveness of the proposed method, real-time experiments are con-

ducted. In the experiments, the linear motor stage is used to simulate a milling machine,

so the only heating source is at the slide. Thus, the heating pad is fixed on the slide

to simulate the heat generated during milling process, and the thermistor is also fixed

on the slide without touching the heating pad to measure the temperature. Based on

the proposed method, the displacement data is measured along the X axis direction at

different temperatures.

The motor system is controlled by Elmo motor driver, and the raw data collections are

done at 5 mm intervals along the 200 mm travel range from the defined origin. Hence,

a total of 41 data points are collected for each displacement line, measured at each temperature. The surface temperature of the slide at the room temperature without air-conditioner is around 26.8°C. The displacement data are collected four times using laser interferometer when the temperature readings show 27, 28, 29 and 30°C. Due to the limited power of the heating pad and the high heat diffusivity of the metal surface of the motor stage, thermal equilibrium is reached at 30°C so measurements above 30°C are not possible (although the heating pad is able to reach 70°C, the surface of the slide is still fixed around 30°C). To minimize the effects of random influence, three cycles of data are collected for each line in both the forward and backward directions at each temperature. The average values of those raw data are used and RBF networks are trained based on those values, as shown in Fig. 3.6, where the raw data are indicated using asterisks.

To obtain the modeling of the displacement error in the one-dimensional linear stage, only one RBF network is necessary. The RBF network for the displacement error $\delta_x(x, T)$ in Eq. 3.4 is trained with the measurement displacement errors, based on both displacement positions and the slide temperatures, using the following equation:

$$\delta_x(x, T) = f_{lin,x}(x, T) \tag{3.6}$$

where $\delta_x(x, T)$ represents the linear error of the motor, x represents the displacement position, and T represents the motor temperature. The training process is done offline with pre-acquired raw data and the parameters are finely tuned to avoid over-fitting problem. The 2D and 3D results from the trained 2-D RBF network are shown in
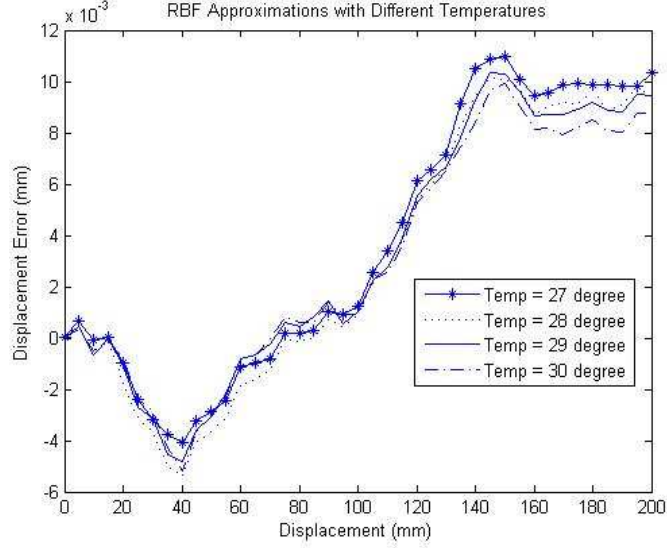
Figure 3.6: RBF approximations with different temperatures (2D)

Fig. 3.6 and Fig. 3.7 separately. In Fig. 3.6, the straight lines represent the RBF approximations, and the asterisks represent the reference data at each temperature. It can be observed that for the Akribis motor in the experiment, the displacement errors decrease when the motor temperature increases.

To validate the effect of the proposed method, the system performance with and without the proposed compensation method should be compared, under both fixed temperature and varying temperature cases. In the fixed temperature situation, the temperature is maintained at $28.5°$C which is at the mid-point of the temperature range in experiments. In the varying temperature situation, the temperature is controlled to follow the designed trace shown in the Fig. 3.8. The compensation process is done using the RBF approximation results as a feedback to the reference position command in the motor controller with the help of dSpace controller. The results for both cases are shown in Fig. 3.9 and Fig. 3.10, where the solid line shows the system performance after er-
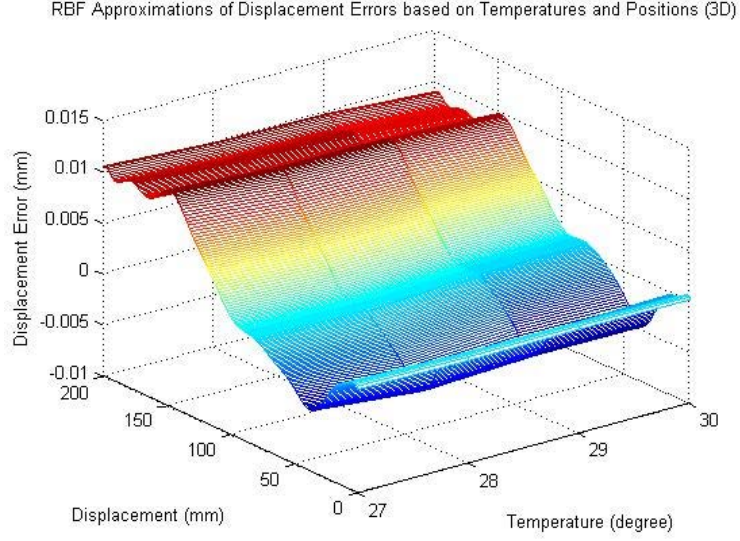
Figure 3.7: RBF approximations with different temperatures (3D)
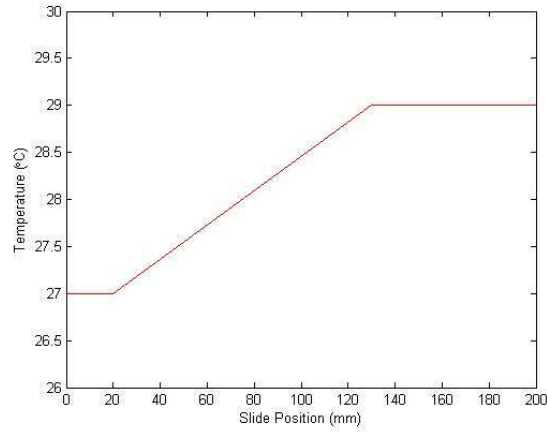
Figure 3.8: Designed temperature trace

ror compensation using the proposed RBF approximation method and the dotted line shows the system performance after error compensation based on geometric error compensation only without thermal error compensation at room temperature. It can be observed that the displacement error is reduced to between -2μm to 1.5μm with proposed method, compared to between -6μm to 5μm with normal compensation method at room temperature (i.e., without considering the temperature changes).

60
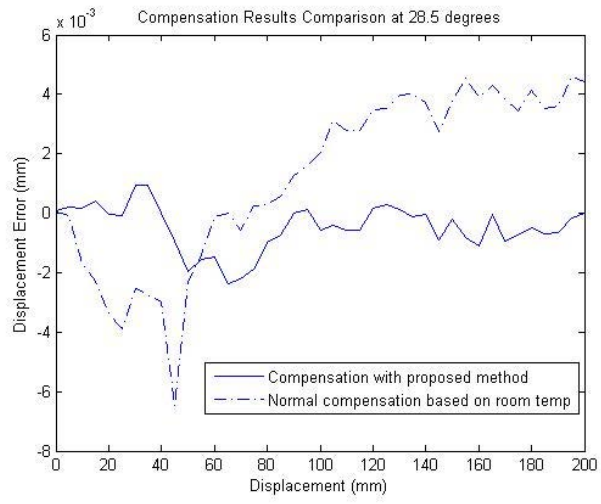
Figure 3.9: Compensation results comparison at 28.5°C
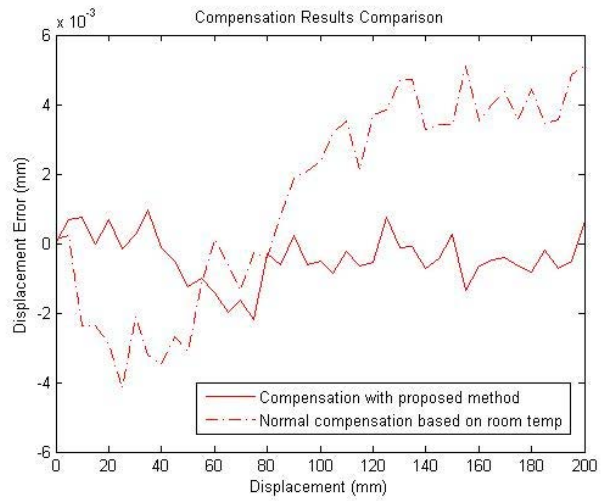
Figure 3.10: Compensation results comparison at varying temperatures

3.5 Conclusion

In this chapter, a RBF-based displacement error and thermal error compensation approach is proposed and developed. The displacement errors are related to both movement positions and the machine operational temperature. The raw data are measured using laser interferometer, and the temperature sensor. A 2D RBF network is trained to model and estimate the displacement errors, instead of the traditional look-up table for error compensation in the controller. The precision and effectiveness of the proposed method is verified through experiments.

Chapter 4

Selective Control Approach Towards Precision Motion Systems

4.1   Introduction

High precision motion control is a core requirement in many industries leveraging on precise robotics and automation such as semiconductor manufacturing, precision machining and metrology. The measurement accuracy sustainable in an application relies critically on the precision and resolution of the position sensors used as well as other important characteristics such as response time, bandwidth, robustness to environmental factors, control interface, physical dimensions, mounting and price. Commonly used position sensors are the optical and magnetic encoders. While laser interferometry can yield a finer resolution in position measurements, it is costly and more suited to calibration and quality control purposes than providing real-time measurement in motion systems. The optical encoder can produce more pulses per cycle than the magnetic encoder, which effectively leads to a higher measurement resolution. To date, the scale grating on linear optical encoders can reach less than four micrometer in pitch. However, there are rela-

tive strengths associated with the magnetic encoder. It is less sensitive to vibration and impact, and more robust to the presence of environmental contaminants such as dirt, oil or water which may lead to a failure in the optical encoder. Comparing cost, generally the cost of a magnetic encoder is also lower than the optical encoder. Thus, between them, the optical encoder is not necessarily a clear choice for the superior resolution it offers when there are other important factors to satisfy in an application. The magnetic encoder can outperform with respect to some of these requirements. Therein this specific example, lies the potential of the use of multiple different sensors for the same measurement, each suited to a certain set of operational factors possibly and collectively arising in the same application.

There is inevitably a limit to the overall performance achievable with a single sensor. Multiple sensors can be used and fused when multiple facets of performance measures are necessary in an application, unattainable with one alone. As an example, a digital encoder can be used to yield position measurements with satisfactory accuracy over a good range of the control motion, but a higher accuracy is needed near the target position. Replacing it by an alternate sensor like the laser interferometer to give fine measurements throughout can be an unnecessarily costly alternative, the laser optics may not be easily mounted on the system for the specific application, and the operational environment may even rule it out as a feasible choice. Such limitations can be managed by using a different position sensor(s) in parallel which is able to fill the gaps beyond the reach of the other sensor. An additional position sensor such as an analog encoder which

can be invoked around the settling point to yield or interpolate into finer resolution measurements [75]- [79]. However, over the range when precision is not critical, the digital encoder may be used instead to raise the maximum operation speed and reduce data handling overheads. Other applications may include an appropriate synergy of position sensors to achieve dynamic balance in response speed and resolution, bandwidth and accuracy, cost and performance, robustness and sensitivity, or other combination of these attributes.

Such an approach has been used in certain domains. In location tracking systems, fusion of signals from global positioning systems and inertia navigation systems is commonly done [80]. Other domains of applications include reverse engineering in coordinate measuring machines [84]- [87], robotics control [82] [83], surveillance system [88], lumber grading [89], mill grinding process [90] and chemical odour mappings [91]. Sensor fusion can also be used to avoid sensor degradation or failure situation to increase the reliability [92]. In precision control, such applications are relatively scarce. Forbes [93] used multiple laser trackers to improve the measurement accuracy deteriorated by the random effects in the refractive index of air along the light path [94] using single laser tracker. He used a general Bayesian approach and the weightages of data were determined by noise parameters, but only applicable to large scale metrology systems. Sebastian et al [95] used a thermal position sensor (TPS) and medium-derived position error signal (PES) to compute the position information as TPS can measure position over an entire travel range but it inherits noise and drift at low frequencies. PES offers excellent DC

fidelity over a limited measurement range but an insufficient solution for the full range. The selection process is controlled by the frequency. Mahmood et al [96] also designed a frequency selective two-sensor controller of a nano-positioner in a discrete manner; using the capacitive sensor signal at low frequencies and the strain displacement signal at high frequencies. The use of multiple sensors is more commonly encountered in the process control industry (albeit for other types of process measurements) under the name of selective control, when variants such as auctioneering or median selector control can select the maximum, minimum or the median value of the multiple sensing measurements for control to satisfy the current control objective.

Current sensor fusion techniques are broadly based on applying the central limit theorem or a Kalman filter to obtain a combined measurement from individual ones, weighted by the quality of the measurements, commonly in the form of noise variances [81]. In order to support an expanded applications of such fusion techniques, a more general framework to enable a practically amenable fusion of sensors with weights that can be selectively adapted to one or more general performance qualities is fundamentally important and useful. The first objective of this chapter is thus to present a framework for combining measurements from different sensors in a practically efficient manner. The weight attached to each measurement is not fixed but they are allowed to evolve to selector attributes chosen to bring out the relative strengths of each measurement. In the chapter, the approach is more specifically elaborated with respect to precision motion control where the application of sensor fusion is less commonly encountered. A

case study is employed in the development which involves the control of a linear motor using a digital magnetic encoder and an analog circuit providing incremental position measurements from velocity measured by an analog sensor. An updated position signal is derived given the positions from the magnetic encoder and the velocity sensor, with different weightages on these measurements. The weightages applied are computed from an optimal fitting procedures to match the final position closely (reference provided by a laser interferometer) and they vary with two different selector attributes in the form of velocity and relative noise present in the velocity sensor over the digital encoder. As these weights change in a nonlinear manner to the selectors, the RBF is used to model the weight variation over the range of operations. Once the RBFs are trained, they provide the weights given the current attributes. A comprehensive set of experimental results are provided to illustrate the applicability of the proposed framework and algorithms.

The rest of the chapter is organized as follows: Section 4.1 describes the proposed sensor fusion framework based on multiple position sensors and a set of selector attributes, Section 4.2 describes the selection and training of the RBF networks, Section 4.3 furnishes the experimental work and results and Section 4.4 concludes the chapter.

4.2   Proposed Framework

The main idea of the proposed framework is to facilitate the derivation of a single combined measurement from multiple sensors providing the same type of measurement.
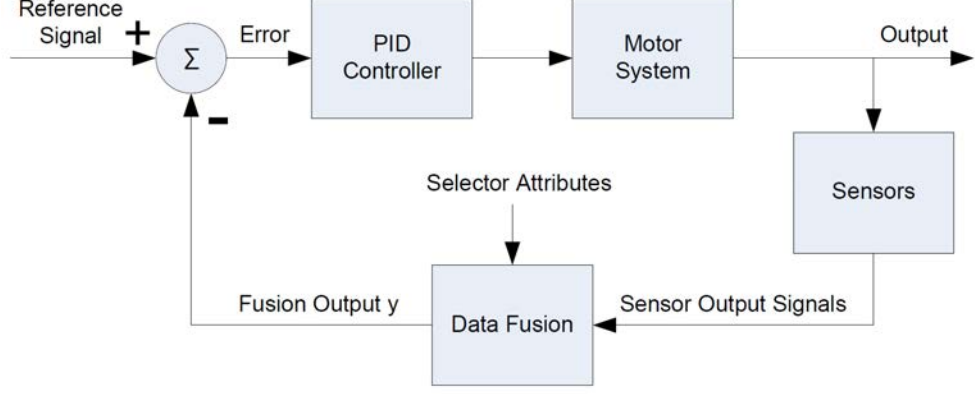
Figure 4.1: Architecture of the proposed data fusion framework

Each sensor can be different in the operational principles and thus individually optimal for a restricted set of scenarios classified under a set of selector attributes. The proposed frame work is shown in Fig. 4.1 and Eq. 4.1. The objective is to achieve a higher quality measurement in some sense of the application, not from any of the individual sensors alone, but an appropriate fusion of the multiple sensors to yield a more optimal fit to the true values in a dynamic manner. While the framework is general, it will be elaborated with respect to position sensing in motion control in this chapter and substantiated similarly with a linear motor setup and experiments.

$$y(s, k) = f(s_1, s_2, ..., s_u) \cdot g(k_1, k_2, ..., k_v) \tag{4.1}$$

where $s_1, s_2, ..., s_u$ are the sensor output signals of the multiple N sensors, $k_1, k_2, ..., k_v$ are the selector attributes of the sensor outputs, and y is the data fusion output.

4.2.1 Position computation using multiple position sensors

Assume N position sensors are used to infer a single position measurement and the fusion function is chosen to be linear with respect to the measurements as shown in Eq.
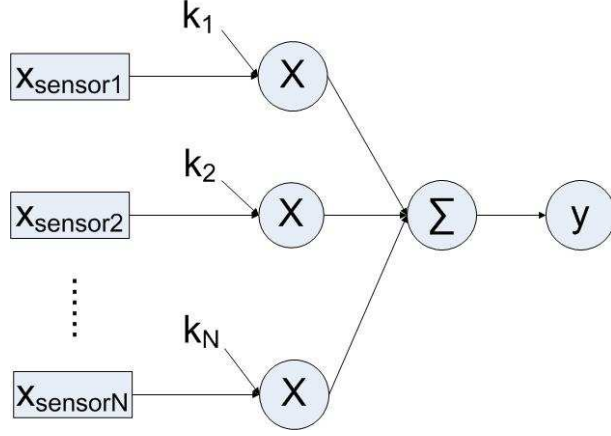
Figure 4.2: Position computation using multiple position sensors

4.2 and Fig. 4.2:

$$x_{pos}(k, x) = \sum_{i=1}^{N} k_i \cdot x_{sensor_i}$$

$$= k_1 \cdot x_{sensor_1} + k_2 \cdot x_{sensor_2} + ... + k_N \cdot x_{sensor_N} \tag{4.2}$$

where k_1, k_2,..., k_N are parameters weighing the influence of each of the measurement on the final value, and x_{sensor_1}, x_{sensor_2},..., x_{sensor_N} represent the measurements from the N different sensors.

We would like to compute the weights so that the target combined value approaches the true value. It should be pointed out that the optimal weights are not fixed but vary with different scenarios which distinguish the strengths of each of the sensor. We refer to the attributes classifying these scenarios as the selector attributes. The true value is unknown in practice but it may be taken to be the value of a close calibration from a gold standard calibration sensor.

4.2.2   Selection weightage computation

For a fixed set of selector attributes, a laser interferometer is used to yield the reference of the true position x_{laser} and the parameters k_1, k_2,..., k_N are to be tuned to fit the fused position x_{pos} to be as close as possible to the reference x_{laser}. Since the function is linear with respect to the parameters, they can be obtained efficiently in a non-iterative manner using least squares estimation algorithms.

However, this single set of weights computed is optimal in the least squares sense with respect to the set of selector attributes. This is fine and sufficient if these attributes are not expected to change during the course of the operations expected of the motion system. When they do change, the weights may not be optimal anymore. To this end, a way to efficiently model and compute the parameters over a range of selector attributes will be necessary. Such selectors may include the frequency of the trajectory, the amount or variance of the noise present relatively among the sensors, the velocity or acceleration of the motion, or the positional zones in the working area. The selectors are necessary to bring out the strengths of individual sensors. For example, different sensors have different characteristics such as response time, bandwidth, resolution, robustness to environmental factors, physical size and cost. A higher weight should be assigned to the specific sensor once the operation enters a domain where it offers relatively higher performance above the others.

In this chapter, we consider two selector attributes in the motion velocity and noise level n_{noise} in each sensor. For a controlled variation in each of these attributes, the

optimal values of k_1, k_2,..., k_N are computed to correspond to the least square estimation between the computed x_{pos} and the measured x_{laser}. For the linear data fusion function used in Eq. 4.2, the equation can be re-written as the following matric-vector form:

$$x_{pos} = S \cdot K = \begin{bmatrix} x_{sensor_1}(t_1) & ... & x_{sensor_N}(t_1) \\ x_{sensor_1}(t_2) & ... & x_{sensor_N}(t_2) \\ ... & ... & ... \\ x_{sensor_1}(t_M) & ... & x_{sensor_N}(t_M) \end{bmatrix} \cdot \begin{bmatrix} k_1 \\ k_2 \\ ... \\ k_N \end{bmatrix} \tag{4.3}$$

where the entries of S are given by $x_{sensor_i}(t_j)$ which is the output of the $sensor_i$ at time t_j ($i = 1, 2, ..., N; j = 1, 2, ..., M$), the entries of K are given by k_i, and the entries of x_{pos} are given by $x_{pos}(t_j)$ at time t_j.

To find the values of K using the least square estimation between x_{pos} and x_{laser}, let Eq. 4.3 equals to x_{laser}:

$$S \cdot K = x_{laser} \tag{4.4}$$

where the entries of x_{laser} are given by $x_{laser}(t_j)$ at time t_j.

Assuming $S^T S$ is non-singular, the least squares optimal solution of K is given by Eq. 4.4:

$$K = (S^T S)^{-1} S^T x_{laser} \tag{4.5}$$

where the entries of x_{laser} are given by $x_{laser}(t_j)$ at time t_j.

A recursive LS algorithm can be used to refine the weights with each incremental data set obtained, so that estimation can begin after the first data set and each subsequent incoming data set will improve the accuracy of the estimates. With this algorithm, the optimal values of the weightings k_1, k_2,..., k_N for each set of selector attributes can be

71

obtained to yield a position output closest to the true value under the condition reflected by the selector attributes. To this end, systematic errors such as certain geometrical errors are also compensated in the process. RBF networks, which would be introduced in the next section, are then trained to model those weights over the variation of the attributes.

4.2.3 Parameter weightage modeling using RBF approximation

In the approach proposed above, each computed parameter weightage K varies with motion velocity and noise level n_{noise} in a nonlinear manner. To estimate those weightages, neural networks like RBF method can be used [50]. It has been shown that under mild assumptions, RBF is suitable for universal approximations, i.e., any continuous function can be approximated over a compact set to any degree of accuracy. So, in this chapter, RBF is employed for the modeling of the weights variation with respect to the selector attributes.

In the case study considered in this chapter to be further highlighted in Section 4.3, the two selector attributes in terms of the velocity $velo$ and noise level n_{noise} in the velocity sensor are considered as the input x. The selection weightage K computed using least squares estimation is used as the target y. Thus, this specific RBF network has 2-DOF since its characteristics depend on both motion velocity $velo$ and noise level n_{noise}. Based on Eq. 2.11, this RBF network can be re-written as:

$$K = \sum_{i=1}^{M} w_i \varphi_i(|||[velo, n_{noise}] - [\mu_{velo_i}, \mu_{n_{noise\,i}}]|||) + w_0 \qquad (4.6)$$

72

The RBF weights w can be obtained by replacing x and μ with $[velo, n_{noise}]$ and $[\mu_{velo}, \mu_{n_{noise}}]$ accordingly in Eq. 2.13 and Eq. 2.14. The trained RBF function can be used to model the variation of the weightages K with the selector attributes and subsequently used to construct the data fusion function accordingly using Eq. 4.3.

4.3 Case Study

A single axis setup (Akribis DC linear motor) is used as the basis for a case study. The slide attached on the stage can move bi-directionally along the X axis, with a working range of 200 mm. A magnetic encoder with a resolution of 2 mm is used to obtain the position signal x_{enc}. An analog velocity sensor is also mounted to give analog velocity measurements as well as positional information when the velocity is fed into a digital integrator. Thus, in this case study, we have two different sources of position measurement; one from the magnetic encoder and the other from the velocity sensor integrated to yield the position. Being an analog sensor, the resolution of the velocity sensor is infinitesimal. Thus, when digital integration is done accurately over the lower velocity range, the latter position measurement can offer a better accuracy than the magnetic encoder. However, as velocity picks up relative to the sensitivity of the sensor, the accuracy of the velocity measurement degrades leading to accuracy loss in the position measurements too after the digital integration. Thus, the relative performance of each of the sensor varies with velocity and velocity is selected as the first selector attribute in this case study. The relative amount of noise present from the two
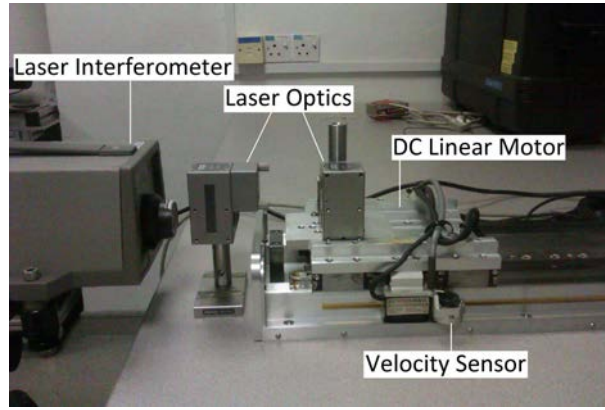
Figure 4.3: System setup 1
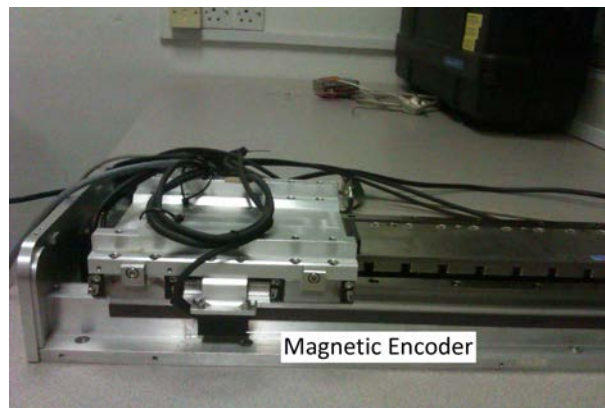
Figure 4.4: System setup 2

sources should also govern the priority to be attached to each of the two measurements to infer the final position measurement. The magnetic encoder is a digital sensor. Thus, the second selector attribute is chosen to be the amount of noise present in the velocity measurements.

A laser interferometer is used to provide the "true" position measurement x_{laser}. The system setup is shown in Fig. 4.3 and Fig. 4.4. The system flowcharts are shown in Fig. 4.5 and Fig. 4.6.
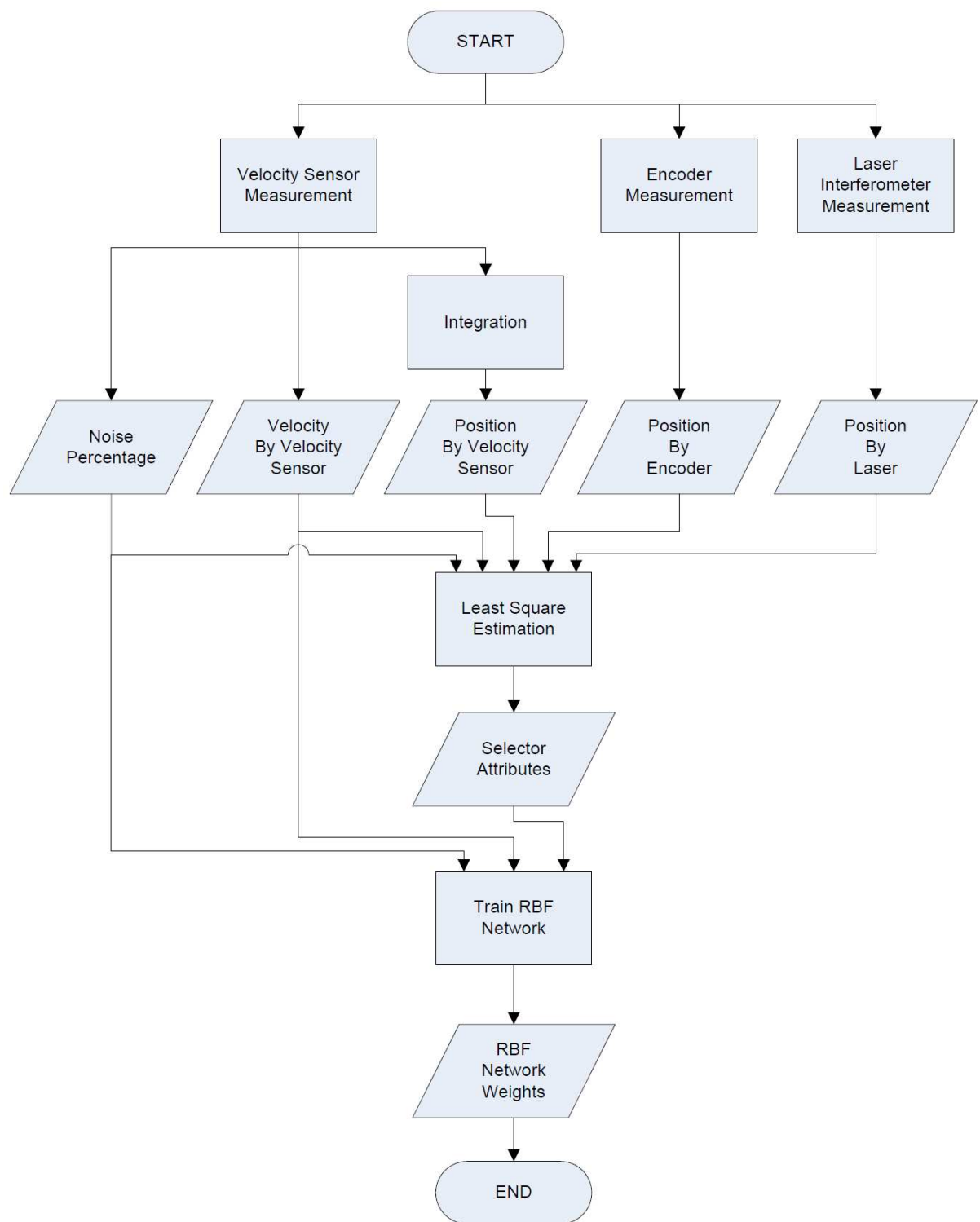
Figure 4.5: RBF network training

75
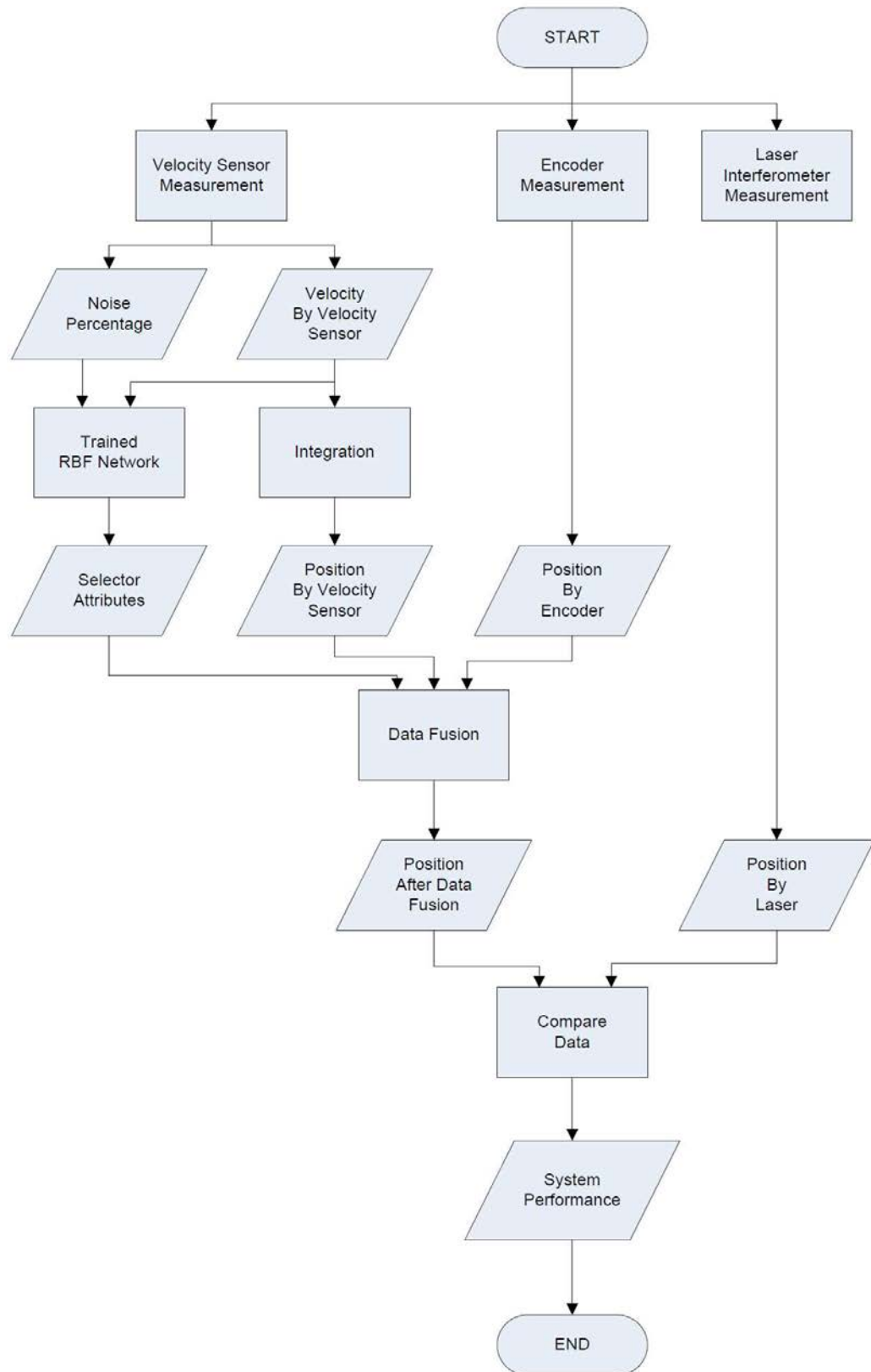
Figure 4.6: System flowchart

76

4.3.1 Data collection phase

The motor is controlled to run at constant velocity mode with 200 mm total movement length. The noise level associated with the velocity sensor used can be maintained at 5% in ideal and static laboratory conditions. However, it can vary with the presence and interaction with EM sources, power interference or operating conditions. To enable the results to remain applicable at other times and operating conditions of the motor, the noise level as a selector attribute is allowed to vary during the data collection phase by injecting or amplifying the noise to different levels. The raw data and true data are collected with different velocities from 0.02 m/s to 0.6 m/s and different noise levels in the velocity sensor from 5% to 1000% of the maximum reading for each velocity. At a specific movement velocity and a specific noise level in the velocity sensor, the velocity sensor output $v_{vsensor}$, the magnetic encoder output x_{enc} and the true data x_{laser} are continuously collected during the motor movement, and the velocity sensor measured position signal $x_{vsensor}$ is obtained separately after the integration of $v_{vsensor}$.

4.3.2 Parameter estimation

Using the linear in the parameter form, the combined position can be expressed in the following form:

$$x_{pos} = k_1 \cdot x_{vsensor} + k_2 \cdot x_{enc} \tag{4.7}$$

The reference position x_{laser} obtained by the laser interferometer is used as the reference position x_{laser} for the purpose of estimating the parameters k_1 and k_2. For each

77

Table 4.1: k_1 Values Selection for Different Velocities and Noise Levels

Noise	Velocities (m/s)						
	0.04	0.10	0.20	0.30	0.40	0.50	0.60
5%	0.87	0.875	0.61	0.46	0.25	0.29	0.00
10%	0.87	0.885	0.62	0.47	0.255	0.29	0.00
50%	0.89	0.98	0.585	0.405	0.30	0.265	0.00
100%	0.915	1.00	0.665	0.48	0.185	0.31	0.00
300%	0.825	1.00	0.48	0.285	0.025	0.105	0.00
500%	0.375	0.38	0.205	0.01	0.005	0.055	0.00
1000%	0.035	0.04	0.02	0.01	0.005	0.00	0.00

set of selector attributes, the optimal weight parameters can thus be estimated with the algorithm as presented in previous section. Thus, with the full data set collected earlier, two tables (Table 4.1 and 4.2) can be obtained, tabulating the optimal weights against the velocity selector $v_{vsensor}$ and the noise selector n_{noise}. From those two tables, it can be seen that at low noise situations, the value of k_1 (the weightage of the velocity sensor) is much larger than the value of k_2 (the weightage of the encoder) at low velocity range, and much smaller at high velocity range. Thus in this motor, the position measured using velocity sensor is better than that using encoder in the low velocity range, and vice versa. This means it is possible that the position measured using velocity sensor can be better than encoder under specific situations. This is precisely why a selective approach is developed.

4.3.3 RBF modeling of weights variation

In this specific case, a 2-dimensional RBF networks is trained and applied to approximate the values of the weight parameters k_1 and k_2 as shown in Fig. 4.7 based on two selector

Table 4.2: k_2 Values Selection for Different Velocities and Noise Levels

Noise	Velocities (m/s)						
	0.04	0.10	0.20	0.30	0.40	0.50	0.60
5%	0.135	0.13	0.39	0.54	0.75	0.705	0.995
10%	0.135	0.12	0.38	0.53	0.745	0.705	0.995
50%	0.115	0.025	0.42	0.6	0.7	0.73	0.995
100%	0.09	0.01	0.34	0.525	0.82	0.69	0.995
300%	0.185	0.035	0.54	0.73	0.98	0.895	0.995
500%	0.65	0.665	0.82	1.00	1.00	0.945	0.995
1000%	1.00	1.00	1.00	1.00	1.00	0.995	0.995
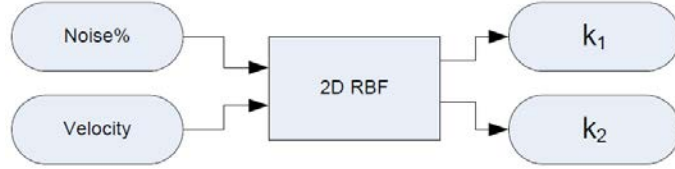
Figure 4.7: Flowchart of 2D RBF network

inputs: $v_{vsensor}$ and n_{noise} as follows:

$$k_1 = f_{k_1}(v_{vsensor}, n_{noise}) \tag{4.8}$$

$$k_2 = f_{k_2}(v_{vsensor}, n_{noise}) \tag{4.9}$$

So the fused position signal can be represented as in Eq. 4.10, and this position signal x_{pos} can either be used directly by the controller, or be interpolated to a higher order to improve the system resolution.

$$x_{pos} = f_{k_1}(v_{vsensor}, n_{noise}) \cdot x_{vsensor} + f_{k_2}(v_{vsensor}, n_{noise}) \cdot x_{enc} \tag{4.10}$$

The approximated functions $f_{k_1}(v_{vsensor}, n_{noise})$ of k_1 and $f_{k_2}(v_{vsensor}, n_{noise})$ of k_2 are determined and plotted in Fig. 4.8 and Fig. 4.9, under different velocities and noise levels. Only six lines are shown in each figure with six noise levels from 5% to 500% corre-spondingly. A nonlinear relationship can be observed between k_1/k_2 values and selectors:
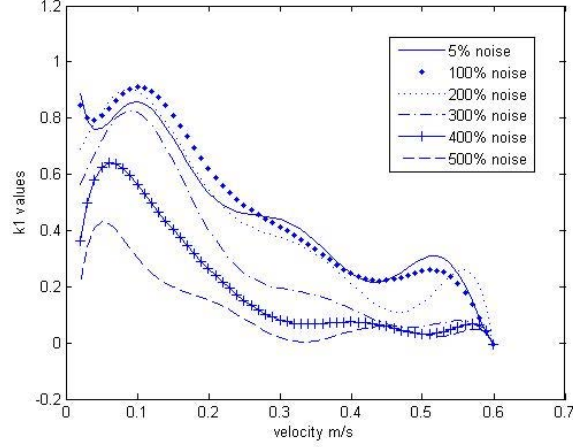
Figure 4.8: RBF approximation of k_1

velocity and noise levels. k_1 decreases significantly with higher noise levels under same velocity value. This is consistent with physical intuition as a higher content of noise will shift weightage away from the analog sensor. k_1 also decreases significantly with higher velocity under same noise level. At lower velocities, the position measurements from the digitally integrated velocity signal yield good accuracy but the accuracy is degraded at higher velocities due to the sensitivity characteristics of the sensor. The complementary relationships are observed in k_2. In order to show the relationship between k_1/k_2 values and velocities/noise levels, a two-dimensional RBF is used to approximate the functions of k_1 and k_2, which are depicted in Fig. 4.10 and Fig. 4.11.

4.3.4 Control experiments

To observe the improvement on the overall precision with the proposed framework and approach, control experiments on the testbed are done. Three sinusoidal reference signals with the amplitude of 100mm and the periods of 3/4/5 seconds are applied to the linear

Figure 4.9: RBF approximation of k_2

Figure 4.10: 2-dimensional RBF approximation of k_1
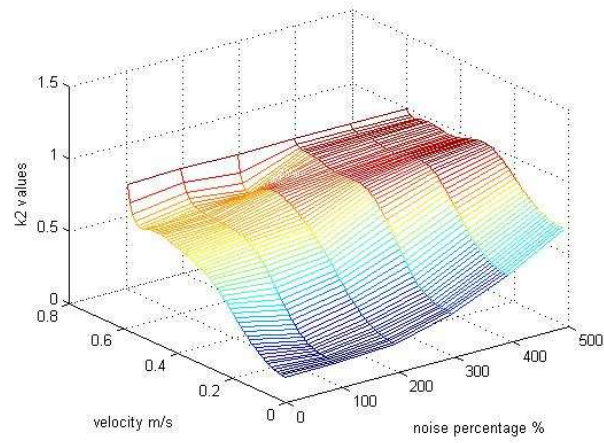
Figure 4.11: 2-dimensional RBF approximation of k_2

81

motor separately. The periods of the sinusoidal reference signals are specially chosen to include all the measured velocities of the linear machine. A PID controller is used to control the linear motor. The analog velocity sensor is used to measure the velocity signal $v_{vsensor}$, the magnetic encoder is used to measure the position sign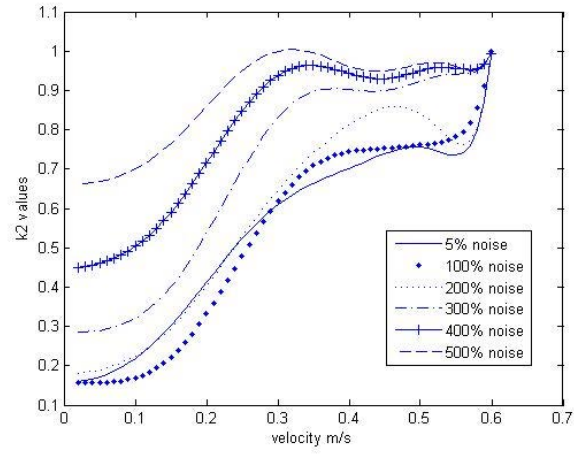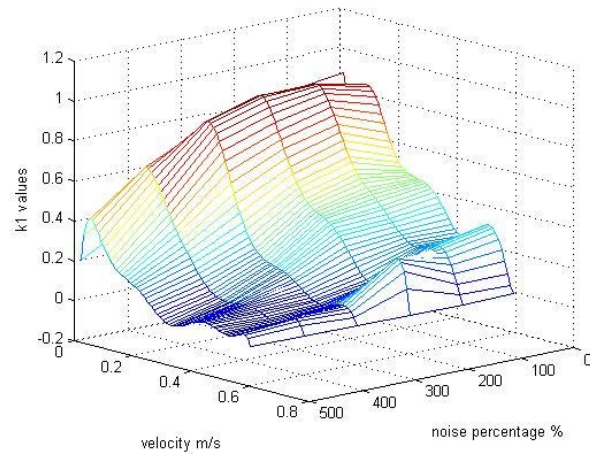al x_{enc} and the laser interferometer is used to measure the reference position x_{laser}. Those collected signals can be used to train the 2D RBF networks, and the estimated position x_{pos} can be obtained using Eq. 4.10.

As originally the magnetic encoder is installed in the motor stage, the system error in the estimated position from data fusion is compared with the error in the magnetic encoder, to observe the difference in the system performance before and after installing the velocity sensor in the stage. The positioning and tracking performances of the proposed method for the three reference sinusoidal signals are shown in Fig. 4.12 to Fig. 4.14. To observe the error tolerance of the proposed approach, the system tracking performance at different noise levels are plotted from Fig. 4.15 to Fig. 4.20, for reference signals with period of 5 seconds and error percentages of 5%, 10%, 20%, 30%, 40% and 50%. It can be observed that the system performance can be improved if the noise level is kept below 30%.

As can be clearly observed in the experimental study, the proposed method can improve the tracking performance and system precision. Due to the nonlinear characteristics of k_1 and k_2 and a large data set requirement (as shown in Fig. 4.8 and Fig. 4.9), RBF networks are preferred as they require less data points compared with look-up ta-
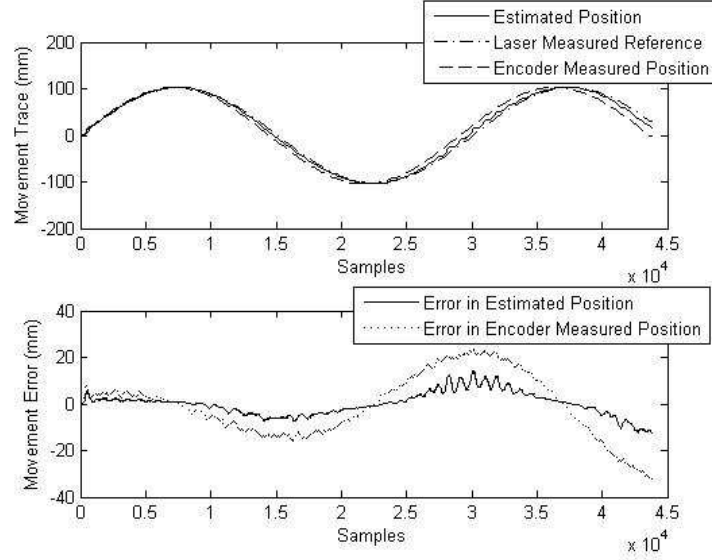
Figure 4.12: Tracking performance with sinusoidal reference input signal (amp=100mm period=3s)

ble method under the same accuracy requirement. The usage of RBF can reduce the memory requirement and improve the control execution speed.

4.4 Conclusion

A framework to fuse measurements from different sensors in a practically amenable manner is presented in the chapter. The weight attached to each measurement is not fixed but they evolve with selector attributes to yield an improved combined measurement based on the situation as demarcated by the attributes. Algorithms to determine the weights from measurements and model their nonlinear variation with the selector attributes have been developed. A selective control approach towards precision motion systems based on this framework is then developed and demonstrated with a case study on a linear motor with two position measurements forthcoming from two different sensors. Improved performance is observed compared to when only a single sensor is used.
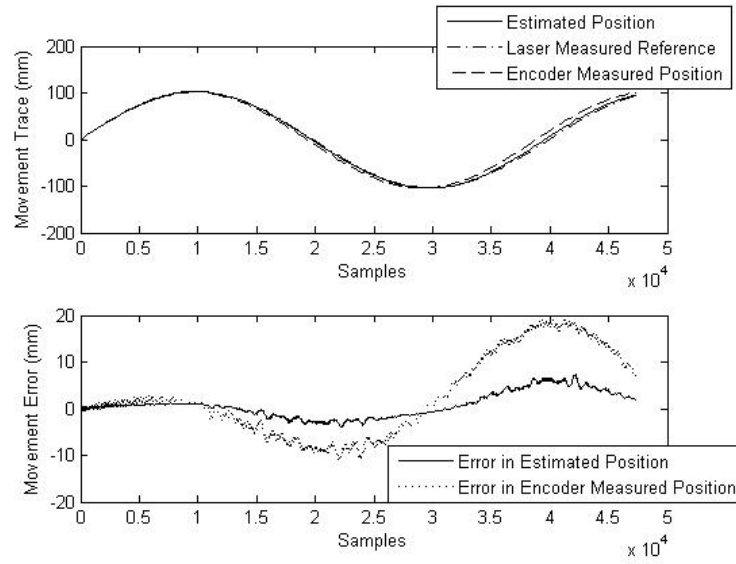
Figure 4.13: Tracking performance with sinusoidal reference input signal (amp=100mm period=4s)
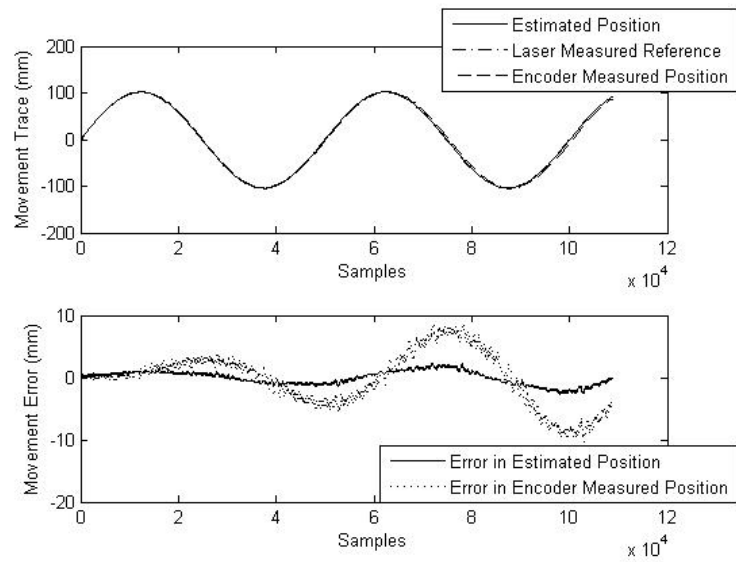
Figure 4.14: Tracking performance with sinusoidal reference input signal (amp=100mm period=5s)
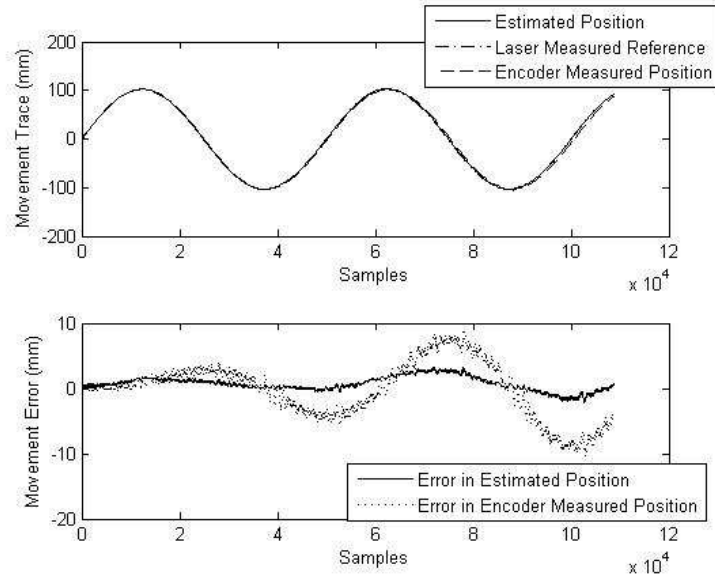
Figure 4.15: Tracking performance with 5% velocity sensor error and sinusoidal reference input signal (amp=100mm period=5s)
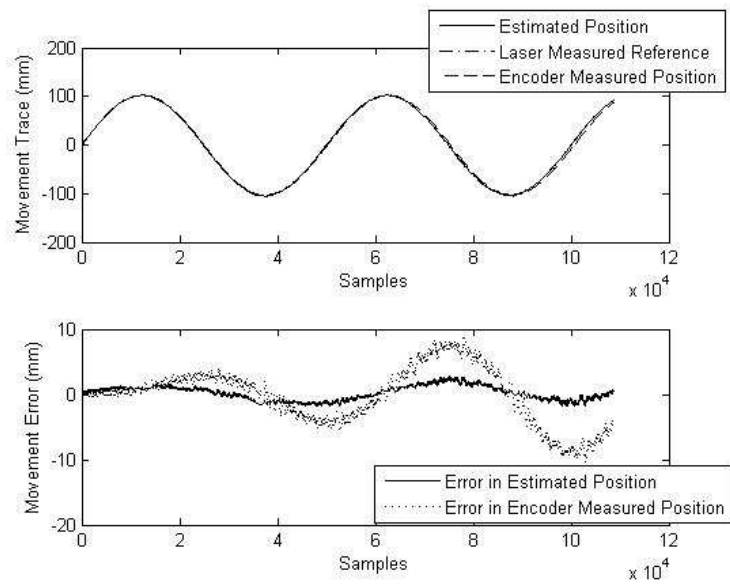
Figure 4.16: Tracking performance with 10% velocity sensor error and sinusoidal reference input signal (amp=100mm period=5s)
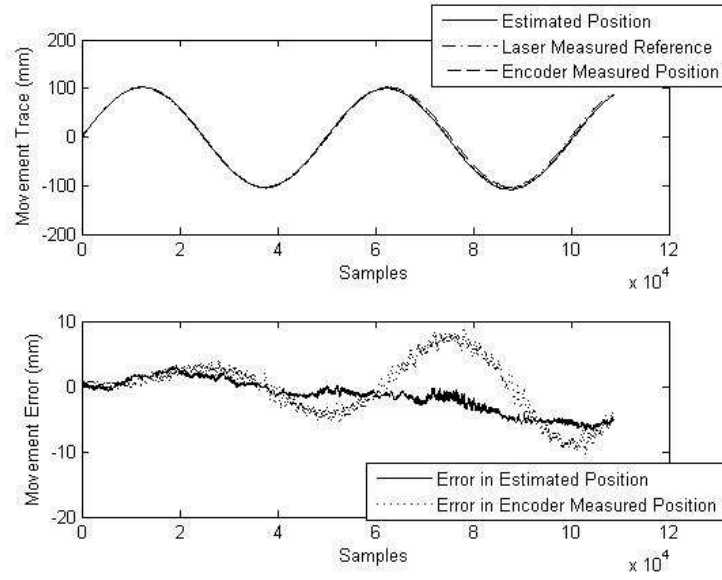
Figure 4.17: Tracking performance with 20% velocity sensor error and sinusoidal reference input signal (amp=100mm period=5s)
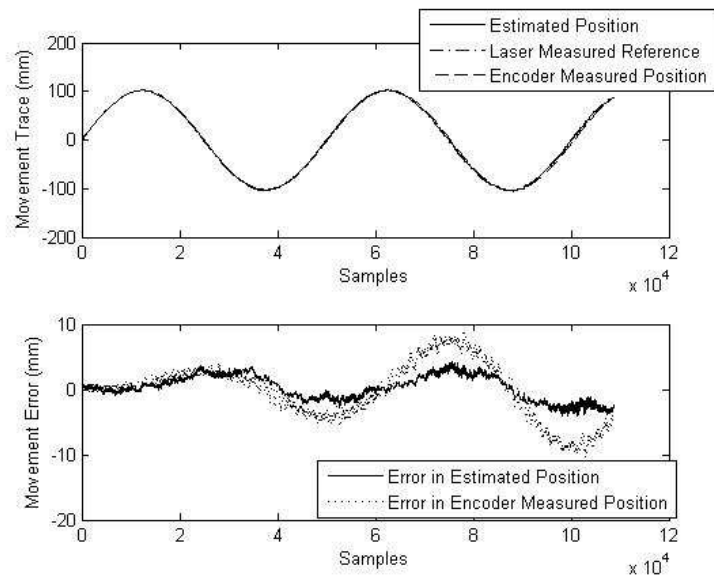
Figure 4.18: Tracking performance with 30% velocity sensor error and sinusoidal reference input signal (amp=100mm period=5s)
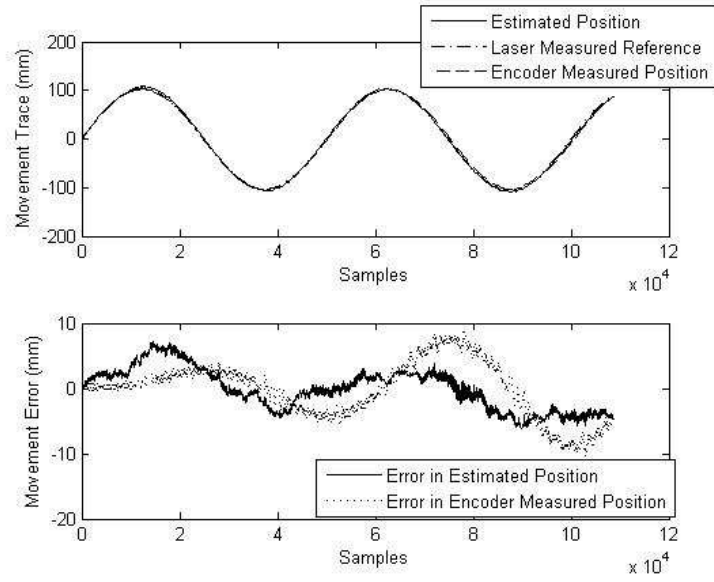
Figure 4.19: Tracking performance with 40% velocity sensor error and sinusoidal reference input signal (amp=100mm period=5s)
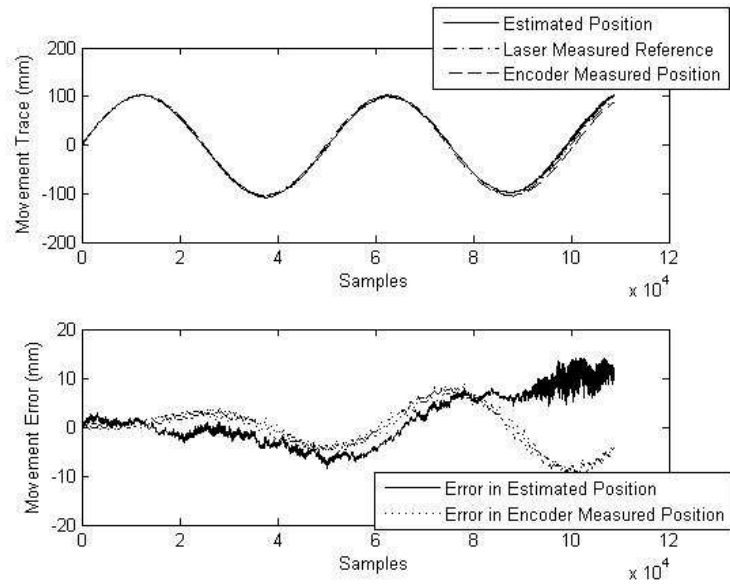
Figure 4.20: Tracking performance with 50% velocity sensor error and sinusoidal reference input signal (amp=100mm period=5s)

Chapter 3 can also be considered as a special case of this chapter. In Chapter 3, two sensors (displacement and thermal) are used together to obtain the displacement error and the overall performance is also improved compared with the performance using one displacement sensor only.

Chapter 5

Development of Drop-On-Demand Micro-Dispensing System

5.1 Introduction

Bio-chip microarray technology is becoming an important platform for biomedical solutions. The most popular bio-chip microarrays are DNA and protein microarray, and the key issue is microarray fabrication [104]. The methods for microarray fabrication can be classified into two categories: contact printing and non-contact inkjet printing [106]. Contact printing is the first approach for microarray fabrication and involves loading a printing pin with the solution at the loading station, tapping it to the substrate and cleaning at the washing station. The operation speed is relatively low as limited by the loading and cleaning procedure, and the shape of the spots may not be uniform due to the surface tension, adhesive force and capillary action [106]. Due to the speed constrain and non-uniformity of the spots of contact printing method, non-contact inkjet printing method is adopted and a micro-droplet dispensing system is designed: solutions are ejected from the dispensing head onto the substrate from a certain distance and no

loading or washing stations are needed [106]. Thus the procedure of the micro-droplet dispensing system is much faster compared with that of contact printing.

A micro-droplet dispensing system with multiple dispensing heads has many engineering applications, including micro fabrication, DNA micro-arraying, manufacture of bio-sensor strips, micro-patterning on printed circuit board, rapid prototyping, etc. Due to the requirements from different micro-fabrication applications, researchers usually developed their own micro DOD systems [97] [107]- [110]. These systems basically consist of two components: the multiple dispensing heads with their associated drivers and the XYZ precision stage to move the dispensing heads and substrate onto the desired position. In our DOD micro-dispensing system in this chapter, two solenoid actuating micro-valve dispensers are used. Micro-valve nozzle is widely used in micro-dispensing applications. To build tissue scaffold, Khalil et al. [100] and Lee et al. [101] proposed the multi-material deposition system with different types of nozzles, among which micro-valve was applied. However, their reports focused on the functional description of components and system. Kwang and Ahn [102] gave a brief overview of micro-valves, based on the actuation mechanisms and their applications. He believed that reliability was the key for successful miniaturization and commercialization of fully integrated microfluidic systems, and there was plenty of room for further improvement in the performance of existing micro-valves. Li et al. [103] characterized the performance of micro-valve in DOD system with regards to operational time, pressure, and viscosity of dispensing material. The influence of dispensing heads own operational parameters on printing performance

has been extensively reported [98] [99].

However, the factors which can determine the final placement accuracy of the printed pattern, such as the placement of the dispensing head, the accuracy of the droplet trajectory, the positioning accuracy of the stage system, environmental noises like wind, vibrations and time related disturbances, are not fully addressed yet [105]. In the micro-droplet dispensing method, the dispensing head is well controlled in a repeatable manner to eject individual drops of material such that the final size and position of the dot on the substrate is predictable. The above factors can obviously affect the micro-fabrication accuracy, thus it is very necessary to discuss their influence in the position accuracy of the micro-dispensing process and apply compensations accordingly.

In the experiments, the system printing performance on the substrate is investigated using statistical methods. The droplets from the dispensing head are printed and their results on the substrates are examined in detail to obtain the print pattern. The error compensation technique is applied to improve the accuracy of the droplets. In the chapter, the experimental setup is introduced in Section 5.2, followed by the discussion of factors related to printing accuracy in Section 5.3. Droplet distribution analysis of the dispensing head is given in Section 5.4, and error compensations on the motor stage and printed droplets are shown in Section 5.5 and Section 5.6. A conclusion is given in Section 5.7.
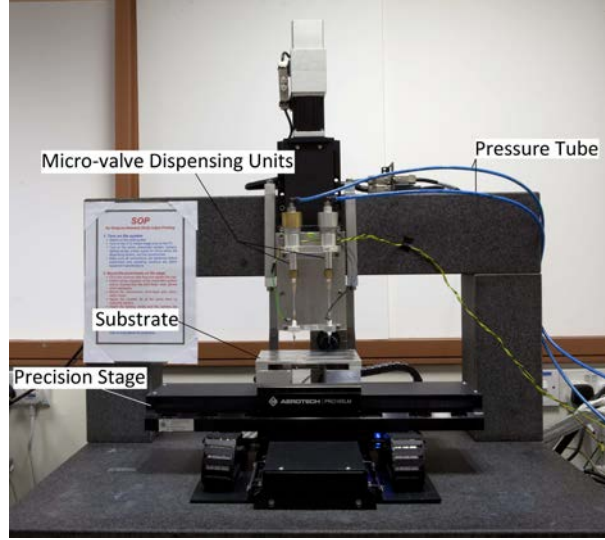
Figure 5.1: Micro-dispensing DOD system

5.2 Experimental Set-up of Micro-dispensing DOD System

5.2.1 Introduction to micro-dispensing DOD system

Fig. 5.1 shows the micro-dispensing DOD system used in the experiment, including XYZ precision stage and two dispensing units. The position speed for the X and Y stage ranges from 1 to 250 mm/s with a positioning accuracy of $5\mu m$ and $1\mu m$ respectively. The two dispensing units are attached on the Z axis with a mounting structure. The substrate plate is mounted on the slide which rides on the XY plane so it is able to move along both Y and Z axis directions. The stage positions are recorded by encoders attached on XYZ axes. When the stage reaches the target position, the stage will produce a set of TTL trigger signals to activate the dispensing driver and the corresponding dispensing head for drop ejection.

5.2.2 Micro-valve dispensing system

In this section, the micro dispensing units are introduced. Each dispensing head is connected to $50ml$ reservoir with a $7\mu m$ filter to prevent nozzle clog. The trigger signal from the stage driver, i.e. standard TTL signal, is used as the input of the dispensing head drivers. The corresponding driver subsequently magnifies this signal to the appropriate voltage levels for dispensing head operation.

The solenoid actuated micro-valve dispensing system consists of a micro-valve, a micro-valve driver and a pneumatic controller. The micro-valve shown in Fig. 5.2 is from Lee Company (VHS Starter Kit P/N IKTX0322000A) equipped with 3 nozzles with diameter of 127, 190.5 and 254 μm respectively. Fig. 5.3a shows a schematic diagram of the solenoid micro-valve with a cross-sectional image. The micro-valve operates through a solenoid system to open or close the valve. A magnetic field is induced which forces the piston to open the valve as indicted by the arrow. Likewise, the spring forces the piston onto the valve seat to close the valve. Fig. 5.3b shows the triggering signal of micro-valve driver. Under external trigger signal between 60 Hz and 1 kHz, the valve driver outputs 24 V spike voltage to activate the valve and 3 V to hold the open status. The total time period including spike and hold status is defined as operational on time (OOT).

Figure 5.2: Micro-vale from Lee company
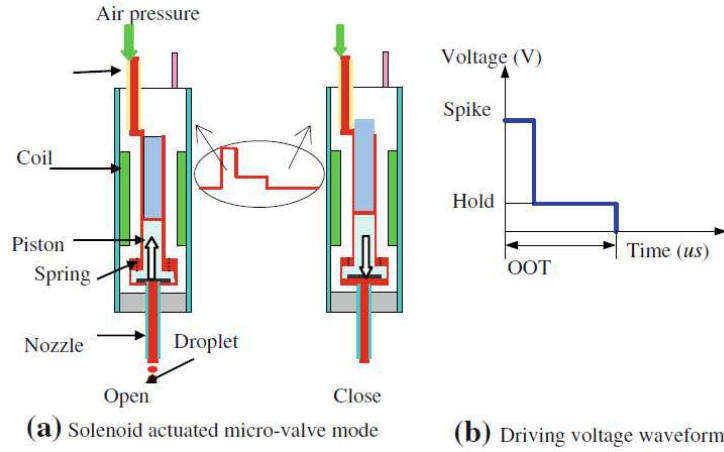
Figure 5.3: Schematic diagram of the solenoid micro-valve

5.2.3 Pneumatic controller

The pneumatic controller used in this DOD system is shown in Fig. 5.4. It has two outlets for a stable positive pressure and purge pressure to expel the liquid accumulated at the nozzle tip. When the valve is open, the stable positive pressure pushes the liquid along the chamber towards the nozzle. With the proper pressure and OOT, the liquid can form a droplet at the nozzle tip.

5.3 Factors Related to Printing Accuracy

Besides own parameters of the dispensing heads, factors which can determine the final placement accuracy of the printed pattern are the positioning accuracy of the precision

94

Figure 5.4: Pneumatic controller

stage, the placement of the dispensing head, time related disturbances and environmental

noises like wind or vibrations.

5.3.1 Stage related parameters

The precision XYZ stages provide 3D printing capability by positioning the dispensing

heads and substrate under the predefined position. Inaccuracies in the precision stage

movement also lead to possible errors in geometry or accumulations of droplet in one

region. Error compensation can be applied to improve the stage accuracy.

5.3.2 Dispensing head placement

As the dispensing head is fastened using screws on the mounted structure of Z axis,

the placement of the dispensing head may not be properly aligned with Z axis. Both

displacement and angular differences may exist. The ejected droplets may be off the

target due to those differences. Error compensation can also be applied to adjust the

droplet positions on the substrate.

5.3.3 Environmental noises

The printing performance of the micro-dispensing system is fairly sensitive to vibrations in the fluid supply line and reservoir. The ejected droplets are also sensitive to the wind in the environment. Both may cause erratic droplet dispensing in the system. As the environmental noises are not repeatable and the unstable circumstances are not fully understood, the best way is minimize those environmental noises. An isolation cage can be applied to the stage to avoid the effect of wind, and lower printing speed and improvement of dispensing heads' fixture design with isolated and stationary connection between dispensing head and reservoir can help reduce the vibration.

5.3.4 Time related disturbances

The printing time should be controlled to maintain a fabrication process with desired accuracy. With the current observation of two dispensing heads functionality, a consistent, steady droplet stream is less likely to be preserved upon stopping and restarting of dispensing heads for more than one hour. It is also observed that the speed of the droplet tends to decrease with printing time. With the increase of printing time, the change in the reservoir level relative to the dispensing head, gradual magnification of internal disturbances from the dispensing head actuation process, or corrosion of the orifice plate could contribute to this phenomenon. With a progressive decrease in ejection speed over time, the presence of crosswinds can greatly affect proper droplet placement on the substrate. In some cases, cleaning the orifice plate with a compatible solvent introduces

temporary impedance to stable droplet formation. When residual solvent evaporates from the orifice plate surface, lingering solvent may interfere the ejected drops, notably their speed in the air. This phenomenon is clearly illustrated by the observed gradual shift in dispensed droplet position. Thus, sufficient time is required before fabrication experiment so that the solvent can fully evaporate.

5.4   Statistics of Deposited Droplet Size

The diameter of printing droplets is very useful to define proper pitch and speed in fabrication and to test the repeatability of the system. The measurement can be easily determined in ink-based tests by measuring the ink drop size shown on paper using microscope. For observation purpose, operational parameters and printing parameters are selected carefully to ensure no overlapping among adjacent droplets. The dispensing liquid is dispensed over five rows of length at 5cm each. For each dispensing head, about 80 samples are randomly selected from around 1,200 printed droplets on the photo paper from both X and Y directions. Readings of droplet diameter are taken for five times. The droplet characteristic is described using average droplet diameter and standard deviation.

5.4.1   Droplet samples from micro-valve dispensing head

The droplet size samples are collected under two cases: pitch between 0.7 and 1.0 mm (case 1); and speed between 1.8 and 72 mm/s (case 2). Table 5.1 shows droplet size analysis in the two cases, and the dispensing material is distilled water with ink. The

Table 5.1: Droplet Size Analysis in Micro-valve Dispensing Head

	Case 1		Case 2	
	$\overline{x}_{m\_d}$	σ_{m_d}	$\overline{x}_{m\_d}$	σ_{m_d}
Droplet (mm)	0.619	0.008	0.664	0.008
η (%)	Within $\pm\sigma_{m\_d}$	Within $\pm2\sigma_{m\_d}$	Within $\pm\sigma_{m\_d}$	Within $\pm2\sigma_{m\_d}$
	70.2	93.5	70.9	94.2

measured average droplet diameter and its standard deviation are denoted as $\overline{x}_{m\_d}$ and

σ_{m_d} separately. η is the percentage of droplet size located within a specific range.

In case 1, the average droplet size is 0.619 mm with the operational parameters of

$OOT = 180\mu s$ and pressure $P = 9.75psi$. No obvious difference has been found in droplet

size samples collected from the pitch range $[0.7, 1.0]mm$, i.e. varying pitch can not affect

the dispensed droplet size on the substrate. Also, 70.2% of droplet size observation falls

within $\overline{x}_{m\_d} \pm \sigma_{m\_d}$ (one sigma) under varied pitch, and this number reaches to 93.4%

for $\overline{x}_{m\_d} \pm 2\sigma_{m\_d}$ (two sigma).

In case 2, the average droplet size is 0.664 mm with the operational parameters of

$OOT = 200\mu s$ and $P = 10psi$. It is also noted that the dispensed droplet size does not

change with varied speed. In case 2, 70.9% of droplet size observation is located within

one sigma, this number reaches to 94.2% for two sigma, and almost all the data points

lie within three sigma. Fig. 5.5 illustrates the frequency distribution from the two cases,

and droplet size within $\pm\sigma_{m\_d}$ is highlighted.

5.4.2 Droplet size analysis

There are three notable observations. Firstly, it is found that varying pitch and speed

can not change the dispensed droplet size on the substrate. Secondly, the frequency

(a) Frequency distribution under varied pitch [0.7mm, 1.0mm]
(b) Frequency distribution under varied speed [1.8mm/s, 72mm/s]
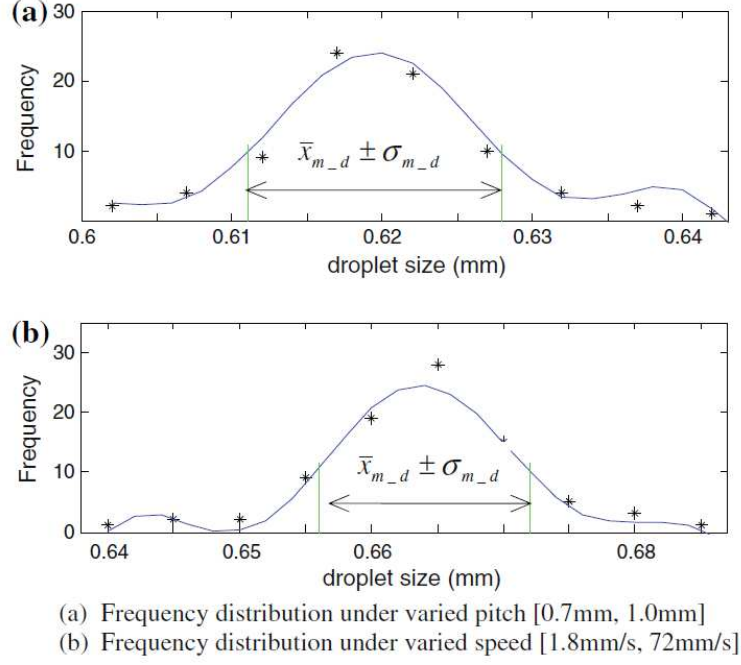
Figure 5.5: Droplet diameter distribution for micro-valve dispensing head

distribution curve is bell-shaped, with a peak for each case. The droplet size from a

specific set of operational parameters tends to cluster around the average droplet size,

and the standard deviation is the width of the bell. Last but not least, the statistical

results of our droplet size samples approximates to normal distribution (68% of the

samples within one sigma, 95% within two sigma, and 99.7% within 3 sigma). These

conclusions provide valuable information for building theoretical models or empirical

equations in 3D micro-fabrication process.

5.5 Error Compensation on Motor Stage

According to previous analysis, there are many factors which may affect the printing

accuracy of the DOD system. But as the time related disturbances are not fully un-

derstood and the environment noises are not repeatable, only the first two factors can

be compensated using proper modeling. As the accuracy of the stage is fixed, it is very difficult and costly to implement hardware modification. So software compensation like geometric error compensation is more feasible. For the motor stage used in the DOD system, the influence from Z axis is not considered due to the less frequent movement in this direction. The geometric error compensation on the motor stage is conducted using the same method as in Chapter 2. The compensation results are shown in section 2.3.1 and the displacement error can be reduced by around 35% from result shown in Fig. 2.17.

5.6 Error Compensation on Printed Droplets

In real experiment, the placement of the dispensing head may not be exactly aligned with the desired position. Thus the final droplet position may be different from the desired position. The error between the desired position and the actual droplet position comprise of two components: systematic error and random error. The systematic error can be determined from the trajectory analysis based on placement of dispensing head, and can be compensated accordingly. The random error may come from system noises and changes in environment condition etc. The random error cannot be compensated but can be minimized by having more data to average out the effects. The detailed flowchart of the error compensation procedure is shown in Fig. 5.6.
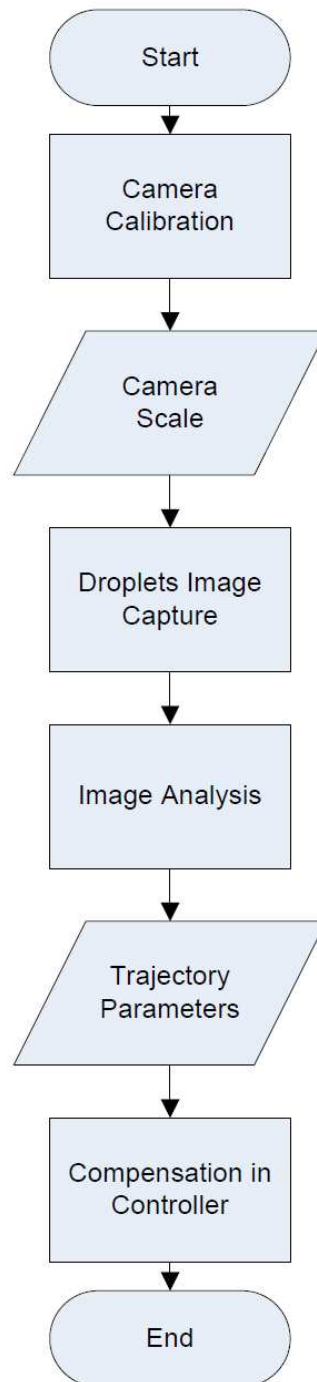
Figure 5.6: Flowchart of droplet error compensation
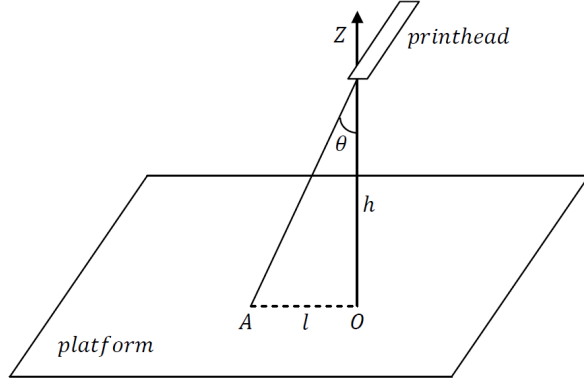
Figure 5.7: Droplet trajectory vertical

5.6.1 Trajectory analysis of the printed droplets

The droplet trajectory from the dispensing head is shown in Fig. 5.7 and Fig. 5.8, where h is the distance from the end position of the dispensing head to the substrate, l is the length of the trace projection OA on XY plane, α is the angle between OA and X and θ is the angle between the dispensing trace and Z axis. Let x_e and y_e be the initial placement errors of dispensing head on X and Y axes, and x_p and y_p are the measured distances between the target position and droplet position on X and Y axes, then the droplet trajectory can be modeled as:

$$\begin{bmatrix} x_p \\ y_p \end{bmatrix} = \begin{bmatrix} 1 & 0 & tan\theta cos\alpha \\ 0 & 1 & tan\theta sin\alpha \end{bmatrix} \begin{bmatrix} x_e \\ y_e \\ h \end{bmatrix} \tag{5.1}$$

The four variables α, θ, x_e and y_e can be estimated with the coordinate measurement of the droplet position. In order to minimize the random error, multiple droplet positions at different heights h of the dispensing head can be measured to average out the effects. Then error compensation on the droplet position can be performed to correct the misplacement of the droplet from the required position.

102
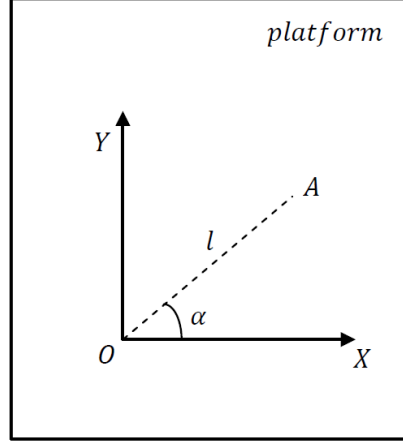
Figure 5.8: Droplet trajectory horizontal

5.6.2 Camera calibration

In order to measure the coordinates of the droplets, the images of the droplets should be captured. As the time related disturbances may affect the final droplet distribution, the capture process must be online thus a real time camera vision system has been set up. The maximum capture area of the camera is around $12mm \times 8mm$, and the resolution is around $10\mu m/pixel$. The camera is driven and controlled by computer software directly and the captured photos are analyzed by Matlab to extract the required parameters for error compensation. The whole process is online and the camera system can be removed after all the parameters are identified.

Before using the camera vision system, calibration of the camera is compulsory to obtain the corresponding scale in the captured images in unit of $\mu m/pixel$. The calibration ruler with reference circles of known radius is shown in Fig. 5.9 and the capture image of the reference circles are shown in Fig. 5.10. As the colors of the droplet and the plate are white and black respectively during the experiment, the color of the image is
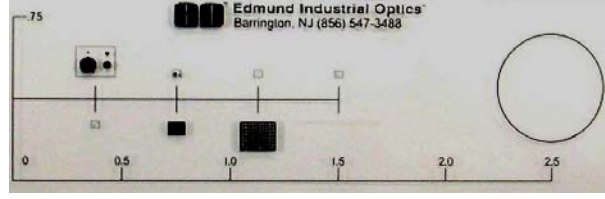
Figure 5.9: Calibration ruler

reverted as the color of the circle is white as shown in Fig. 5.11. The four circles of the reverted circles are analyzed using circle fitting method as shown in Fig. 5.12 and the scale is computed as the average of the ratio between the known radius R_{real} and the measured radius R_{meas} of the four circles.

The flowchart of the camera calibration is shown in Fig. 5.13. First, the figure is converted to a binary image with two colors: white and black, with logic value 1 for white pixel and logic value 0 for black pixel. Second, one pixel P with logic value 1 (which means within a white circle) is recognized using "find" function in Matlab. Third, the outline of the circle which has the pixel P is traced using "bwtraceboundary" function. The location of the pixel P is used as the starting point for the boundary tracing. Fourth, all the pixels (x_i, y_i) along the outline and the circle fitting method are used to obtain the radius and the center coordinate of the circle.

5.6.3 Circle fitting

The circle fitting method is used to obtain the radius r and the center of a circle (x_c, y_c) based on the known coordinates of the circle outline and the circle equation in Eq. 5.2:

$$(x - x_c)^2 + (y - y_c)^2 = r^2 \tag{5.2}$$

Let the coordinate of the circle center $(x_c, y_c) = (a, b)$, and the circle radius $r =$

104
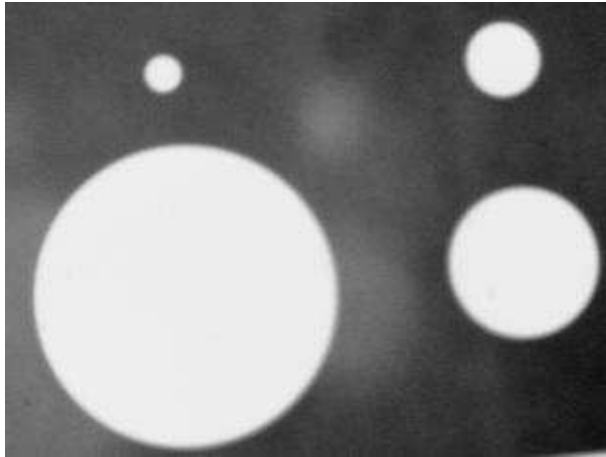
Figure 5.10: Circles captured for calibration
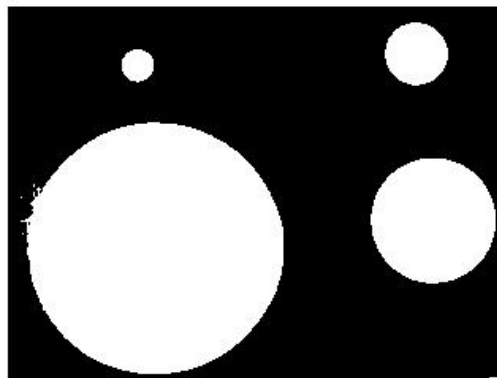
Figure 5.11: Reverted circles for calibration
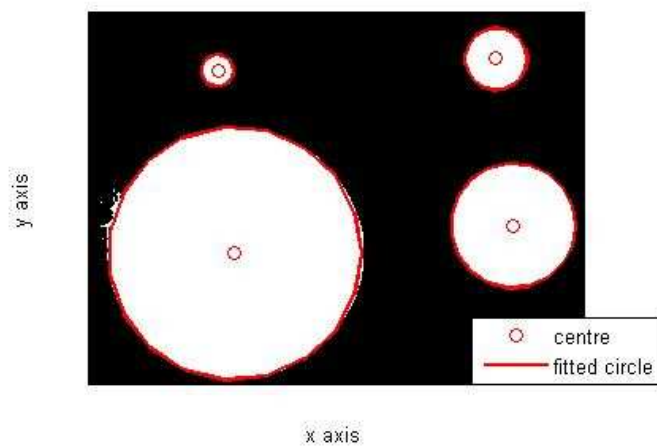
Figure 5.12: Recognized circles after circle fitting
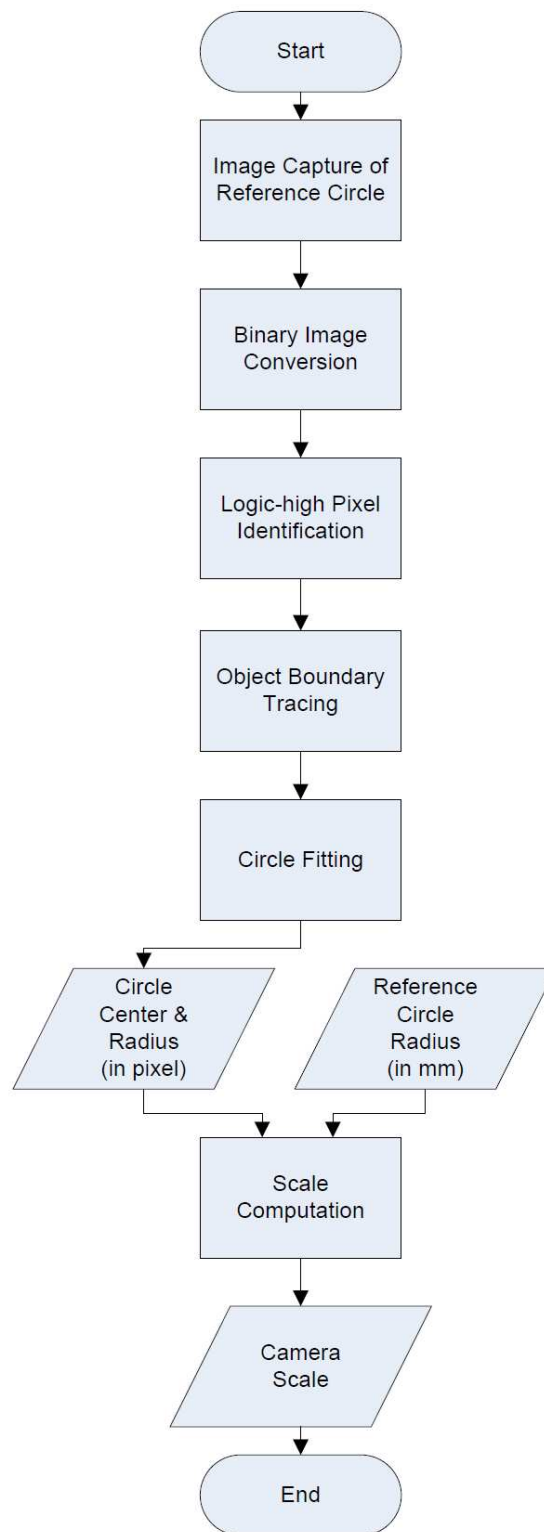
Figure 5.13: Flowchart of camera calibration

$\sqrt{(a^2 + b^2)/4 - c}$, where a, b and c are the unknown variables, then Eq. 5.2 becomes:

$$x^2 + y^2 + ax + by + c = 0 \tag{5.3}$$

As the variables x and y are $N \times 1$ vectors, then the Eq. 5.3 can be transformed as:

$$\begin{bmatrix} X & Y & I \end{bmatrix} \begin{bmatrix} a \\ b \\ c \end{bmatrix} = \begin{bmatrix} -(X^2 + Y^2) \end{bmatrix} \tag{5.4}$$

where I is a $N \times 1$ identity vector

As all the pixels' coordinates (x, y) on the circle outline have been identified, so the

unknown parameter a, b and c can be obtained using Eq. 5.5:

$$\begin{bmatrix} a \\ b \\ c \end{bmatrix} = \frac{\begin{bmatrix} X & Y & I \end{bmatrix}}{\begin{bmatrix} -(X^2 + Y^2) \end{bmatrix}} \tag{5.5}$$

5.6.4 Trajectory model parameter identification

To identify the parameters in Eq. 5.1, a few droplets without compensation at different

heights of the dispensing head are captured using camera vision system in Fig. 5.14. In

Fig. 5.14, droplets A and B are collected at height h_1 and droplets C and D are collected

at h_2. The four droplets are analyzed using circle fitting method and the coordinates

of the fitted circle centers (indicated using green circle) and the target circle centers

(indicated using red square) are measured within the image. The four coordinates can

be substituted in Eq. 5.1 and the parameters α, θ, x_e and y_e can be obtained accordingly.

Then error compensation can be done by updating the target coordinates into the

stage controller using Eq. 5.6:

$$\begin{bmatrix} x_{new} \\ y_{new} \end{bmatrix} = \begin{bmatrix} x_T \\ y_T \end{bmatrix} - \begin{bmatrix} 1 & 0 & tan\theta cos\alpha \\ 0 & 1 & tan\theta sin\alpha \end{bmatrix} \begin{bmatrix} x_e \\ y_e \\ h \end{bmatrix} \tag{5.6}$$
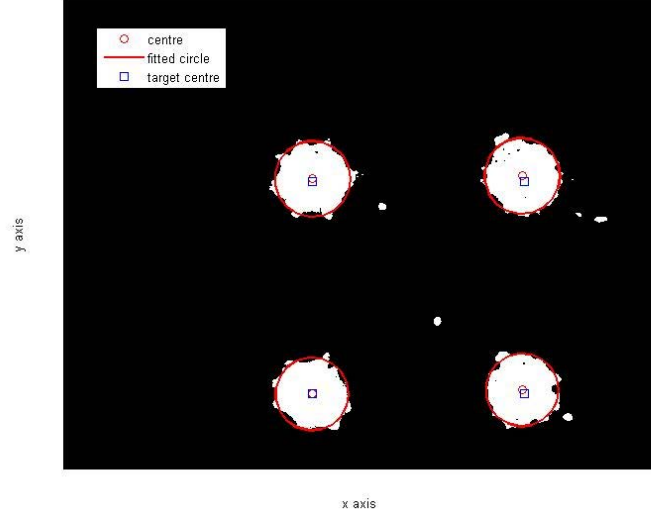
Figure 5.14: Droplets image for trajectory model parameter identification

where x_{new} and y_{new} are the updated coordinates after compensation, x_T and y_T are the target coordinates before compensation, and h is the height of the dispensing head

5.6.5 Compensation results & analysis

After camera calibration and trajectory model parameter identification, the parameters of the camera vision system and the dispensing head can be obtained and the results are shown in Table 5.2. The droplet results of DOD micro-dispensing system before and after droplet error compensation at heights of $2mm$ and $20mm$ are shown in Fig. 5.15 and Fig. 5.16 respectively. Due to the limited resolution of the camera vision system, only eight droplets during the experiment are shown in those two figures. In Fig. 5.15 and Fig. 5.16, the green circles and dotted lines represent the centers and outlines of the fitted circles before compensation, the blue circles and dotted lines represent the centers and outlines of the fitted circles after compensation, and the red squares and triangles represent the target positions for droplets before and after error compensation. The

Table 5.2: Estimated Parameters in Trajectory Model

Parameter type	Value
Image scale	12.9 $\mu m/pixel$
Angle α	0.9739°
Angle θ	89.696°
Placement error x_e	2.0 μm
Placement error y_e	118.2 μm
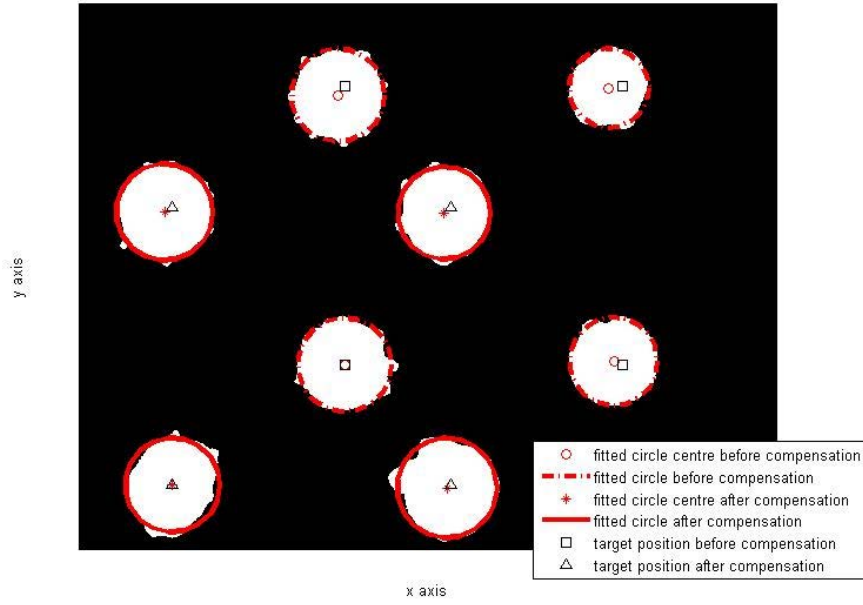
Figure 5.15: Droplet results with and without error compensation at height=2mm

displacement errors of the droplets in Fig. 5.15 and Fig. 5.16 are shown in Table 5.3

and clearly the accuracy of the DOD micro-dispensing system get improved with error

compensation for both height of 2mm and 20mm.

5.7 Conclusion

In this developed micro-valve dispensing DOD system, the micro-valve dispensing head

are attached on the Z axis of a precision stage to perform system characterization

experiments. The deposited droplet positions on the substrate on the XY slide are used
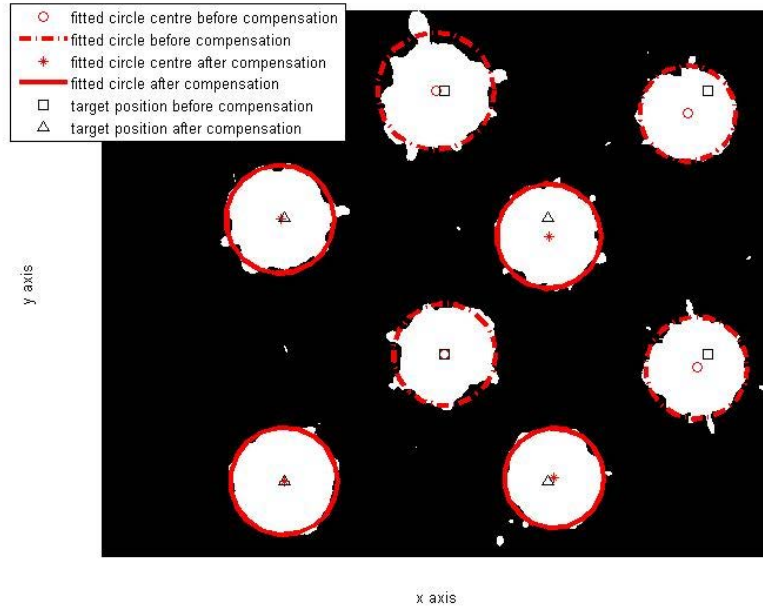
Figure 5.16: Droplet results with and without error compensation at height=20mm

Table 5.3: Displacement Errors Before and After Compensation at Different Heights

	Before (mm)	After (mm)	Improvement
2mm height	0	0	N.A.
	0.1175	0.1036	11.83%
	0.1524	0.0988	35.17%
	0.1056	0.0519	50.85%
20mm height	0	0	N.A.
	0.0995	0.0482	51.56%
	0.3499	0.2142	38.78%
	0.1988	0.0806	59.46%

to test the system accuracy, and the droplet size follows normal distribution. Error compensations are conducted on both precision machine and printed droplets. The accuracy of both the stage and the printed droplets are improved accordingly.

Chapter 6

Conclusions

6.1 Summary of Contributions

The ultimate goal of the research work in this thesis is to investigate and compensate the possible error sources in high precision machine to improve the precision and accuracy, via error compensation technique and sensor selective control approaches. The geometric, thermal and end-effector errors are modeled and the corresponding compensation methods are proposed in this thesis, and a selective control of data fusion of multiple sensors is proposed to deal with the error raised in the sensor measurement.

The geometric error is the most common error in high precision system, but usually the calibration and compensation process may take several days as many optics are involved and each type of optic requires setup time. So first, a cost effective and time efficient method on the geometric error compensation is proposed by computing the error components using displacement measurement results only and estimating the position errors using RBF networks. For validation purposes, all the geometric error components are measured using full sets of optics as the reference and the error components estimated

using RBF network can match the reference values closely. With the proposed geometric error compensation method, the position accuracy of both XY tables are significantly improved.

Together with the geometric error, the thermal error is also one of the main factors behind the system error. Secondly, the system error is identified and modeled using both position and temperature information and a 2D RBF network is used in the error compensation. The position accuracy of the DC linear is improved at both fixed and varying temperatures with the proposed thermal and displacement error compensation method.

Thirdly, a selector control frame work in the data fusion of multiple sensors is proposed to improve the accuracy in the sensor measurement of the precision system. The proposed frame work decreases the computation complexity by using 2D RBF network to estimate the selector attributes in the data fusion of multiple sensors instead of conventional methods like Kalman filter. In the specific case on the control of a DC linear motor using a digital magnetic encoder and an analog velocity sensor, the proposed method can improve the tracking performance and system precision, by comparing the output of the proposed frame work with the reference position signal measured using laser interferometer.

In order to study the error caused by the end-effector, the development and control of the micro-dispensing DOD system is investigated lastly. The proposed parametric model of the printed droplets are identified online using image processing techniques on the

113

droplets and are updated in the machine controller. Error compensation on both stage and printed droplets are conducted to improve the performance of the DOD system.

In this thesis, extensive experiment results have been furnished to illustrate the effectiveness of the proposed models or methods.

6.2 Suggestions for Future Work

Regarding the efforts and approaches used in this thesis for precision improvement in high precision machine, although above contributions have been made in this thesis, there are still improvements which can be achieved. Thus, the suggestions for future works are given below.

The optimal data collection interval versus accuracy requirement

In Chapter 2, the geometric errors are estimated based on the raw linear data collected using laser interferometer. These raw data are collected at a certain distance interval of 5mm on both machines. In the experiment, we observe that the overall outcome of the error compensation can vary with different data collection intervals and the results with different data collection densities are shown in Table 2.3. This information can be used to reduce the calibration time while maintain the accuracy at a required level. Thus in the future work, it is possible to compare the accuracy of each error component under different data intervals to obtain the relationship between the system accuracy and data collection interval. A RBF approximation can be used to estimate this relationship and find the optimal value of data collection interval under certain accuracy requirement for

future error compensation and calibration work.

Augmented error compensation method with other developed error model

In some situations, the error source may be fairly clear and a dynamic model may be developed for the error source. One possible example is the vibration disturbance generated by a machine. In those cases, the proposed method can be augmented using the known dynamic error model.

If the error source in the developed dynamic error model is measurable in real-time experiments, the induced system error can be calibrated with the error source and the new N-dimensional model can be estimated and implemented into the system. This is quite similar as the method used in Chapter 3, with temperature as another parameter in the error computation and estimation. For example, if the vibration disturbance is the known error model and the vibration source can be modeled and measurable in real time experiments, the linear error can be updated easily from $f_{linear}(position, temp)$ to $f_{linear}(position, temp, vibration)$ by calibrating linear error based on the vibration error as another input parameter. Then updated linear error model with three parameters can be used in the system compensation.

If the error source is not measurable in real-time experiments but the error model is known, the relationship between the error source and the current known and measurable parameters must be identified. Then the known error model can be described using a new model with all current known parameters, and the new model can be implemented into the system. In the vibration error example, if the vibration error is not measurable

in real time but the relationship between vibration error and other parameters such as temperature, velocity and position can be found, the vibration error can be described as a new model g: $f_{vibration} = g(temp, velocity, position)$. This new model g can be used as an input parameter with other parameters to calibrate the system and establish a new model $f_{linear}(position, temp, g)$ in the system compensation.

The effect of heating rate in the thermal error

In Chapter 3, a 2D RBF network is used to estimate the geometric errors, based on both temperature and position measurements, as shown in Fig. 3.1. During the experiments, the heating rate (i.e. temperature changing rate) is considered as a constant in the interpolation of RBF networks. But in real situation, the heating rate may vary during the operational process. Thus, the data interpolation in RBF approximations should be adjusted accordingly. For example, for three geometric error measurements at temperatures T1, T2 and T3 as shown in Fig. 6.1, the RBF approximation should follow the black solid line if the machine is heated at a slower heating rate first and a faster heating rate later from T2 to T3, instead of the dashed line which represents constant heating rate. Thus, 3D RBF network can be proposed to estimate the geometric errors, based on three inputs: temperature, heating rate, and position measurements, as shown in Fig. 6.2.

Dual RBF method in selective control approach

In the specific case of the Chapter 4, one 2-dimensional RBF network is used to estimate computation weightages k_1 and k_2, based on both velocity and noise levels,
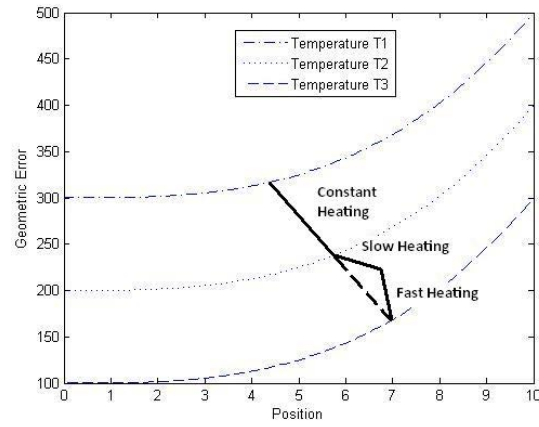
Figure 6.1: Heating rate effect on error compensation
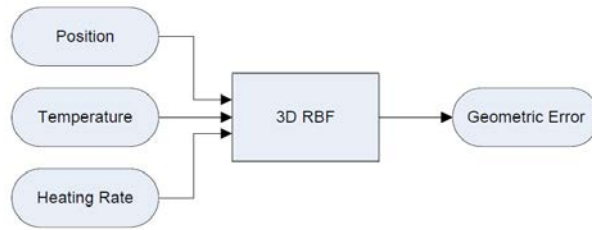
Figure 6.2: Flowchart of 3D RBF network
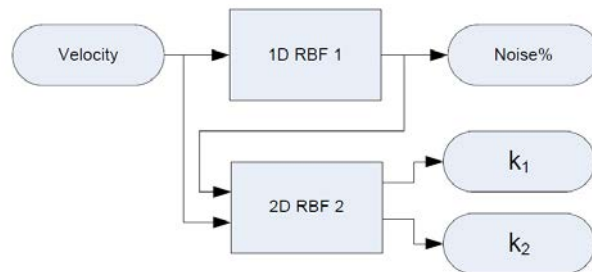
Figure 6.3: Single selector attribute with RBF model of noise versus velocity
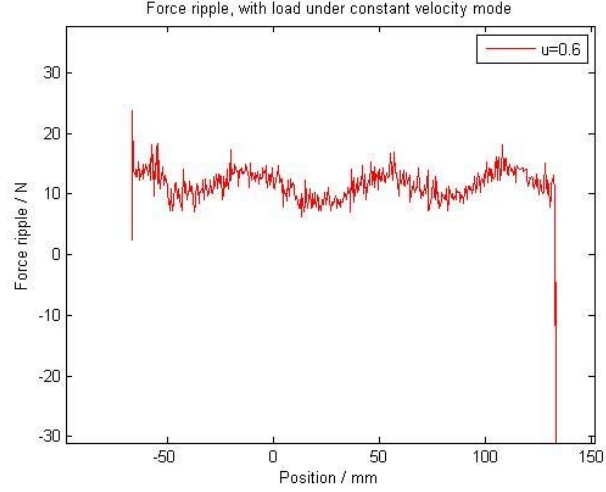
Figure 6.4: Force ripple signal measured

as shown in Fig. 4.7. In this case study, the noise level is obtained directly from the manufacturer's specifications under ideal conditions and introduced into the system as an independent attribute. During real time experiments, we observe that the noise level may vary with a change in velocity so there is also a nonlinear relationship between the velocity measured and the noise level in the sensor. It is possible to use frequency domain signal processing technique by applying filter to estimate the noise level dynamically and directly from the raw data. This method is very commonly adopted but it introduces additional dynamics into the system. It is also possible to train another RBF network offline to model the relationship between the velocity and noise level, to obtain the noise level directly from velocity measurements for a specific velocity sensor. So a dual RBF network method can be proposed to estimate the selector attributes, as shown in Fig. 6.3.

Delay minimization in multi-sensor fusion

In the feedback control, the multi-sensor fusion will lead to some level of delay. The delay may come from both the fusion process of multiple sensors, and the operation of each sensor (e.g., the integral activity in the velocity sensor). A significant delay in the feedback control may cause several problems including control failure, as the data obtained is not live or accurate. In order to minimize the delay, the following possible approaches can be considered to improve the proposed method in Chapter 4:

a) For some situations, some of the sensors contribute very little to the overall fusion output. Thus, in order to avoid the delay in the fusion process of the multiple sensors, the outputs of those sensors can be disabled. With fewer sensors in the data fusion, the computational complexity can be lowered. Thus, an intelligent and efficient sensor switch schedule can be proposed during the operation process.

b) The current data fusion algorithm consists of several computations such as integration of velocity sensor output. The delay can be minimized if a new algorithm of the data fusion is proposed to minimize the computational complexity.

c) The sampling intervals of each sensor at different situations can be changed to minimize the delay in the sensor signal acquisition process, according to the operational performance and system requirement. For example, at low speed operation of the machine, the sampling intervals can be decreased for some sensors while maintaining the accuracy unaffected.

d) It is also possible to upgrade the hardware of the system like control card and sensors with better specifications to minimize the delay from the hardware side.

Extension from linear sensor fusion to nonlinear fusion

Nonlinearity exists in many systems and the linear sensor fusion may not be applicable in these situations. Thus nonlinear sensor fusion method can be considered to deal with the nonlinearity in the system. Two possible ways can be considered to extend the proposed linear sensor fusion method in the thesis:

a) If the linear regions in the system can be identified, or the nonlinear system can be divided into several regions which can be approximated using linear method, the proposed linear sensor fusion method can still be applied to those linear regions (or approximately divided linear regions). The calibration of the system can be done in different regions to identify the specific weightages in those regions.

b) The data fusion output can be described using n-th order polynomial based on the outputs of the individual sensors. Calibration work of the system can be conducted to identify the order n and the coefficients of the polynomial. For example, with the encoder sensor and velocity sensor in Chapter 4, the new position signal can be described as: $x_{new} = k_0 x_{enc}^n + k_1 x_{enc}^{n-1} x_{vel}^1 + ... + k_n x_{vel}^n$, where x_{new} is the sensor fusion output, k_i is the weightage coefficient, x_{enc} is the encoder output and x_{vel} is the velocity sensor output. The linear data fusion method proposed in the thesis can also be considered as a special case of the polynomial method with order $n = 1$.

Precision control with force ripple signal

Force ripple can significantly affect the performance of the precision system, due to the attracting and repelling forces in the magnetic structure. Several techniques have been

applied to identify and compensate the force ripple signal in precision systems [111]-[113]. From experiment observations using linear motor in Fig. 4.4, the force ripple is a repeatable, periodic and position dependent signal, as shown in Fig. 6.4. Besides improving the system precision by compressing or compensating the force ripple signal, it is also possible to identify and model the force ripple signal under different system variables like current, voltage, position and velocity etc. With the proper modeling of force ripple signal, a sensor-less position control in the precision machine may be possible.

Bibliography

[1] S.T. Smith, R.M. Seugling, "Sensor and actuator considerations for precision, small machines", Precision Engineering, vol. 30, no. 3, pp. 245-264, 2006

[2] F. Haugen, Basic Dynamics and Control, ISBN 978-82-91748-13-9, 2009

[3] "Laser and optics user's manual", Agilent Technologies, 2007

[4] H. Nakazawa, Principles of Precision Engineering, Oxford University Press, USA, 1994

[5] O. Reimer, K. Rickens, "Review of Ultra Precision Machining Capabilities", CERN, 2012

[6] F.Z. Fang, V.C. Venkatesh, "Diamond Cutting of Silicon with Nanometric Finish", Annals of the CIRP, vol. 47, no. 1, pp. 45-49, 1998

[7] N. Taniguchi, "Current status in and future trends of ultra precision machining and ultra-fine processing", Annals of the CIRP, vol. 32, no. 2, pp. 573-582, 1983

[8] United Nations, Text of the CBD, http://www.cbd.int/convention/text/, 1992

[9] M.G. Fri, U.P. Kralovnszky, "The founding father of biotechnology: Kroly (Karl) Ereky", International Journal of Horticultural Science, vol. 12, no. 1, pp. 9-12, 2006

[10] A.S. Putra, S. Huang, K.K. Tan, S.K. Panda, T.H. Lee, "Design, modeling, and control of piezoelectric actuators for intracytoplasmic sperm injection", IEEE Transactions on Control Systems Technology, vol. 15, no. 5, pp. 879-890, 2007

[11] J.S. Chen, T.W. Kou, S.H. Chiou, "Geometric error calibration of multi-axis machines using an auto-alignment laser interferometer", Precision Engineering, vol. 23, no. 4, pp. 243C252, 1999

[12] "Engineering Reference", Aerotech

[13] M.A. Donmez, D.S. Blomquist, R.J. Hocken, C.R. Liu, M.M. Barash, "A general methodology for machine tool accuracy enhancement by error compensation", Precision Engineering, vol. 8, no. 4, pp. 187-196, 1986

[14] "What is metrology?", http://www.bipm.org/en/convention/wmd/2004/, BIPM, 2004

[15] K. Takamasu, S. Ozawa, T. Asano, A. Suzuki, R. Furutani, S. Ozono, "Basic concepts of nano-CMM (coordinate measuring machine with nanometer resolution)", In Proceedings of Japan-China Bilateral Symposium on Advanced Manufacturing Engineering, vol. 155, pp. 155-158, 1996

[16] K. Takamasu, K.R. Furutani, S. Ozono, "Development of nano-CMM (coordinate measuring machine with nanometer resolution)", In Proceedings of the XIV IMEKO World Congress, vol. 8, pp. 34-39, 1997

[17] F.G. Shinskey, JP Shunta, J.E. Jamison, A. Rohr, "2.28 Selective, Override, and Limit Controls", 2006

[18] S.T. Smith, R.M. Seugling, "Sensor and actuator considerations for precision, small machines", Precision Engineering, vol. 30, no. 3, pp. 245-264, 2006

[19] W. Wu, X. Wen, Z.L. Wang, "Taxel-addressable matrix of vertical-nanowire piezotronic transistors for active/adaptive tactile imaging", Science, 2013

[20] L. Liu, K.K. Tan, A.S. Putra, T.H. Lee, "Compensation of hysteresis in piezoelectric actuator with iterative learning control", IEEE/ASME International Conference on Advanced Intelligent Mechatronics, pp. 1300-1305, 2009

[21] L. Liu, K.K. Tan, S. Chen, C.S. Teo, T.H. Lee, "Identification and compensation of hysteretic dynamics of piezoelectric actuators for accurate and fast scanning", IEEE Conference on Industrial Electronics and Applications, pp. 1633-1638, 2012

[22] A. Bunte, S. Beineke, "High-performance speed measurement by suppression of systematic resolver and encoder errors", IEEE Transactions on Industrial Electronics, vol. 51, no. 1, pp. 49-53, 2004

[23] K.K. Tan, S.N. Huang, "Geometrical error compensation of machines with significant random errors", ISA Transactions, vol. 44, no. 1, pp. 43-53, 2005

[24] C.S. Teo, K.K. Tan, S.Y. Lim, "Dynamic geometric compensation for gantry stage using iterative learning control", IEEE Transactions on Instrumentation and Measurement, vol. 57, no. 2, pp. 413-419, 2008

[25] K.K. Tan, S.N. Huang, T.H. Lee, "Geometrical error compensation and control of an XY table using neural networks", Control Engineering Practice, vol. 14, no. 1, pp. 59-69, 2006

[26] T.H. Lee, K.K. Tan, S.N. Huang, "Adaptive friction compensation with a dynamical friction model", IEEE/ASME Trans.Mechatronics, vol. 16, issue 1, pp. 133-140, 2011

[27] ASME B5.54-1992, Methods for performance evaluation of computer numerically controlled machining centers, The American Society of Mechanical Engineers, New York, 1993

[28] S. Sartori, G.X. Zhang, "Geometric error measurement and compensation of machine", Annals of CIRP, vol. 44, no. 2, pp617-634, 1995

[29] P.S. Huang, J. Ni, "On-line error compensation of coordinate measuring machines", International Journal of Machine Tools and Manufacture, vol. 35, no. 5, pp. 725-738, 1995

[30] P. Yang, T. Takamura, S. Takahashi, K. Takamasu,O. Sato, S. Osawa, T. Takatsuji, "Development of high-precision micro-coordinate measuring machine: multi-probe measurement system for measuring yaw and straightness motion error of XY linear stage", Precision Engineering, vol. 35, issue. 3, pp. 424-430, 2011

[31] P. Majda, "Modeling of geometric errors of linear guideway and their influence on joint kinematic error in machine tools",Precision Engineering, vol. 36, issue. 3, pp. 369-378, 2012

[32] Y. Kakino, Y. Ihara, Accuracy Inspection of NC Machine Tools by Double Ball Bar Method, New York: Gardner Publications, pp. 61-69, 1993

[33] N. Srinivasa, J.C. Ziegert, C.D. Mize,"Spindle thermal drift measurement using the laser ball bar", Precision Engineering, vol. 18, no. 2-3, pp. 118-128, 1996

[34] G.W. Caskey, S.D. Philips, B.R. Borchardt, "Results of the NIST national ball plate round robin", Journal of Research of the National Institute of Standards and Technology, vol. 102, no. 1, pp. 85-93, 1997

[35] B. Bringmann, W. Knapp, "Machine tool calibration: geometric test uncertainty depends on machine tool performance", Precision Engineering, vol. 33, no. 4, pp. 524-529, 2009

[36] Z. He, J. Fu, X. Yao, W. Qian, "Volumetric error identification for CNC machine tool based on multi-body system and vector diagonal measurement", in Int. Conf. Mechanic Automation and Control Engineering (MACE), pp. 3345-3349, 2010

[37] A. Balsamo, P. Pedone, E. Ricci, M. Verdi, "Low-cost interferometric compensation of geometrical errors", Annals of the CIRP, vol. 58, no. 1, pp. 459-462, 2009

[38] S.C. Jeng, W.K. Tzu, H.C. Shen, "Geometric error calibration of multi-axis machines using an auto-alignment laser interferometer", Precision Engineering, vol. 23, no. 4, pp. 243-252, 1999

[39] G. Zhang, R. Ouyang, B. Lu, "A displacement method for machine geometry calibration", Annals of the CIRP, vol. 7, pp. 515-518, 1988

[40] G. Zhang, R. Veale, T. Charlton, B. Borchardt, R. Hocken, "Error compensation of coordinate measuring machines", Annals of the CIRP, vol. 34, no. 1, pp. 445-448, 1985

[41] G. Zhang, R. Hocken, "Improving the accuracy of angle measurement in machine calibration", Annals of the CIRP, vol. 35, no. 1, pp. 369-372, 1986

[42] G. Chen, J. Yuan, J. Ni, "A displacement measurement approach for machine geometric error assessment", International Journal of Machine Tools & Manufacture, vol. 41, pp. 149-161, 2001

[43] K. Umetsu, R. Furutani, S. Osawa, T. Takatsuji and T. Kurosawa, "Geometric calibration of a coordinate measuring machine using a laser tracking system", Measurement Science and Technology, vol. 16, no. 12, pp. 2466-2472, 2005

[44] Y.M. Ertekin, A.C. Okafor, "Vertical machining center accuracy characterization using laser interferometer", Journal of Materials Processing Technology, vol. 105, no. 3, pp. 394-406, 2000

[45] Y. Lin, Y. Shen, "Modelling of five-axis machine tool metrology models using the matrix summation approach", The International Journal of Advanced Manufacturing Technology, vol. 21, no. 4, pp. 243-248, 2003

[46] D.E. Gilsinn, A.V. Ling, "Comparative statistical analysis of test parts manufactured in production environments", Journal of Manufacturing Science and Engineering, vol. 126, no. 1, pp. 189-199, 2004

[47] A.W. Khan, W. Chen, "Systematic geometric error modeling for workspace volumetric calibration of a 5-axis turbine blade grinding machine original research article", Chinese Journal of Aeronautics, vol. 23, no. 5, pp. 604-615, 2010

[48] K.K. Tan, T.H. Lee, S.N. Huang, Precision Motion Control Design and Implementation, 2nd edition, Advances in Industrial Control Series, London: Springer-Verlag, 2008

[49] K.K. Tan, S.N. Huang, H.L. Seet, "Geometrical error compensation of precision motion systems using radial basis function", IEEE Transactions on Instrumentation and Measurement, vol. 49, issue. 5, pp. 984-991, 2000

[50] S. Olyaeea, S. Hamedib, Z. Dashtbana, "Efficient performance of neural networks for nonlinearity error modeling of three-longitudinal-mode interferometer in nano-metrology system", Precision Engineering, vol. 36, issue. 3, pp. 379-387, 2012

[51] C.M. Bishop, Neural Networks for Pattern Recognition, Oxford University Press, 1995

[52] J. Lopez, M. Artes, "A new methodology for vibration error compensation of optical encoders", Sensors, vol. 12, no. 4, pp. 4918-4933, 2012

[53] R. Hocken, J. A. Simpson, B. Borchardt, J. Lazar, C. Reeve, P. Stein, "Three dimensional metrology", Annals of the CIRP, vol. 26, no. 2, pp. 403C408, 1977

[54] P.M. Ferreira, C.R. Liu, E.Merchant, "A contribution to the analysis and compensation of the geometric error of a machining center", Annals of the CIRP, vol. 35, pp. 259C262, 1986

[55] D.E. Rumelhart, G.E. Hintont, R.J. Williams, "Learning representations by back-propagating errors", Nature, vol. 323, no. 6088, pp. 533-536, 1986

[56] S. Haykin, Neural Networks: A Comprehensive Foundation, Prentice Hall PTR, 1994

[57] J.A. Leonard, M.A. Kramer, "Radial basis function networks for classifying process faults", Control Systems, IEEE, vol. 11, no. 3, pp. 31-38, 1991

[58] R.J. Howlett, L.C. Jain, (eds.), Radial Basis Function Networks 2: New Advances in Design, vol. 67, Springer, 2001

[59] E.J. Hartman, J.D. Keeler, J.M. Kowalski, "Layered neural networks with Gaussian hidden units as universal approximations", Neural computation, vol. 2, no. 2, pp. 210-215, 1990

[60] R. Ramesh, M.A. Mannan, A.N. Poo, "Error compensation in machine tools a review: Part I: geometric, cutting-force induced and fixture-dependent errors", International Journal of Machine Tools and Manufacture, vol. 40, issue 9, pp. 1235-1256, 2000

[61] J. Mayr, J. Jedrzejewski, E. Uhlmann, M.A. Donmez, W. Knapp, F. Hartig, K. Wendt, T. Moriwaki, P. Shore, R. Schmitt, C. Brecher, T. Wrz, K. Wegener, "Thermal issues in machine tools", CIRP Annals - Manufacturing Technology, vol. 61, issue 2, pp. 771-791, 2012

[62] R. Ramesh, M.A. Mannan, A.N. Poo, "Error compensation in machine tools a review: Part II: thermal errors", International Journal of Machine Tools and Manufacture, vol. 40, issue 9, pp. 1257-1284, 2000

[63] Y. Wang, G. Zhang, S. M. Kee, J. W. Sutherland, "Compensation for the thermal error of a multi-axis machining center", Journal of Materials Processing Technology, vol. 75, issue 1, pp. 45-53, 1998.

[64] S. Li, Y. Zhang, G. Zhang, "A study of pre-compensation for thermal errors of NC machine tools", International Journal of Machine Tool & Manufacture, vol. 37, issue 12, pp. 1715-1719, 1997

[65] S. Yang, J. Yan, J. Ni, "Accuracy enhancement of a horizontal machining center by real-time compensation", Journal of Manufacturing Systems, vol. 15, issue 2, pp. 113-124, 1996

[66] J. Yang, J. Yuan, J. Ni, "Thermal error mode analysis and robust modeling for error compensation on a CNC turning center", International Journal of Machine Tools and Manufacture, vol. 39, issue 9, pp. 1367-1381, 1999

[67] J. Mou, M.A. Donmez, C. Cetinkunt, "An adaptive error correction method using feature-based analysis techniques for machine performance improvement. Part 1: Theory derivation", ASME Trans. Journal of Engineering for Industry, vol. 117, pp. 584-590, 1995

[68] D.A. Krulewich, "Temperature integration model and measurement point selection for thermally induced machine tool errors", Mechtronics, vol. 8, pp. 395-412, 1998

[69] A. Balsamo, D. Marques, S. Sartori, "A method for thermal deformation corrections of CMMs", Annals of the CIRP, vol. 39, issue 1, pp. 557-560, 1990

[70] S. Eastwood, P. Webb, "Compensation of thermal deformation of a hybrid parallel kinematic machine", Robotics and Computer-Integrated Manufacturing, vol. 25, issue 1, pp. 81-90, 2009

[71] J.S. Chen, "Fast calibration and modeling of thermally induced machine tool errors in real machining", International Journal of Machine Tools and Manufacture, vol. 37, issue 2, pp. 159-169, 1997

[72] M. Yang, J. Lee, "Measurement and prediction of thermal errors of a CNC machining centre using two spherical balls", ASME Trans. Journal of Materials Processing Technology, vol. 75, pp. 180-189, 1998

[73] J. Mou, "A method of using neural networks and inverse kinematics for machine tools error estimation and correction", Journal of Manufacturing Science and Engineering, vol. 119, issue 2, pp. 247-254, 1997

[74] Y. Zhang, S.N. Huang, K.K. Tan, "Vision-assisted thermal monitoring system for CNC machine surveillance", Proceedings of the IEEE International Conference on Automation and Logistics, pp. 382-387, 2008

[75] H.V. Hoang, J.W. Jeon, "An efficient approach to correct the signals and generate high-resolution quadrature pulses for magnetic encoders", IEEE Transactions on Industrial Electronics, vol. 58, no. 8, pp. 3634-3646, Aug 2011

[76] K.K. Tan, H.X. Zhou, "New interpolation method for quadrature encoder signals", IEEE Transactions on Instrumentation and Measurement, vol. 51, no. 5, pp. 1073-1079, Oct 2002

[77] K.K. Tan, K.Z. Tang, "Adaptive online correction and interpolation of quadrature encoder signals using radial basis functions", IEEE Trans. IEEE Transactions on Control Systems Technology, vol. 13, no. 3, pp. 370-377, May 2005

[78] M. Kayal, F. Burger, R.S. Popovic, "Magnetic angular encoder using an offset compensation technique" IEEE Sensors Journal, vol. 4, no. 6, pp. 759-763, Dec 2004

[79] S.H. Hwang, J.H. Lee, J.M. Kim, C. Choi, "Compensation of analog rotor position errors due to nonideal sinusoidal encoder output signals", IEEE Energy Conversion Congress and Exposition (ECCE), pp. 4469-4473, 2010

[80] J.N. Gross, Y. Gu, M.B. Rhudy, S. Gururajan, M.R. Napolitano, "Flight test evaluation of sensor fusion algorithms for altitude estimation", IEEE Transactions on Aerospace and Electronic Systems, vol. 48, no. 3, pp. 2128-2139, 2012

[81] G.A. Einicke, Smoothing, Filtering and Prediction: Estimating the Past, Present and Future, Rijeka, Croatia: Intech, 2012

[82] D. Amarasinghe, G.KI. Mann, R.G. Gosine, "Landmark detection and localization for mobile robot applications: a multisensor approach", Robotica, vol. 28, no. 5, pp. 663-673, 2010

[83] P. Goel, S.I. Roumeliotis, G.S. Sukhatme, "Robust localization using relative and absolute position estimates", Proceedings of IEEE/RSJ International Conference on Intelligent Robots and Systems (IROS), vol. 2, pp. 1134-1140, 1999

[84] V.H. Chan, C. Bradley, G.W. Vickers, "A multi-sensor approach to automating coordinate measuring machine-based reverse engineering", Computers in Industry, vol. 44, no. 2, pp. 105-115, 2001

[85] V. Carbone, M. Carocci, E. Savio, G. Sansoni, L. De Chiffre, "Combination of a vision system and a coordinate measuring machine for the reverse engineering of freeform surfaces", The International Journal of Advanced Manufacturing Technology, vol. 17, no. 4, pp. 263-271, 2001

[86] Y. Huang, L. Haiyan, Q. Wang, L. Chen, "Integrating multiple sensors for the closed-loop three-dimensional digitization", Proceedings of the Institution of Mechanical Engineers, Part C: Journal of Mechanical Engineering Science, 2012

[87] T.S. Shen, J. Huang, C.H. Menq, "Multiple-sensor integration for rapid and high-precision coordinate metrology", IEEE/ASME Transactions on Mechatronics, vol. 5, no. 2, pp. 110-121, 2000

[88] E.I. Gokce, A.K. Shrivastava, J.J. Cho, Y. Ding, "Decision fusion from heterogeneous sensors in surveillance sensor systems", IEEE Transactions on Automation Science and Engineering, vol. 8, no. 1, pp. 228-233, 2011

[89] D.E. Kline, C. Surak, P.A. Araman, "Automated hardwood lumber grading utilizing a multiple sensor machine vision technology", Computers and Electronics in Agriculture, vol. 41, no. 1 pp. 139-155, 2003

[90] J. Tang, T. Chai, W. Yu, L. Zhao, "Modeling load parameters of ball mill in grinding process based on selective ensemble multisensor information", IEEE Transactions on Automation Science and Engineering, vol. PP, no. 99, pp. 1-15, 2012

[91] L. Cui, M.J. Swann, A. Glidle, J.R. Barker, J.M. Cooper, "Odour mapping using microresistor and piezo-electric sensor pairs", Sensors and Actuators B: Chemical, vol. 66, no. 1, pp. 94-97, 2000

[92] Q. Yang, Y. Chen, "Reliability of coordinate sensor systems under the risk of sensor precision degradations", IEEE Transactions on Automation Science and Engineering, vol. 7, no. 2, pp. 291-302, 2010

[93] A.B. Forbes, "Weighting observations from multi-sensor coordinate measuring systems", Measurement Science and Technology, vol. 23, no. 2, 025004, 2012

[94] A. Weckenmann, X. Jiang, K-D. Sommer, U. Neuschaefer-Rube, J. Seewig, L. Shaw, T. Estler, "Multisensor data fusion in dimensional metrology", CIRP Annals-Manufacturing Technology, vol. 58, no. 2, pp. 701-721, 2009

[95] A. Sebastian, A. Pantazi, "Nanopositioning with multiple sensors: a case study in data storage", IEEE Transactions on Control Systems Technology, vol. 20, no. 2, pp. 382-394, 2012

[96] I.A. Mahmood, S. Moheimani, K. Liu, "Tracking control of a nanopositioner using complementary sensors", IEEE Transactions on Nanotechnology, vol. 8, no. 1, pp. 55-65, 2009

[97] L. Li, M. Saedan, W. Feng, J.Y.H Fuh, Y.S. Wong, H.T. Loh, S.C.H. Thian, S.T. Thoroddsen, L. Lu, "Development of a multi-nozzle drop-on-demand System for multi-material dispensing", Journal of Materials Processing Technology, vol. 209, no. 9, pp. 4444C4448, 2009

[98] J. Sun, J.H. Ng, J.Y.H. Fuh, Y.S. Wong, H.T. Loh, Q. Xu, "Comparison of micro-dispensing performance between micro-valve and piezoelectric printhead", Microsystem Technologies, vol. 15, no. 9, pp. 1437C1448, 2009

[99] M.H. Tsai, W.S. Hwang WS, H.H. Chou, P.H. Hsieh, "Effects of pulse voltage on inkjet printing of a silver nanopowder suspension", Nanotechnology, vol. 19, no. 33, pp. 335304C335312, 2008

[100] S. Khalil, J. Nam, W. Sun, "Multi-nozzle deposition for construction of 3D biopolymer tissue scaffolds", Rapid Prototyping Journal, vol. 11, no. 1, pp. 9C17, 2005

[101] E.W. Lee, G.C. Phil, "Method and apparatus for preparing biomimetic scaffold", US Patent WO/2003/079985

[102] W.O. Kwang, C.H. Ahn, "A review of microvalves", Journal of Micromechanics and Microengineering, vol. 16, no. 5, pp. 13C39, 2006

[103] R. Li, A. Nasser, C. Sanjeev, "Droplet generation from pulsed micro-jets", Exp Thermal Fluid Sci, vol. 32, no. 8, pp. 1679C1686, 2008

[104] M. Zhang, T.J. Tarn, N. Xi, "A nano-liter bio-material spotting system for bio-chip microarray fabrication", Proceedings of ICRA, vol. 2, pp. 1456-1461, 2004

[105] T. Shutter, "An overview of digital printing for advanced interconnect applications", Circuit World, vol. 31, no. 3, pp. 4-9, 2005

[106] S.K. Moore, "Making chips to probe genes", IEEE Spectrum, pp. 54-60, March 2001

[107] "Drive waveform effects on ink-jet device performance", MicroFab Technote 99-03, 1999

[108] M. Ibrahim, T. Otsubo, H. Narahara, H. Koresawa, H. Suzuki, "Inkjet printing resolution study for multi-material rapid prototyping", JSME International Journal Series C, vol. 49, no. 2, pp. 353-360, 2006

[109] A.A. Khalate, X. Bombois, R. Babuska, H. Wijshoff, R. Waarsing, "Performance improvement of a drop-on-demand inkjet printhead using an optimization-based feed-forward control method", Control Engineering Practice, vol. 19, no. 8, pp. 771-781, 2011

[110] H. Wijshoff, "The dynamics of the piezo inkjet printhead operation", Physics Reports, vol. 491, no. 4, pp. 77-177, 2010

[111] K.K. Tan, S.N. Huang, T.H. Lee, "Robust adaptive numerical compensation for friction and force ripple in permanent-magnet linear motors", IEEE Transactions on Magnetics, vol. 38, no. 1, pp. 221-228, 2002

[112] S. Zhao, K.K. Tan, "Adaptive feedforward compensation of force ripples in linear motors", Control Engineering Practice, vol. 13, no. 9, pp. 1081-1092, 2005

[113] K.K. Tan, S.J. Chin, H.F. Dou, "Feedforward suppression of force ripple based on a simplex-optimized dither signal", ISA transactions, vol. 42, no. 1, pp. 19-27, 2003

Author's Publications

Journal Papers

1. J. Sun, R. Yang, K. K. Tan, J. Y. H. Fuh and Y. S. Wong. Performance Characterization of Drop-On-Demand Micro-Dispensing System with Multi-Printheads. *Microsystem Technologies*, 16(12):2087-2097, 2010

2. J. Sun, J. Y. H. Fuh, E. S. Thian, G. S. Hong, Y. S. Wong, R. Yang and K. K. Tan. Fabrication of Electronic Devices with Multi-material Drop-on-demand Dispensing System. *International Journal of Computer Integrated Manufacturing*, accepted 2011

3. K. K. Tan, S. Huang, C. S. Teo and R. Yang. Controller Design of Eddy Current Braking in An Air Bearing System. *Automatica*, 48(11):2831-2836, 2012

4. R. Yang, K. K. Tan, A. Tay, S. Huang, J. Sun, J. Y. H. Fuh, Y. S. Wong and C. S. Teo. RBF-Based Geometric Error Compensation with Displacement Measurements Only. *IEEE Transactions on Automation Science and Engineering*, submitted

5. R. Yang, A. Tay, K. K. Tan. Displacement and Thermal Error Compensation

using RBF Networks. *IEEE Transactions on Industrial Informatics*, submitted

6. R. Yang, P. V. Er, K. K. Tan. Selective Control Approach Towards Precision Motion Systems. *IEEE Transactions on Automation Science and Engineering*, submitted

Conference Papers

1. J. Sun, J. Y. H. Fuh, Y. S. Wong, E. S. Thian, R. Yang and K. K. Tan. Fabrication of Electronics Devices with Multi-Material Drop-On-Demand Dispensing System. In *Proceedings of the 2010 International Conference on Manufacturing Automation, ICMA 2010*, pages 64-70, Hong Kong, 2010

2. K. K. Tan, S. N. Huang, C. S. Teo and R. Yang. Damping Estimation and Control of A Contactless Brake System Using An Eddy Current. In *Proceedings of the 8th IEEE International Conference on Control & Automation, ICCA 2010*, pages 2224-2228, Xiamen, China, 2010

3. K. K. Tan, P. V. Er, R. Yang, C. S. Teo. Selective Precision Motion Control using Weighted Sensor Fusion Approach. In *Proceedings of the 2013 IEEE International Conference on Mechatronics & Automation, ICMA 2013*, pages 179-184, Takamatsu, Japan, 2013

4. K. K. Tan, R. Yang, P. V. Er, A. Tay, C. S. Teo. RBF-based Compensation Method on Displacement and Thermal Error. In *Proceedings of the 2013 IEEE*

International Conference on Mechatronics & Automation, ICMA 2013, pages 1039-1044, Takamatsu, Japan, 2013

Design Competition:

1. R. Yang, S. Chen, and K.K. Tan. Motor Dynamics Simulation Systems. 3rd Prize, *Agilent VEE Challenge 2008*, Penang, Malaysia, 2008.